UNIVERSITY OF TECHNOLOGY SYDNEY

Faculty of Engineering & Information Technology

EXPERIMENTAL AND NUMERICAL STUDY OF A FIXED MULTI–CHAMBER OSCILLATING WATER COLUMN DEVICE (MC–OWC)

A thesis submitted for degree of

Doctor of Philosophy

MOHAMMAD MOUSA ODEH SHALBY

Faculty of Engineering & Information Technology
School of Mechanical and Mechatronics Engineering

EXPERIMENTAL AND NUMERICAL STUDY OF A FIXED MULTI–CHAMBER OSCILLATING WATER COLUMN DEVICE (MC–OWC)

Done by:	MOHAMMAD MOUSA ODEH SHALBY
Supervisor:	Dr. Paul Walker
Co–supervisor:	Dr. Phuoc Huynh
External supervisor:	Prof. David Dorrell
External supervisor:	Dr. Ahmed Elhanafi

Course code: C02018

Subject Number: 49986 Doctor of Philosophy (PhD)

Dates: 24/02/2015 to 18/02/2018

University of Technology Sydney (UTS)

P.O. Box 123, Broadway, Ultimo, N.S.W. 2007

Australia

Certificate

I certify that the work in this thesis has not previously been submitted for a degree nor has it been submitted as part of requirements for a degree except as part of the collaborative doctoral degree and/or fully acknowledged within the text.

I also certify that the thesis has been written by me. Any help that I have received in my research work and the preparation of the thesis itself has been acknowledged. In addition, I certify that all information sources and literature used are indicated in the thesis. This research is supported by the Australian Government Research Training Program.

Signature of Student:

Production Note:
Signature removed prior to publication.

Date: *18 February 2019*

Acknowledgements

First and foremost, my sincere thanks go to Allah, who endowed me to complete this doctorate and for creating the grand power of ocean waves I have had the honour of studying in such depth. In particular, I am grateful to AL–Hussein bin Talal University, Ma'an, Jordan for their financial support of this project.

Most of all, I wish to thank my supervisory team, Dr.Paul Walker, Dr Phuoc Huynh and Professor David Dorrell for giving me the opportunity to perform this work and having guided and helped me throughout the project. Their assistance and advice have made this a rewarding experience. I would also like to extend my sincere gratitude to Dr. Ahmed Elhanafi for his dedicated help, expertise, advice, inspiration, encouragement and continuous support, throughout my studies.

I express my thanks to Manly Hydraulic Laboratories for allowing me to use their laboratory facilities for my experimental work and I would like to acknowledge Mr. Indra Jayewardene and other staff in Manly Hydraulic Laboratories for their assistance during my research. I offer my thanks to Mr.Christopher Hamid, Mr. Michael Diponio andEng.Vahik Avakian from the School of Mechanical and Mechatronic Engineering for their cooperation, encouragement and for facilitating the requirements for this research work.

I am extremely grateful to my mother, father, brothers and sisters for all of the sacrifices that you've made on my behalf. Your prayers for me have sustained me thus far. I will never be able to pay back the love and affection showered upon me by my family. I especially wish to thank my wife, Hafsa, who has been extremely supportive of me throughout this entire process and has made countless sacrifices to help me get to this point.

Finally, I would like to give my special thanks to my great friends. Their motivation and continuous support have helped make this project happen and a more than enjoyable experience. I am really very grateful for all you have done for me.

Abstract

This thesis focuses on preliminary investigating the hydrodynamic performance of a fixed Multi–Chamber OWC (MC–OWC) wave energy converter, which consists of a linear array of four OWC chambers aligned in the same direction of the incident wave propagation. These investigations address the gaps found in previous works by putting forward detailed explanations of the effect of wave height, wave period, device draught and power take–off (PTO) damping on MC–OWC device performance using a combined numerical and experimental approach.

The research methodology was based on two series of experimental sessions and two numerical models. The first experimental campaign was conducted in a small wave flume in the University of Technology Sydney (UTS) for a MC–OWC device at a model–scale of 1:25. This experiment was performed mainly to validate the numerical models and initially observe device response when subjected to limited regular wave conditions. The second experimental session was carried out in the wave flume at the Manly Hydraulic Laboratory (MHL) in New South Wales, Australia for a MC–OWC devices at a model–scale of 1:16. This experiment was designed to 1) assess the device performance over a wide range of regular and irregular wave conditions, 2) study the impact of wave height, wave period and device draught on the performance of a MC–OWC device, and 3) investigate the effect of the pneumatic damping induced by the power take–off (PTO) system on device performance.

The first validated numerical model was a MATLAB time–domain model that was based on a coupling between the rigid piston model and the thermodynamic forces on a MC–OWC device to get a preliminary understanding of device performance. The second numerical model was a fully nonlinear 3D Computational Fluid Dynamics

(CFD) model that was constructed using the commercial code STAR–CCM+. After being validated in good agreement against the physical scale model tests, the CFD model was utilised to study the influence of the power take–off (PTO) damping on the water surface elevation inside the chamber, the differential air pressure, the airflow rate and the device capture width ratio under different incident regular wave conditions.

The extensive analysis of 198 physical tests and 84 CFD simulations revealed that the water surface elevation, differential air pressure, and airflow rate had a similar response in all chambers to the wave conditions, device draught and PTO damping. However, the first chamber always played the primary role in wave energy extraction, and the performance gradually decreased down to the fourth chamber where the lowest performance was found. The maximum capture width ratio of the whole MC–OWC device was found to be 2.1 under regular wave conditions and 0.95 under irregular wave conditions. These ratios were the highest among all similar concepts that have been reported in previous research.

Table of Contents

List of Figures

List of Tables

Acronyms and Abbreviations

Notations

A_1	Chamber area	(m^2)
A_2	Orifice opining area	(m^2)
a	Wave amplitude	(m)
B	Hydrodynamic damping coefficient	(Ns m^{-1})
C_d	Coefficient of discharge	(–)
C_g	Group velocity	(m s^{-1})
c	Wave velocity	(m s^{-1})
c_s	Speed of sound	(m s^{-1})
D	Orifice diameter	(m)
D_pipe	Internal diameter of the pipe	(m)
d	Draught of the water column	(m)
d'	The added draught due to added mass	(m)
E	Total energy	(J)
E_k	Kinetic energy	(J)
E_p	Potential energy	(J)
F	Force	(N)
F_a	Added mass force	(N)
$F_{\Delta p}$	Force due to the varying air pressure	(N)
F_{FK}	Froude–Krylov force	(N)
F_d	Damping force	(N)
F_ex	Exciting force (heave mode)	(N)
f	Frequency	(Hz)
f_e	Peak frequency	(Hz)
fn	Natural frequency	(Hz)
Δf	Frequency bands width	(Hz)
Gi	The wave sensors	(–)
G_{in}	The incident wave height sensor (in the front of the device)	(–)
G_{out}	The wave height sensor in the device rear	(–)
g	Acceleration due to gravity	(m s^{-2})
H	Wave height	(m)
H_s	Significant wave height	(m)
h	Water depth	(m)
h_{in}	The height of the top cover of the chamber relative to the water surface level inside the chamber	(m)

h_{a0}	The height of the top cover of the chamber relative to the SWL	(m)
K	Hydrostatic restoring coefficient	(N m^{-1})
k	Wavenumber	(m^{-1})
k_c	The coverage factor	(–)
L	Wave length	(m)
L_C	Chamber length	(m)
l	Length scale	(–)
M	Mass of the column of water	(kg)
$\mathrm{M_a}$	Added mass (heave mode)	(kg)
m	Air mass	(kg)
$\dot{m}$	Mass flow rate	(kg s^{-1})
N	Number of calibration sample	(–)
n	Number of repeated observations	(–)
P_n	Pneumatic power	(W)
$\overline{P}_n$	Time–averaged pneumatic power	(W)
P_{in}	Mean incident power per meter of the wave crest	(W m^{-1})
P_w	Input power in the OWC	(W)
P_t	The power due to pressure	(W)
P_a	The power is due to airflow velocity	(W)
p_c	Pressure inside a chamber	(Pa)
p_{atm}	Atmospheric air pressure at standard temperature and pressure	(Pa)
Δp	Differential air pressure ($p - p_{\mathrm{atm}}$)	(Pa)
p_{wave}	Dynamic pressure field	(Pa)
Q_w	Airflow rate	(m^3 s^{-1})
Q_p	Volumetric airflow	(m^3 s^{-1})
$\dot{\mathrm{R}}$	The ideal gas constant which is equal to 287.1 for dry air	(J kg^{-1} K^{-1})
Ri	Opening ratio	(–)
R	Correlation coefficient	(–)
$\dot{\mathrm{R}}$	Ideal gas constant	(J kg^{-1} K^{-1})
$S(\omega)$	Spectral variance density	(–)
S	Standard deviation	(–)
s	Wave steepness	(–)
t	Time	(s)
Δt	Time step	(s)

T	Wave period	(s)
T_R	Resonant period	(s)
T_p	Peak period	(s)
T_k	The ambient temperature is in Kelvin	(K)
T_c	The chamber temperature is in Kelvin	(K)
U_S	Standard uncertainty	(–)
$U_{S\text{-}A}$	Standard uncertainty Type A	(–)
$U_{S\text{-}A}$	Standard uncertainty Type B	(–)
V	Air volume	(m^3)
V_i	Air flow velocity	(m. s^{-1})
Y_i	The calibrated data	(–)
$\grave{Y}_i$	The fitted value	(–)
z	The vertical co–ordinate	(m)
u	Fluid velocity in the x–direction	(m s^{-1})
v	Fluid velocity in the y–direction	(m s^{-1})
w	Fluid velocity in the z–direction	(m s^{-1})
η	Water surface elevation	(m)
ε	Capture width ratio	(–)
ε_c	Chamber capture width ratio	(–)
ϕ	Velocity potential	(m^2 s^{-1})
τ	Damping coefficient	(kg$^{1/2}$ m$^{-7/2}$)
γ	The heat capacity ratio	(–)
δ	Calibration factor	(–)
ρ_w	Water density (= 998.2 at 293 K)	(kg m^{-3})
ρ_{air}	Air density (=1.2 for dry air at 293 K)	(kg m^{-3})
θ	Angular length of the chamber	(rad)
ω	Angular frequency	(s^{-1})
ω_n	Natural frequency	(rad s^{-1})
Γ	Viscous stress tensor	(–)
α	Constant that relates to the wind speed and fetches length	(–)
β	Pipe diameter ratio	(–)
Υ	Peak enhancement	(–)
σ	Spectral shape factor	(–)
σ_{est}	The standard error of the estimate	(–)
μ	Dynamic viscosity	(m^2 s^{-1})
λ	Scale ratio	(–)

Abbreviations Used in Thesis

BEM	Boundary element method
CFD	Computational Fluid Dynamics
Ch–1	The first chamber (face the incoming wave)
Ch–2	The second chamber
Ch–3	The third chamber
Ch–4	The fourth chamber
FVM	Finite Volume Method
HRIC	High–Resolution Interface Capturing
LWT	Linear wave theory
MC–OWC	Multi–chamber oscillating water column
MHL	Manly Hydraulic Laboratories
NWT	Numerical wave tank
NRMSE	Normalized Root Mean Square Error
OWC	Oscillating water column
PTO	Power take–off
RANS	Reynolds–Averaged Navier–Stokes
SST	Shear stress transport
SWL	Still water level
UTS	University of Technology Sydeny
VOF	Volume of Fluid
WEC	Wave energy converter

Chapter 1 : INTRODUCTION

1.1 Background and Prospects

Renewable energy sources have a fundamental role in the reduction of air pollution, especially CO_2 emissions. Solar, wind and ocean energies are being rediscovered as a future source of zero–emissions energy [1]. Globally, renewable energy is becoming an essential part of future energy plans of many countries, and it is expected to grow faster than any other energy source. Power generation from renewable sources rose by 17% over the past year (2017) demonstrating a social acceptance and the economic viability of renewable energy deployment. Therefore, 67 countries have recently changed their renewable energy support policies and set renewable energy targets [2]. For instance, the Australian Government has revised the Renewable Energy Target (RET) to be 45,000 GWh/yr by 2020 [3].

Among all the renewable energy sources, ocean wave energy is a promising area for research. There is a growing interest around the world in the utilisation of wave energy for electricity generation. The theoretical estimation of the total amount of ocean wave energy potential is 32,000 TWh/yr, which represents approximately twice the annual global electricity demand of 17,000 TWh/yr in 2008 [4]. Reguero et al. [5] recently provided a new estimation of the global potential wave energy by considering the direction of wave energy and the world coastline alignment. They found that the potential energy resource ranges from 16,000 to 18,500 TWh/yr, which is comparable to the global electricity consumption of about 21,200 TWh in the year 2016 [6]. It is estimated that between 2000 and 4000 TWh/yr of energy can be extracted worldwide from waves because it has both potential and kinetic energies [7]. The majority of ocean waves are wind generated, and they contain roughly 1000 times the kinetic energy of wind (Power density 1 kW/m^2 at 12 m/s) [8, 9]. Furthermore, wave energy is more predictable and stable than wind and solar energy [10]. On the other hand, the wave energy sector is often seen as a confused and risky business by investors and policymakers due to the lack of design consensus and the high Levelized Cost of Electricity (LCOE), which is higher than for any other renewable energy technologies [10-12].

For a long time, the possibility of extracting ocean wave energy via Wave Energy Converters (WECs) has been investigated, and results have indicated that ocean wave energy can be harvested by the WECs and converted into a usable form of energy, e.g. electricity [13, 14]. As a result, many WEC concepts have been proposed, with the first recorded patent filed in 1799 by Girard and Son, and the first operating system was an Oscillating Water Column (OWC) device that supplied a house with 1 kW in 1910 [15]. However, globally, the commercial exploitation of these technologies are still limited compared to Solar PV that represents about 47% of the newly installed renewable power capacity in 2016, with the wind power and hydropower contributing 34% and 15.5%, respectively [16]. At present, most of the technologies for wave energy extraction are still in the infancy stage of development, and there is a very limited number of WEC devices that are suitable for a commercial pilot demonstration stage, especially in countries with extensive coastlines, such as Australia, Denmark, Ireland, Portugal, U.K., and the U.S.A. [15, 17, 18].

The design and development of WECs is a complicated, long–term (starting from scientific first principles, then proof–of–concept prototypes and forward to the commercialization stage) and expensive process [14, 19, 20]. During this process, there are multiple areas that need to be studied and analysed to help develop these technologies and the associated project deployment. There is no single method for the assessment of WEC development and performance, but the Technology Readiness Level (TRL) can be considered as a standard indicator for the advancement in the design and construction of a WEC [21].

OWC devices are considered one of the most successful technologies for harvesting ocean wave energy [22, 23]. This device was initially studied in the 1940s by Yoshio Masuda who developed a navigation buoy powered by an OWC device [24]. The OWC device can be a shoreline–based structure, such as the Portugese Pico plant and wavegen–LIMPET [25, 26] or be combined with a breakwater, such as at Sakata Harbour, Japan [27]. They can be near–shore and ocean–bed–standing structures, such as the PK1 prototype that was developed by Oceanlinx Ltd in Australia and tested in 2005 [28], or a floating platform such as the Mighty Whale that was developed in Japan [29]. The main aim of future development phases of WECs is the installation of multiple devices in array configurations, which is expected to increase, in a more economical way, the amount of wave energy extracted [30, 31].

Most previous research on OWC devices were centred on onshore and offshore isolated devices (i.e., with only one chamber). The optimum performance of these devices is usually obtained at chamber resonant period [24]. Thus, there are very limited studies on the concept and performance of multi–chamber OWC (MC–OWC) devices. The Seabreath is considered as an example of a floating multi–chamber OWC device, and it has been under development at Padova University, Italy since 2008 [32, 33]. However, limited research has been published on this device. For instance, Martinelli et al. [32] built a lumped model to simulate the airflow inside the pipes of the Seabreath device, which was then used to assess the device efficiency based on the Italian sea environment. Another multi–chamber OWC system is the LEANCON, which is arranged in two rows in a V–shaped formation. The hydraulic mechanism of the LEANCON model was designed by Rasmussen [34] and tested at Aalborg University in Denmark [35]. A similar MC–OWC device consisting of a large floating structure made of two legs forming a V–configuration at a 90–degree with 32 chambers was physically and numerically tested at the University College Cork, Ireland [36].

To move any OWC devices from the prototype stage to a more developed and complete technology like wind and solar technologies, a further research effort is still needed. Therefore, in this project, the development of a MC–OWC device will be studied through successive stages of experimental testing and numerical modelling on a small–scale.

1.2 Research Objective

Australia has one of the best wave energy resources in the world [3]. The wave energy resource around Australia could contribute up to 10% of Australian renewable energy needs by 2030 [37]. New South Wales (NSW), Australia, has coastal towns and cities that have many ports and jetties that could be good locations for WECs. Therefore, a MC–OWC scale device with four chambers was built in the University of Technology Sydney to be considered for a long–term research project. The design of this device was based on several years of research. Dorrell et al. [38] tested the first design of three–chambers OWC device at the University of Glasgow in 2003 and then performed initial verification of the model concept [39, 40] followed by a series of studies to develop a mathematical model that describes the hydrodynamic performance of two and three chambers OWC devices [45–49]. In 2012, Hsieh et al. [41] built and tested a wave tank scale model of a side–mounted OWC device consisting of two chambers equipped with two Savonius turbines. Three years later, the initial testing of a new configuration based on a four chamber OWC device concept was carried out under regular wave conditions [42].

Although the above–mentioned research on MC–OWC devices delivered a good understanding of device performance, the effects of power take–off (PTO) damping on water surface elevation inside the chamber, air pressure, airflow rate and device capture width ratio under different incident wave conditions have not yet been investigated. Therefore, this project contributes to the existing knowledge by addressing omissions in previous work by putting forward detailed explanations of the wave period, wave height, device draught and effect of PTO damping on a MC–OWC device performance using a combined numerical and experimental approach as shown in Figure 1.1.

The main objectives of this research are summarised as follows:

[1] Perform a series of experimental tests for a MC–OWC device at two different scales under regular and irregular wave conditions.

[2] Investigate the influence of wave conditions, device draught and PTO damping on the hydrodynamic performance of a MC–OWC device.

[3] Develop a simplified numerical model in the time–domain using a MATLAB/Simulink environment to describe the hydrodynamic behaviour of a MC–OWC device in regular waves.

[4] Assess the accuracy of CFD modelling, using the RANS–VOF solver in STAR–CCM+ code, in simulating the hydrodynamic behavior of a MC–OWC device in regular waves against the experimental results.

1.3 Original Contributions

The author considers that the main contributions of this thesis to the field of wave energy are as follows:

[1] Produce high–quality and reliable experimental data investigating the performance of a MC–OWC device under regular and irregular wave conditions, different PTO damping values and device draughts.

[2] Develop and validate a simplified time–domain model to represent significant parameters and describe the hydrodynamic behaviour of a MC–OWC device in regular waves.

[3] Develop and validate a 3D CFD model based on RANS–VOF approach for the MC–OWC device.

[4] Experimentally and numerically highlight the influence of wave height, wave period and PTO damping on the capture width ratio of testing MC–OWC device.

[5] Experimentally identify the effect the chambers draught have on the capture width ratio of the MC–OWC device.

[6] This study demonstrates the significance of the present MC–OWC device by showing its advantage of being more efficient in energy extraction in comparison with what has been reported in previous research.

1.4 Publications from this Thesis

I. Journal Papers

[1] Shalby M, Dorrell DG, Walker P. Multi–chamber oscillating water column wave energy converters and air turbines: A review. Int J Energy Res. 2018;1–16. https://doi.org/10.1002/er.4222.

[2] Shalby M., Elhanafi A., Walker P., Dorrell DG. CFD modelling of a small-scale fixed multi-chamber OWC device. Energy. Submitted November 10, 2018.

II. Conference Proceeding

[3] Shalby M, Walker P, Dorrell DG, Elhanafi A. *Validation of a Numerical Model for a Small Scale Fixed Multi-Chamber OWC Device*. In: Proceedings of the Thirteenth Pacific-Asia Offshore Mechanics Symposium, October 14-17, Jeju, Korea; 2018.

[4] Shalby M, Walker P, Dorrell DG. *Modelling of the multi-chamber oscillating water column in regular waves at model scale*. In: Proceedings of the 4th International Conference of Energy and Environmental Research, Energy Procedia, July 17-20, Porto, Portugal; 2017.

[5] Shalby M, Walker P, Dorrell DG. *The investigation of a segment multi-chamber oscillating water column in physical scale model*. In: Proceedings of the 5th International Conference on Renewable Energy Research and Applications, November 20-23 Birmingham, UK; 2016.

[6] Shalby M, Walker P, Dorrell DG. *The Characteristics of the Small Segment Multi-Chamber Oscillating Water Column*. In: Proceedings of the 3rd Asian Wave and Tidal Energy Conferance, October 24-28 Singapore; 2016.

1.5 Thesis Layout

This section provides more details on the work carried out for this research project as well as a brief overview of the following chapters.

Chapter 2:

This chapter presents a detailed review of the current state of MC–OWC wave energy converters developed for testing in laboratory conditions. It focuses on the mathematical modelling, experimental model structure, PTO development of particular research programs and the challenges that MC–OWC devices need to overcome to become economically feasible and be able to be compete with existing alternatives.

Chapter 3:

This chapter presents the fundamental theories required for this thesis and used in ocean wave converter technologies. Initially, the required background information about numerical models is presented to introduce the topics for research. Hydrodynamic conversion efficiency calculations that were used to evaluate the performance of the device are presented. To complement this work, a brief exploration of relevant literature is performed in each relevant chapter to identify the important aspects of research, as necessary.

Chapter 4:

This chapter deals with the first physical test–setup of the small–scale model (1:25) in the wave flume of the Renewable Energy Lab at the University of Technology Sydney (UTS). Following, the laboratory test–setup and results of model scale (1:16) in Manly Hydraulic Laboratories are presented. The device hydrodynamic performance tests in regular and irregular waves have been carried out for different design parameters such as wave conditions, device draught and PTO damping. Then these results were used for the validation of numerical models. Finally, uncertainty analyses for the experiments were performed to ensure high quality and reliable measurements in accordance with the method adopted by the International Towing Tank Conference (ITTC).

Chapter 5:

In this chapter, a simplified time–domain model is presented. Governing equations of the rigid piston model and thermodynamic model are firstly presented, then they have been solved in a time domain and implemented in MATLAB/Simulink using the ode45 numerical solver. The physical measurements conducted at the UTS wave flume (Chapter 4) are employed to validate these models. The accuracy of the MATLAB model has been tested through multiple comparisons between numerical and experimental results for crucial variables, namely water elevation inside the chamber, air pressure and airflow rate, under one regular wave condition. Good agreement was achieved. The time–domain model was also used to get a preliminary characterization of the range of values of the water surface elevation, differential air pressure inside the chamber and airflow rate, which might be useful for the setup of laboratory experiments on the OWC device.

Chapter 6:

In this chapter, an incompressible three–dimensional CFD model is developed to simulate the MC–OWC device tested at the UTS wave flume. Firstly, a numerical wave tank (NWT) was developed. A MC–OWC device was incorporated into the 3D NWT and tests were then conducted. Secondly, the numerical and experimental test results were compared. Then, the validated CFD model is used for a benchmark study of 84 numerical tests. These investigate the effects of pneumatic damping caused by the power take–off (PTO) system of a MC–OWC device. Finally, the performance is assessed for a range of regular wave heights and periods.

Chapter 7:

This chapter includes the final conclusions and the main findings of this research. Also, recommendations for future research are given.

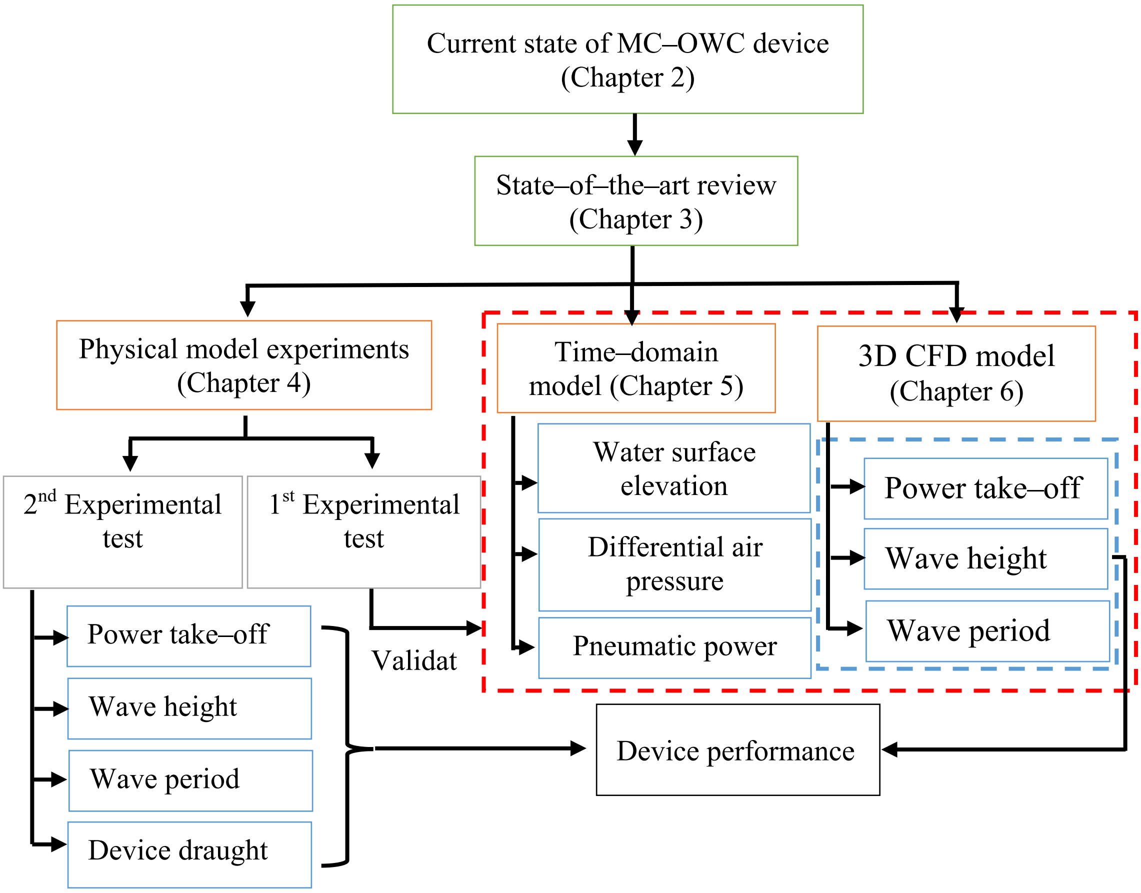

Figure 1.1. Methodology adopted in this work

Chapter 2 : LITERATURE REVIEW OF MC–OWC DEVICES

2.1 Background

The oscillating water column (OWC) is a more common type of wave energy converter (WEC) that has been the subject of study and development for several decades. Multi–chamber oscillating water column (MC–OWC) devices or arrays have the advantage of being more efficient in energy extraction compared to a single chamber system, particularly in more chaotic sea states. A variety of single and array OWC devices have been proposed and studied on a small–scale, whereas few large–scale devices have been tested under ocean wave conditions. This chapter provides a concise review of the current state of MC–OWC device development in laboratory conditions. The review in this chapter is based on the available information in the literature from 2003 to 2012.

2.2 Wave Energy Converters

During the last four decades, inventors and scientists have presented many ideas based on different mechanisms to convert wave energy into electricity. There are approximately eighty–one different concepts under development for wave energy extraction [2]. However, they are all at an early stage of development compared to Solar PV which represented about 47 % of newly installed renewable power capacity in 2016, while the wind and hydropower contributed 34 % and 15.5 %, respectively [16].

WECs can be categorised by their location, type of structure and power take–off (PTO) mechanism by which energy can be harvested from the waves. Most WECs can be both bottom–mounted and floating structures. Clément [15] categorised the main types of wave energy converter based on their operating principle, of which there are four types: 1) oscillating water column (OWC); 2) overtopping device; 3) point absorbers; and 4) oscillating wave surge converter.

The other classification often used is based on the distance from the coast: 1) shoreline WECs which are located at the shore and can be placed on the sea bed in shallow water, integrated into a breakwater, or fixed to a rocky cliff; 2) nearshore WECs which are located several hundred meters, or a few kilometers, from the shore (shallow water); and 3) offshore WECs which are floating or submerged devices in deep water [43].

WECs technologies that are currently in development are at various stages and some device technologies are more advanced than others [8] though there is still no clear technology that is leading in terms of development. However, the oscillating water column (OWC) device is one of the oldest and the most widely researched type of wave energy converter. The mean capture width ratio of the OWC device is about 29 %, while it is about 16 % for point absorber devices and 17 % for floating overtopping devices. These statistics are based on a collection of published results [44]. Moreover, it has been shown that the OWC concept can operate in different locations and on various collector platforms [18]. Heath [45], summarized the main attractions of the OWC on a practical level: 1) it has few moving parts; 2) there are no moving parts underwater or at the water level; 3) it is adaptable and can be used on the shore, in the near–shore region or floating offshore; and 4) it is reliable and easy to maintain [46]. The OWC device continues to have many of its aspects researched. This includes control [47], turbine speed optimization [48], generator selection [49], turbine inertia considerations [50], power maximization [51], permanent–magnet generator operation with irregular waves

[52], short–term wave prediction for operational improvement [53], and use of impulse turbines[54].

In general, it possible to summarise these classifications for existing wave energy converters in Figure 2.1.

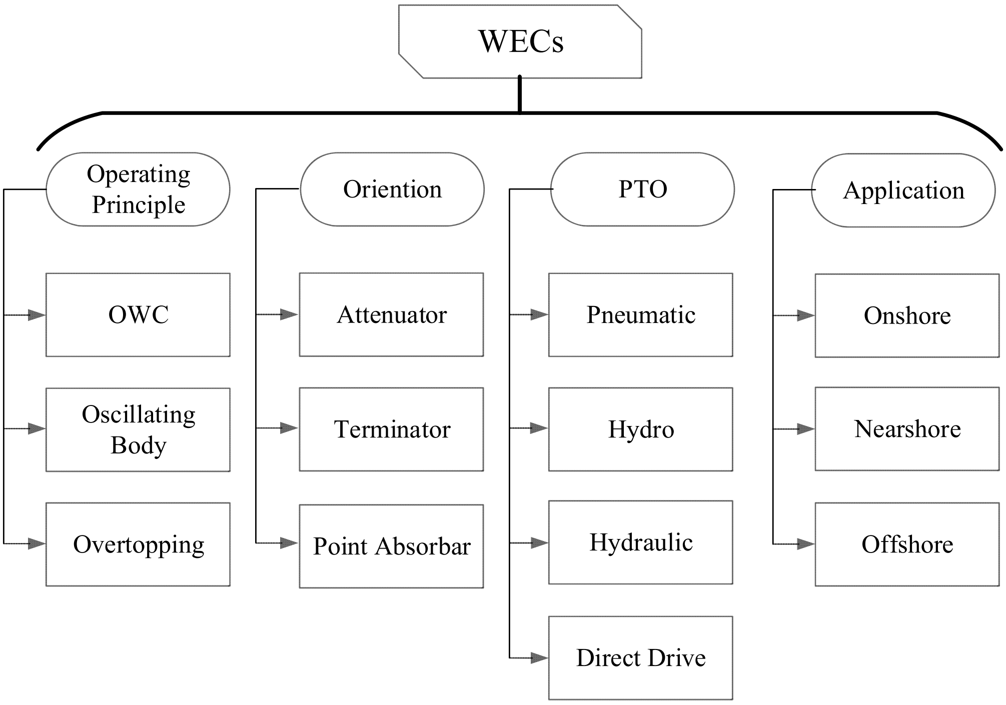

Figure 2.1. Summary of standard classification for wave energy converters, adapted from [55].

2.3 Developing Challenges

Several devices have operated in real oceans, but the most powerful wave energy devices were constructed by Osprey in the UK (1995), and by GreenWAVE in Australia (2014). Both prototypes were deployed near–shore, rated at 1 MW, and were lost in storms. Recently, the deployment of OWC devices was successfully completed at Jeju Island, South Korea, which worked with a rated power of 500 kW. These successful devices show that major obstacles can be overcome with further research [24].

The OWC is one of the most common and mature WEC devices and has seen a steady improvement in its design. Conceptual studies on multi–chamber or an array of fixed and floating OWC devices have been carried out recently [56]. Researchers and companies proposed the MC–OWC model to harness the maximum available energy. It has now been established that the MC–OWC can enhance device performance compared to a single chamber OWC [57]. Some studies have been reported about multi–device deployment or multi–section devices. The multi–chamber oscillating water column (MC–OWC) device can be considered as a multi–section device. An example of a multi–device deployment is the Pelamis; the UK planned to developed the first commercial wave farm with three 750 kW Pelamis wave energy converter devices, and a prototype was installed in Portugal [58], though this project was cancelled sometime after 2010 due to technical difficulties. A multi–section device is the Seabreath, which is a floating attenuator device equipped with an impulse air–turbine and with a valve for airflow control. This is under development at Padova University, Italy [32]. It comprises a set of rectangular chambers with open bottoms aligned with the propagation direction of the incident waves. Another multi–chamber OWC system is the LEANCON, which is arranged in two rows in a V–shaped formation. The hydraulic mechanism of the LEANCON model was designed by Rasmussen [34] and tested at Aalborg University in Denmark [35]. A similar MC–OWC device consisting of a large floating platform comprising two legs joined at a 90–degree angle in a V–configuration with 32 chambers, was physically and numerically tested at the University College Cork, Ireland [20, 36].

To have an MC–OWC as a device that is able to exploit wave energy, several challenges need to be tackled to successfully create a reliable machine that is economically viable at the same time. Therefore, the MC–OWC device needs further development of the technology to prove reliability, robustness and Annual Energy Output and to reduce deployment costs and reduce risks. In general, the design and the construction stages of a WEC are not simple, with several challenges at each stage. Clément [15] summarized these challenges as 1) the wave amplitude, phase, and direction are irregular; 2) the structural loading in the event of extreme weather conditions; and 3) the coupling of the irregular, slow velocity (frequency < 0.1 Hz) of a wave compared to the electrical generator. A generator requires up to 500 times frequency increase (to, say, 50 Hz or 60 Hz). There have been many attempts to overcome these challenges. Most solutions proposed a device that has a significant amount of moving mechanical parts and moorings. Despite the significant research and development achieved, the challenges mentioned above have still not been fully addressed.

MC–OWC devices are considered relatively new as a concept compared to other types of OWC device [32]. Some MC–OWCs have been developed and studied (e.g., LEANCON and Seabreath); however, they have not yet been commercially deployed [33, 34]. The research and development that has been carried out on the concept of a shoreline multi–chamber/array OWC has contributed to significant solutions to the essential challenges. These solutions address reducing deployment costs and increasing its ability to capture energy, especially in the locations where the waves have low and complex energetic content [59]. The results of the study show that MC–OWC devices have the advantages of 1) being suitable for a shoreline location such as a harbour wall, breakwater or wharf which will reduce the WEC establishment cost. Furthermore, this reduces the operating and maintenance costs which have an impact of about a 30% of the total cost of the WEC [56, 60]; 2) reducing the wave attenuation of the internal water height which is considered as one of the major design challenges for a WEC [8];

3) being more efficient than other single WEC when the waves are in random directions and not orthogonal to the device chambers [61]; 4) allowing the waves to penetrate and continue propagating after transferring power to the chambers because it can be side–mounted [41]; and 5) the power output is smoothed compared to a single chamber OWC. This reduces the pulsing load applied to the turbines and PTO [8, 41].

MC–OWC devices are designed to be deployed in the shoreline or nearshore. These locations are associated with many disadvantages such as a lower wave power due to shallow water and shoaling effects, tidal range, and shoreline geography [62]. However, several studies were carried out in order to assess the feasibility of WECs in low energetic sites [63, 64]. Integrating of an OWC device into a breakwater or part of the harbour is an investment that could be a solution that would make WECs competitive with other renewable energy technologies; this would be a significant step forward in terms of OWC device deployment [65].

To date, several WEC reviews have been published [1, 24, 43, 62, 66]. However, few have addressed the concept of the MC–OWC device. Therefore, there is a gap in the review literature; this may affect the development process of the MC–OWC device and review may aid this technology and push it towards the commercial stage. This chapter will cover a systematic review of the development stage of a MC–OWC device that contain two, three or four chambers. It has been carried out using information in the literature over the period from 2003 to 2012. The approach adopted in this chapter focuses on the mathematical modelling, experimental model structure and PTO development of a particular research program. The connection between the turbine and generator in the PTO system, and the electrical theory used to calculate the power, have not been covered in the chapter. Instead, the hydrodynamics and mechanical operation are the focus.

2.4 Working Principles

An OWC consists of two primary components: the chamber and the turbine. Waves propagate into or across the front of the chamber so that the water elevation inside the chamber oscillates with height and phase which are different from the wavefronts. When the water level rises and falls, air is pressurised and depressurised, respectively, so that air moves into and out of the chamber via a bi–directional turbine [67], or unidirectional turbines with suitable ducting [68]. This work focuses on the OWC device that consists of aligned rectangular chambers (two, three or four chambers) with open bottoms; it operates in parallel with the wave direction and shares single or multiple air turbines. In terms of the standard classification of WECs, such a device could be categorized as a fixed or a floating OWC device [69]. Figure 2.2 shows two different configurations of the MC–OWC. The crucial difference between this device and a standard OWC is that the column is segmented, and waves travel across the front of the column as shown in Figure 2.3 (b) (orthogonal configuration) rather than on–coming into the column as shown in Figure 2.3 (a) (parallel configuration).

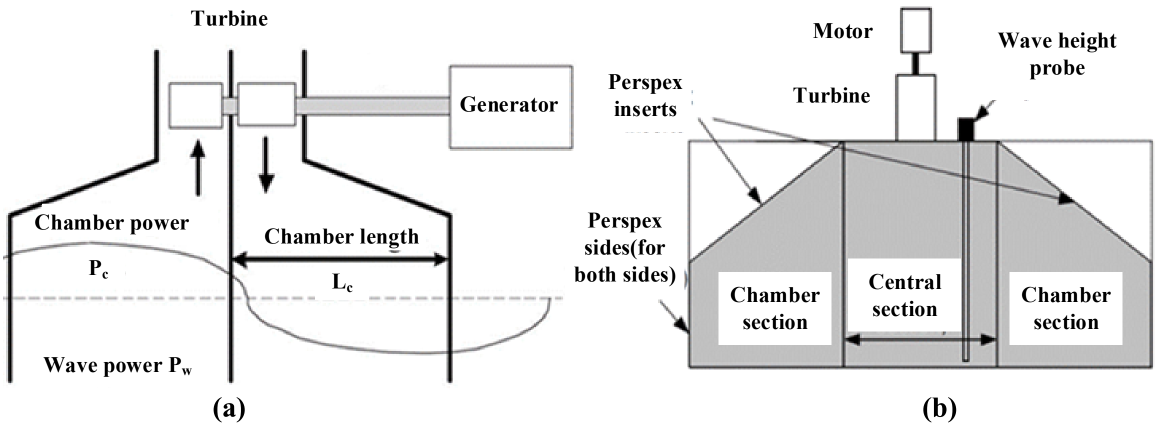

Figure 2.2. Schematic of multi–chamber OWC,(a) Two chambers [41], (b) Three chambers [60, 61]

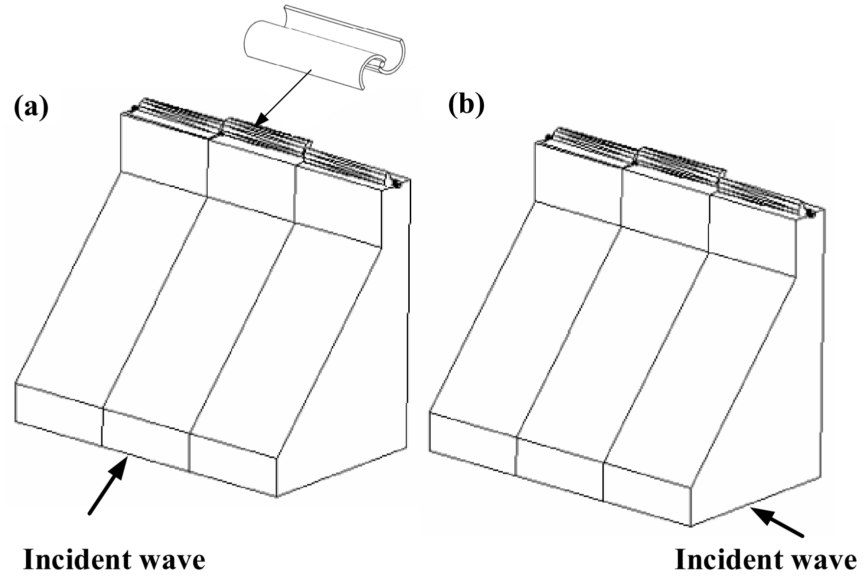

Figure 2.3. Chamber cross section: (a) Parallel configuration; (b) Orthogonal configuration [61].

2.5 Multi–Chamber OWC Device Development

In existing WECs design guidelines, the guideline for each stage provides a general understanding of the device at that stage, beginning with theoretical analyses and extensive experiments carried out on small scale devices and conducted in a wave tank. In this section, a stage development approach is used to describe the studies conducted on MC–OWC devices that have been developed in a period of 2003 to 2012 which are summarized in Table 2.1. To give a better understanding of the development stages, progress can be gauged by reviewing some key developments in the following sections.

Table 2.1 The main stages and study history of the OWC device considered in this chapter

Stages	Duration	Location	Description	PTO
Stage 1 Concept validation	2003–2007 [39, 70-72]	A three–chamber model was tested with two different configurations (parallel and orthogonal to the incident wave) at the University of Glasgow.	A small–scale model consistting of three sections with one main turbine was designed and used as a teaching and research tool. This model was put forward to produce 1 kW.	One main Wells turbine with one and two–stages installed over the chamber central section with DC motor connected to a supply. A three Savonius rotor connected to the same drive shaft.
Stage 2 Proof Concept	2008–2009 [60, 61]	The design scale and the operation of the water column were tested in a wave tank with varying frequency in Taiwan.	A hydrodynamic analytical model was developed to describe the model operation.	Savonius turbine mounted on the top of the chamber and connected in–line with a brushless permanent–magnet generator.
Stage 3 Design model	2010–2012 [41]	Lab tests based on the wave conditions of the east coast of Taiwan.	A two–chamber intermediate–scale (1:11.62) device was tested in a wave tank for wave conditions based on the east coast of Taiwan.	Each chamber had one Savonius turbine on top and connected in–line.
Stage 4 Current work	2015–present [73]	The initial model was designed to complement a research project at the University of Technology Sydney.	The model has four chambers that divide the incident wave into four parts to allow each chamber to run as an OWC.	PTO was implemented through a circular orifice.

2.5.1 Initial Concept Validation

The WEC design development process extends from applying fundamental laws of physics at the initial concept to the proving stage, and then to commercial demonstration [74]. Most new devices have schemes that incorporate some unproven concepts or designs that should be verified before performing more extensive tests.

However, some developers have moved quickly to the stage of pursuing industrial development of these devices for large scale energy production [15].

The first attempts at the development of MC–OWC have taken place at the University of Glasgow in 2003. [72]. Dorrell et al. [72] described the initial work which developed a wave energy converter model. This was used as a teaching tool to aid the understanding of the principles of the wave energy generation. The fundamental model structure was made up of a line of three rectangular chambers as seen in Figure 2.2(b). This model has been subject to a series of tests carried out to estimate the initial hydrodynamic performance of the three–chamber OWC device equipped with a small–scale Wells turbine. In parallel, the linear wave theory was developed to represent wave motion interactions and energy forms as outlined in Section 2.6. The theoretical results were compared to experimental results of the full–scale device similar to the Mighty Whale device in Japan [75]. The study in this period (2003 to 2006) led to the conclusion that the initial model design needed more experimental verification and accurate mathematical modelling of the system to improve efficiency and optimise the device geometry. Moreover, the small–scale Wells turbine that was utilized during the physical test showed low efficiency. So, a Savonius turbine was proposed for the following investigations. This turbine consists of two curved blades forming an "S" shape in cross–section which is similar in design to the vertical–axis wind turbine (VAWT) [76]. Further details will be presented in Section 2.7

One of the critical aspects that have been considered in the initial validation stage is the effect of the device alignment on the turbine performance. Thus, the OWC model in Figure 2.2 (b) was updated to the device as shown in Figure 2.3 with a Savonius rotor which demonstrated an acceptable efficiency in the small–scale tests as presented in

Section 2.7.2. Besides, a mathematical algorithm was developed to predict the performance of the OWC device.

To study this issue, the parallel and orthogonal configuration of the device demonstrated in Figure 2.3 (a) and (b) was tested in wave tank conditions. The first configuration was designed to fit within the available wave tank, so the front face of the chamber acts as a beach as seen in Figure 2.3 (a). The front face of the model was covered with a material that would absorb wave energy and reduce wave reflection, so that wave reflection was almost eliminated. This configuration is much like the LIMPET device which was installed on the western coast of Scotland [77]. The second configuration model was placed orthogonal to the incident waves as in Figure 2.3 (b), so the incident wave continues to propagate without a reflection wave back to the wave tank paddle. A series of tests were carried out for both configurations to study its performance under constant wave height and different wave frequencies. The results of a test of the parallel configuration device showed that the relationship between the output power and the turbine speed is a nonlinear relationship under the wave frequencies 0.55 Hz and 0.8 Hz as shown in Figure 2.4(a) while this relation was linear for the second configuration test under the same wave conditions as shown in Figure 2.4 (b) [78].

In this section, the initial test was conducted to verify a concept of two OWC devices with Wells and Savonius turbines which was performed in regular wave conditions. However, further experimental and simulation work was required to assess the impact of design variables and environmental parameters which were considered as one of the aims of the WECs development in this stage.

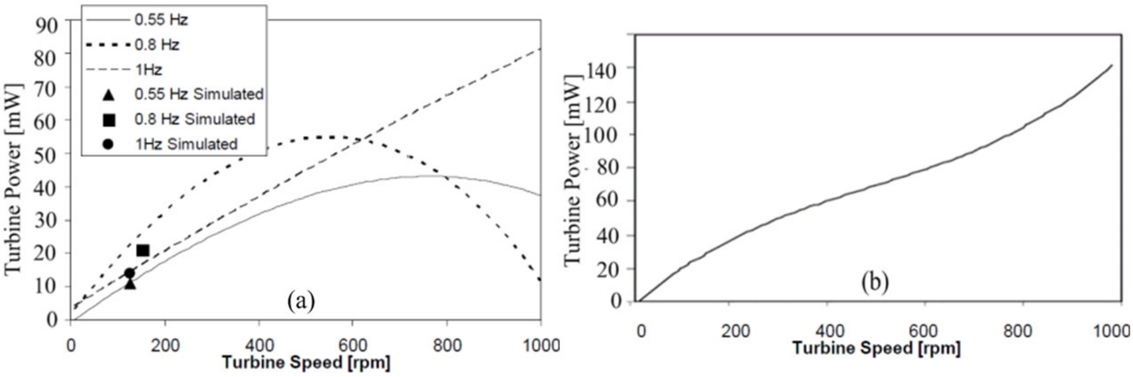

Figure 2.4. Power against turbine speed: (a) Face positioning; (b) Orthogonal positioning [61].

2.5.2 Proof of Concept

In the previous section, the initial concept of the device was presented. The most significant variance of the MC–OWC from the single chamber OWC is the direction of the device, orthogonal positioning of the MC–OWC device is used so that waves pass the device. The mathematical model derived in the previous stage was developed to evaluate the primary design variables, such as chamber length and turbine size. Further details will be introduced in Section 2.6. The model studied in proof of concept stage had an overall length of 4.5 m, it is equally divided into three sections as shown in Figure 2.5(a) and (b). It has been tested in the large wave tank (water depth 3.35 m) under regular wave conditions with intermediate wavelength ranges and a variation of wave heights. The model was equipped with three Savonius rotors installed on the top of each chamber sections and connected in–line with a permanent magnet Direct Current (DC) machine which is used to act as the generator for the system as seen in Figure 2.5 (a).

In parallel with the physical testing, Dorrell et al. [79] utilized a Computational Fluid Dynamic (CFD) analysis to study the performance of a Wells and a Savonius turbine.

The simulation and experiment results of the test of this device showed that the Savonius rotor does not have a high conversion rate, and its output power is limited over the test conditions. In the tests, the airflows of the three chambers are merged into one. Therefore, a single Wells turbine was assessed on the upper part of the OWC segments as shown in Figure 2.5 (c).

The theoretical results in the proof of concept stage allowed the developers to propose a first design procedure to represent turbine sizing design calculations. For instance, they calculated the turbine diameter (0.45 m) that could be used to design a 1 kW device if there is a theoretical conversion rate of 16 % as reported in [80].

The work presented in this section was the catalyst for subsequent research which concentrated on a possibility for performance optimisation, scaling of the model, and construction of efficient turbines for delivering higher power.

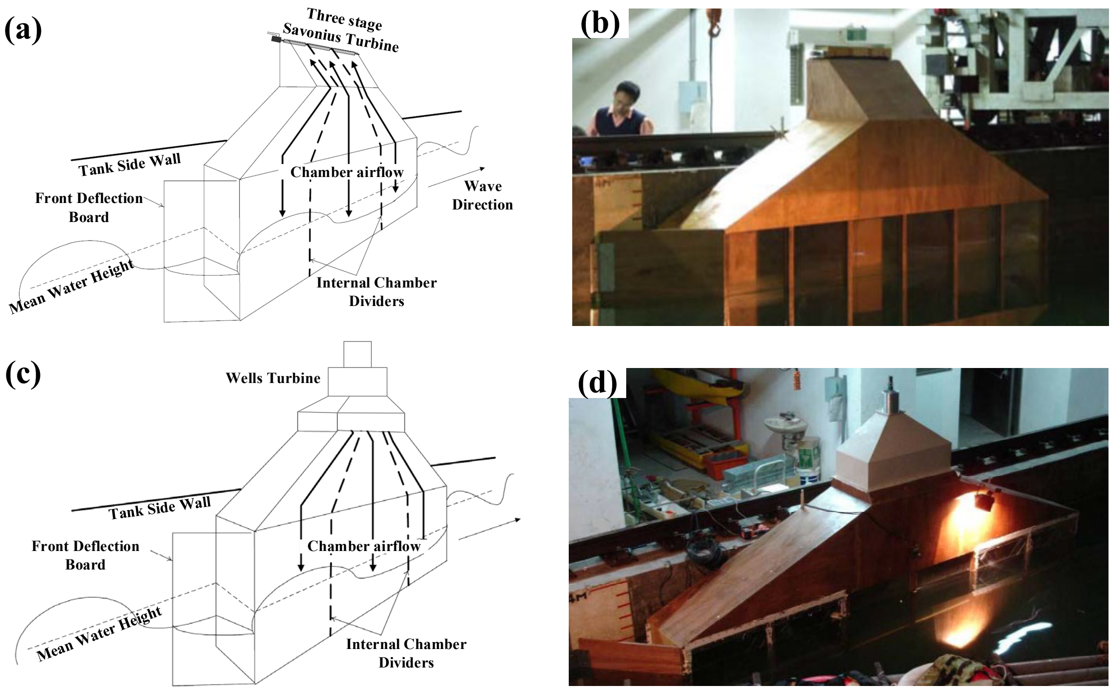

Figure 2.5. Segmented OWC devices arrangement, (a): Schematic showing the arrangement of MC–OWC with Savonius rotor; (b): A photo of the physical scale model three–segment OWC with Savonius rotor; (c): Schematic showing the arrangement of MC–OWC with Wells turbine; (d): A photo of the physical scale model arrangement with Wells turbine [79, 80].

2.5.3 Design Model

In the previous two sections, the experiment and simulation results provided an estimation of the energy production capacity of the proposed models shown in Figure 2.5. Seven years after the first work, Hsieh et al. [41] developed a two chamber OWC model as shown in Figure 2.6. This design of the model was, in part, based on the design related of the devices in earlier research work (three–chamber OWC models). It was tank–tested using scaled–down waves based on the wave conditions around Taiwan. This step was considered the earliest step towards device marketing which was not included in the preliminary implementation plan.

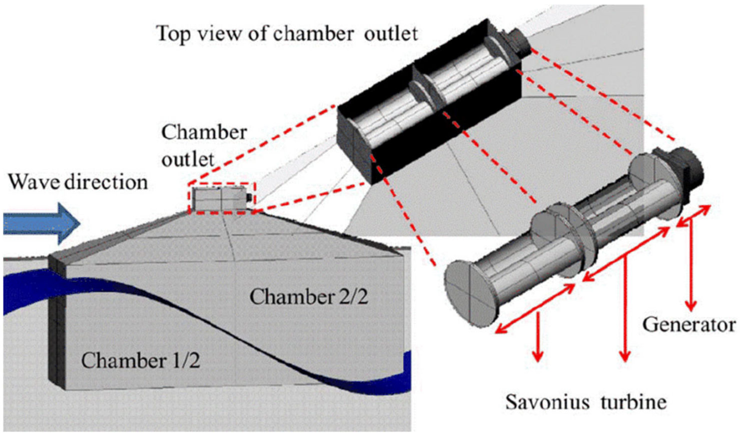

Figure 2.6. Schematic of two–segmented OWC [41].

The model was built based on the Froude scaling factor $\lambda = 11.62$, then tested in a wave tank under deep water conditions (the water depth in the target site is 38.9 m) as described in [41].

Hsieh et al. [41] utilised analytical and experimental approaches to study the device components individually. The analytical model, which was developed in the previous work, was verified by experiment results and found to be in a good agreement. The analytical model was then simplified to study the oscillating wave surface elevation inside the chamber. Two Savonius turbines were used since it was a two–chamber device. These turbines were designed using the design of the verified turbines in the previous study. The turbine performance was defined by the power coefficient which depends on the shaft torque, turbine rotational speed, sweep area of the turbine blades, and the inlet airflow velocity through the turbine. This coefficient was evaluated experimentally then it was modelled numerically using the CFD–CFX package. As a result of the Savonius turbine CFD model, the relationship between the chamber differential air pressure and the airflow rate was described.

The improvement of the analytical and experimental approach was continued in the design mode stage. Further investigations were conducted to study the impact of area ratio (the cross–section area of the chamber, A_1 to the turbine inlet area, A_2) and chamber in regular wave conditions. The area ratio is considered as the main parameter that impacts on the overall performance of the model by increasing and decreasing the airflow velocity through the turbine. The experience gained during the previous stages (initial concept validation and proof of concept) has improved the performance of the MC–OWC device. The maximum theoretical efficiency of the OWC chambers is 89.2% (with turbines and generators excluded) as reported in [41].

It is clear from this stage that the investigation was more comprehensive, where the most important achievements were:

1. The device geometry was selected based on the target site.
2. The impact of the design parameters on the device performance has been studied analytically and experimentally which was not considered before.
3. The wave conditions that allowed the device to capture a maximum power were identified.

4. The developers obtained a 13.9 % overall energy conversion rate (wave–to–wire) from the proposed model shown in Figure 2.5 which was reasonable compared to other similar systems such as the “Mighty Whale”.

2.6 Theory of Operation

Ocean wave energy is a form of solar energy; the temperature differences across the globe cause winds that blow over the ocean surface. These winds cause ripples, which grow into swells. Such waves can then travel thousands of miles with virtually no loss of energy [43]. As waves propagate, energy is dissipated at the air–water interface and between the water and seafloor in shallow water. The resultant movement of water carries kinetic energy which can be harnessed by wave energy devices.

This section describes a brief review of an overview of the hydrodynamic theories that have been used in the development stages (Section 2.3). The basic model was developed by Evans [81], who proposed the concept of an oscillating pressure on the incident water surface and its equivalence to the interior water surface of an OWC.

A set of equations was introduced for a multi–chamber OWC rather than just a single chamber OWC, but the limitation to a single device was enforced during the derivation. The theoretical development of the device can be divided into three phases. First, a mathematical model was built to describe the wave surface elevation inside and outside the chamber. Then this model was integrated with the differential air pressure in the chamber and, in particular, to the pressure drop in the turbine blades, detailing the relationship between the waves and the airflow through the turbine. Third, the mechanical characteristics have been taken into account to obtain the power available at the turbine inlet and the rotational speed and torque that is then applied to the generator [20, 24].

2.6.1 Surface Elevation

Linear wave theory was utilised to describe the wave behaviour at the first stage of development (further detail will be outlined in Section 3.2). This theory provides an equation that defines kinematic and dynamic properties of the wave surface.

The first theoretical model was formulated to describe a regular incident wave by applying Newton's Laws and using the assumptions of the linear wave theory (with waves of a small amplitude $H/2$, relative to both the wavelength L and the water depth d). The equation of a regular surface wave profile as a function of time t and horizontal distance x can be described as [78, 82]:

$$\eta(x,t)=\frac{1}{2}H\cos(kx-\omega t) \tag{2.1}$$

where $k = 2\pi/L$ is the wave number, and $\omega = 2\pi/T$ is the angular frequency. Figure 2.7 illustrates the main parameters of the chamber.

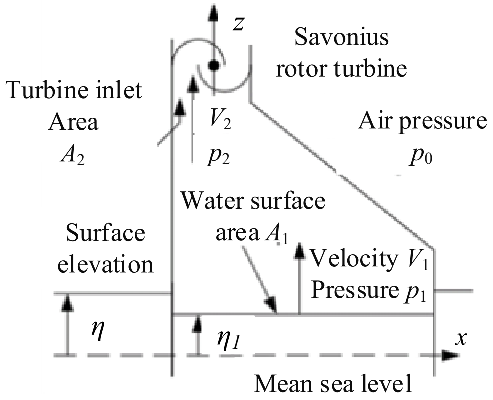

Figure 2.7. Device variables definitions [41].

Further derivations were done on the surface elevation formula to derive the internal water surface elevation inside an OWC chamber η_1, at the equilibrium position. At this point, Dorrell et al. [61] used Newton's Law $\sum F = ma$ to derive the relationship between the incident wave height and the wave height within the air chamber which was developed in [61, 83] from:

$$\left[\rho_w g\left(\eta-\eta_1\right)-\Delta p\right]A_1=\frac{d}{dt}\left(\rho_w \eta_1 A_1 \frac{d\eta_1}{dt}\right) \tag{2.2}$$

where ρ_w is the density of seawater, and Δp is the total pressure drop across the turbine.

By using a small–scale model assumption, the airflow velocity at the turbine V_2 can be obtained from the differential of the internal free surface as $d\eta_1/dt$. This relation is satisfied due to relatively low pressure ($p_1 - p_0 \approx 0$). Hence, the motion of the internal free surface can be defined, and the relationship between p_2 and p_1 can be determined.

According to the design characteristics of the MC–OWC device, the wave propagates along the chamber instead of being incident on the front wall of the chamber. Therefore, it was concluded that it is sufficient to consider the influence of the fundamental wave frequency. Further development of the expression for the water surface elevation was obtained to introduce the effects of the ratio of the wavelength L to chamber length L_c which directly relates to the wave height inside the chamber:

$$\eta\left(t\right)=\frac{H}{L_c+2\,d}cos\left(\omega t\left(\frac{L_c\,sin\left(\theta\!\left/\!_2\right.\right)+2\,d\,cos\left(\theta\!\left/\!_2\right.\right)}{\theta}\right)\right) \tag{2.3}$$

where d, is the chamber draught and θ (rad), is the angular chamber length = $2\pi \times L_c/L$

By using Eq. (2.3), the attenuation of the internal water height in the chamber was simplified to

$$\eta_i\left(t\right)=H_i cos\left(\omega t\right)\frac{2sin\left(\theta/2\right)}{\theta} \tag{2.4}$$

where i = 1, 2… is the chamber number, and H_i is water height in the chambers. This equation takes into account the depth of the chamber which is a particular modification of this arrangement. A further equation which dictates the oscillation of the water inside the chambers was obtained (see the appendix in [61] for derivation details):

$$\eta_i\left(t\right)=\frac{g.e^{i\omega t}}{g-j0.04\omega\left(A_1/A_2\right)}\eta\left(t\right) \tag{2.5}$$

During all the development stages reviewed in Section 2.5, Eqs. (2.4) and (2.5) were used to describe the fundamental oscillation of the water height inside the chamber and the airflow through the turbine. In the design model stage, it was observed, using experimental results, that there is a second harmonic content in the interior water surface elevation, but the fundamental component dominates which was validated by using the Runge–Kutta–Nystrom simulations as described in detail in [41].

2.6.2 Airflow Velocity and Pressure Change

In the proof of concept stage (Section 2.5.2), the relationship between the oscillating pressure inside the chambers $p_1(t)$ and the internal water surface elevation was derived by Dorrell et al. [78]. Firstly, the pressure over the water elevation in the chamber $p_1(t)$ (see Figure 2.7), was assumed to be negligible compared to the pressure across the turbine $p_2(t)$, which appears due to changing the interior water elevation in the chamber. The pressure across the turbine is considered as one of the terms in the expression for the power available at the turbine inlet since the air chamber is pressurised. Therefore, the pressure term and its impact on the other parameters were studied extensively during that stage of development [60, 78].

The relationship between the pressure drop through the turbine and the change in the internal water surface elevation was expressed as

$$\Delta p = f\,\rho_a \left(\frac{d\eta_1}{dt}\right) = f\,\rho_a \left(\frac{A_1}{A_2}\right)\frac{\omega H_i}{2} cos\left(\omega t\right) \qquad (2.6)$$

Further modifications were performed by combining Eq. (2.6) with Eq. (2.2) which was rewritten in a simpler form:

$$\frac{d}{dt}\left(\eta_1 \frac{d^2\eta_1}{dt^2}\right) + f\left(\frac{d\eta_1}{dt}\right) - g\left(\eta - \eta_1\right) = 0 \qquad (2.7)$$

Dorrell et al. [60] suggested three solution methods to solve Eq. (2.7) . Each method was verified and compared to experimental results. Finally, the relationship between the internal water surface elevation and air velocity, and the pressure inside and outside the chamber was obtained by solving Eq. (2.7)[60].

2.6.3 Power Available at the Turbine

The efficiency of the OWC device is one of the most important issues that should be considered in the design procedure. The theory developed in Section 2.6.2 was able to evaluate important parameters (the interior water elevation and the pressure change across the turbine) which have a significant effect on the performance of the OWC device.

Throughout the MC–OWC device development, the developers focused on two kinds of power which represent the total extracted power of the device. The first term is the power due to pressure P_t, which is a function of the pressure at the turbine inlet p_2 and the air pressure outside the device chamber p_0. The second term is the power due to airflow velocity P_a, which is the power derived from the kinetic energy of the airflow [61]. The total power available at the turbine inlet P_{in} is given as

$$P_{in} = P_t - P_a = \left[\begin{pmatrix} -\rho_a\left(\frac{A_1}{A_2}\right)\left(\frac{\omega H_i}{2}\right)^2\left(2cos\left(\omega t\right)^2 - 1\right) \\ \rho_a\left(\frac{A_1}{A_2}\right)\left(V_2 - V_1\right) \end{pmatrix} + \frac{1}{2}\rho_a V_2^2\right]\times Q \tag{2.8}$$

where Q is volume flowrate = $A_1 \times V_1 = A_2 \times V_2$, ρ is the air density, ω is angular wave frequency.

In this section, the mathematical models that were developed during the stages presented in Section 2.5 were highlighted. All the assumptions and improvements applied during the mathematical development have been confirmed to be in good agreement with results of experiments that were conducted. Therefore, such a theory plays an important role in assessing the performance and the hydrodynamic behaviour of the device.

2.7 Turbine Design and Testing

Several PTO systems have been suggested; these are considered as the most critical element in the energy conversion chain of a WEC. These usually consist of an air turbine or turbines [84], coupled through a mechanical gear–box [85] or directly coupled to a rotary electrical generator [86], or possibly connected through hydraulic systems [87]. Most proposed and tested air turbines for wave energy conversion are axial–flow machines of two basic types: the Wells turbine [41, 88] and the impulse turbine [89, 90]. Several reports provide detailed information about the performance and the running characteristics of these turbines [91-93].

Most of the research work has focused on the PTO system during the device development period that has been reviewed in this chapter. Since the first study work was conducted on the MC–OWC in 2003, the PTO system has been modelled by a Wells turbine or a Savonius turbine. This Section gives an overview of these two types of air turbine as used in small–scale MC–OWC devices, the Wells turbine (monoplane and biplane configurations) and the Savonius turbine, as a possible alternative in small–scale devices. This study uses available information on the aerodynamic performance of the turbines, especially the CFD results and the laboratory testing.

2.7.1 Wells Turbine

The Wells turbine was invented in 1976 by Wells [94]. Various types of Wells turbines have been developed and tested. A major advantage of the Wells turbine is its mechanical simplicity and relatively low cost. It requires a flow coefficient of around 0.1 so that it rotates at either a high speed or low inlet velocity to maintain the flow coefficient.

Since the first study of the OWC device by Dorrell et al. [38], they have addressed the design of the small–scale turbine. The turbine design approach was based on the geometry variables, blade profile and rotor planes [38, 70, 79]. Two Wells turbine models were proposed and tested by Dorrell et al. [70]; they were a monoplane Wells turbine (single stage) and a biplane Wells turbine (double stage) as illustrated in Figure 2.8 (a) and (b) respectively.

The first Wells turbine design was proposed and tested using the MC–OWC device in 2003 by Dorrell et al. [38]. It was made of eight symmetrical NACA15 aerofoils profile (90° stagger angle) which is a recommended profile by Raghunathan [95] for a small scale Wells turbine blade. Fixed pitch blades were used with a thickness ratio of approximately 20 % to design this turbine. The input is the pneumatic power which depends on the pressure amplitudes and the volume flow rate at the turbine inlet, which was obtained from experimental tests conducted on the small–scale MC–OWC device. This OWC device had three column sections merged into one air chamber as illustrated in Figure 2.4 (d). The turbine was connected to a DC machine and installed on the top of the chamber to test, as shown in Figure 2.4 (c). In the first series of the tests [38], the results were not satisfactory because the output power was low. The poor design was improved by introducing a biplane Wells turbine (two–stage of cross section area 0.01539 m^2) which used an optimized blade profile.

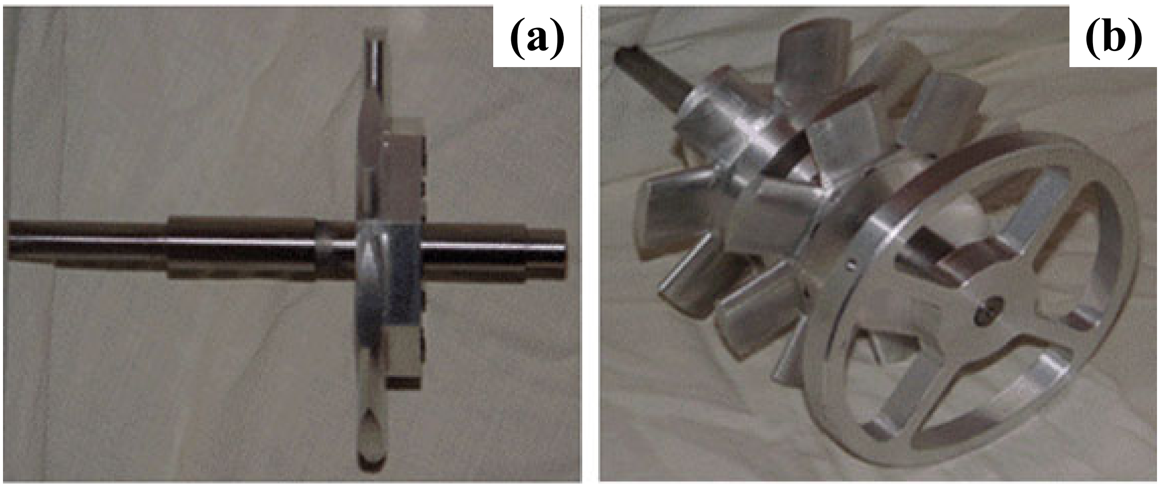

Figure 2.8. Wells turbine rotor: (a) : Monoplane (single stage); (b): Biplane (double stage) [70].

A biplane Wells turbine was then modelled and analysed by using the CFD. The CFD–CFX simulations were conducted at a constant rotational speed and alternating inlet velocity (±10 m/s) with zero reference pressure. The output from the analysis indicates that the biplane turbine had very low conversion rates at low tip speed ratio (the ratio between the tangential speed of a blade and the airflow velocity through the turbine) since the frequency of oscillating airflow in an MC–OWC was typically less than 0.1

Hz. Even with this low conversion rate, a Wells turbine still represents a viable option in a small OWC device since it is flexible and the alternatives are also going to exhibit a low conversion rate [80]. However, a scaling exercise in [48] illustrated that a larger Wells turbine has a much higher conversion rate illustrating that its performance is related to its Reynolds number and thus size.

2.7.2 Savonius Turbine

In a small–scale OWC device, airflow velocities at the water surface elevation inside the chambers were very low with a relatively low–pressure. For a turbine designed to operate under laboratory conditions, the size of the turbine will be relatively large with a relatively low operational speed. As a result of the low conversion performance of the Wells turbine, a Savonius rotor was proposed as an alternative to the Wells turbine. The Savonius rotor is a vertical–axis turbine with curved blade arrangements which is commonly used to generate energy from the wind. Figure 2.9 (a) shows one of the rotors used in the development stages. It can be arranged in series on top of the chambers so that the device chambers can be working independently. The three–chamber arrangement with three Savonius rotors is illustrated in Figure 2.4 (a) and (b) and two–chamber arrangement with two Savonius rotors is shown in Figure 2.5[78].

The system shown in Figure 2.4 (a) and (b) with a three Savonius rotor configuration was constructed to investigate the system performance in wave tank conditions at three different wave periods with a variation of the wave height. The conversion factor of each Savonius rotor was low, and the output power was inevitably small. Therefore, the Savonius turbine output power was experimentally measured by fitting a small permanent–magnet DC machine to the turbine, and the speed measured by a simple hand–held tachometer and the output power was calculated by using a simple design algorithm that was developed to overcome the low power output which showed acceptable results [78]. To improve the last selected design, a CFD–CFX simulation was developed to simulate a single rotor as shown in Figure 2.9 (b). This model was assessed under constant air velocity. The simulation results were in good agreement with the experimental results as Dorrell et al. explained in [80].

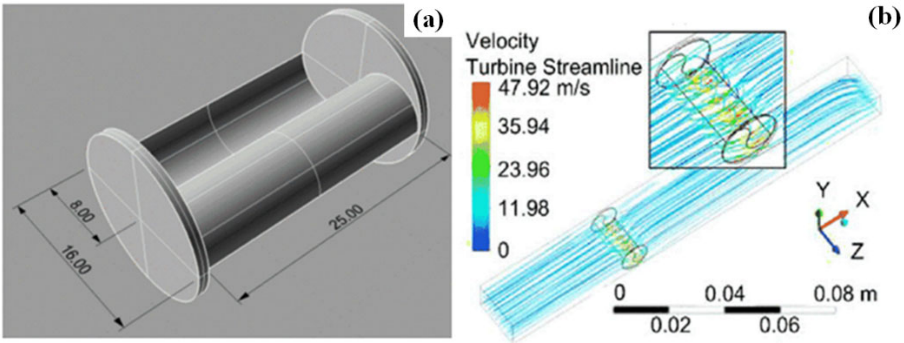

Figure 2.9. Savonius turbine, (a): Savonius rotor dimensions; (b): CFX model for Savonius turbine [61].

Since both the Wells and Savonius rotors are power modules, a comparison was made regarding power coefficient, pressure coefficient, efficiency and operating range. A Wells turbine of a similar size is likely to have an even lower conversion rate due to the low Reynolds number for these small–scale models. Therefore, in small–scale systems, a Savonius rotor is used as it provides better energy conversion. The MC–OWC devices in the studies detailed here had real PTOs and were subjected to several investigations and tests at Stages 1 and 2 of device development; the developers suggest that progress has been made towards the design of a more sophisticated device (with a scale of 1:10) with testing to be carried out under a number of sea states, including realistic survival conditions. This will take the design past Stages 1 and 2 in Table 2.1.

2.7.3 Alternative PTO Systems

The development of an efficient and reliable PTO system is the main challenge for WECs. One of the principal problems that a small–scale turbine encounters is the stall condition and mechanical losses in the powertrain. The PTO system implemented in the MC–OWC devices of the previous project uses individual turbines as illustrated in Figure 2.10 (a). However, another development is to link the turbines together as shown in Figure 2.10 (b) and cascade the air between the chambers. In [96], it was suggested to use high– and low–pressure ducts to link the chambers as in Figure 2.10 (c), and this was tested on a small–scale model. In this project, the PTO system was represented in a simplified way by an orifice to simulate a nonlinear impulse turbine, as used in [97-99]. Thus, orifice plates of different sizes were used as discussed in Section 3.4.3

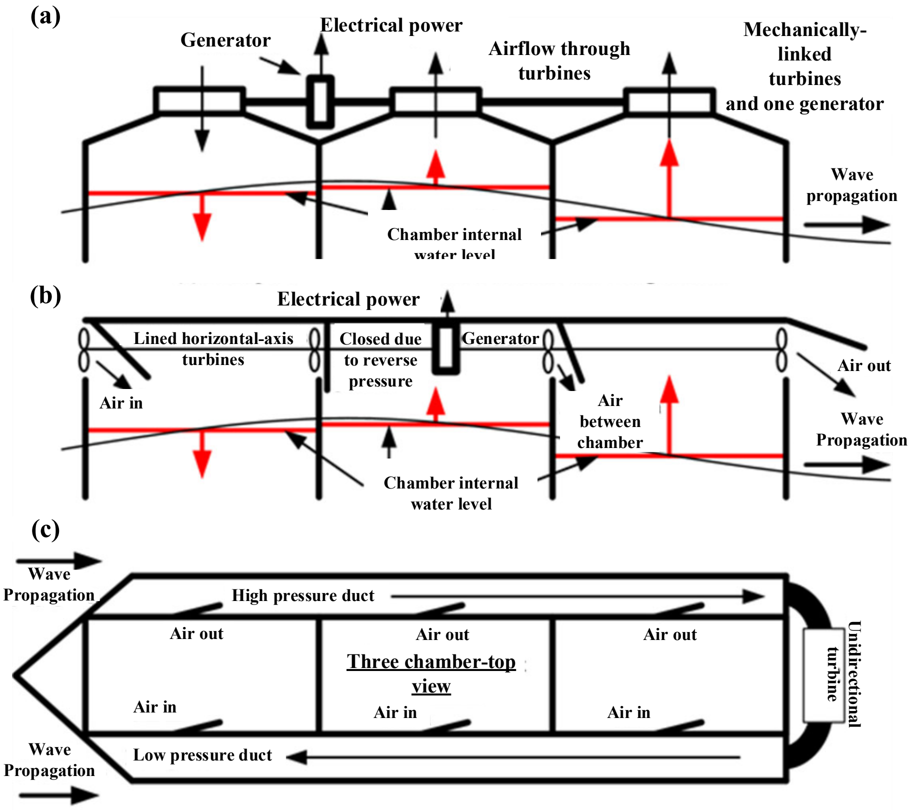

Figure 2.10. Alternative PTO systems, (a): Multiple chambers with linked turbines and one generator; (b): Cascaded chambers with linked chambers and turbines and one generator; (c): a Single unidirectional turbine with high and low–pressure ducts [96].

2.8 Summary

In this chapter, a stage development approach was used to assess the status of device development which will enable the MC–OWC device to become economically feasible and be able to compete with existing alternatives. Each stage is characterised by very specific goals and objectives which make it possible to progress systematically.

The stage developing approach highlighted that development was progressing too quickly in some phases and possibly missing significant parts of phase development, such as assessing the impact of design variables on the device performance. This work is currently being carried out. The repercussion on further development will be affected if it is not. Furthermore, the proposed model faced several design difficulties such as device geometry, the direction of the chamber with respect to the incident wave, and the PTO configuration which all have an impact on the device performance. According to this chapter, these difficulties are still not very well understood, and future research should be focused on addressing these challenges effectively since this type of WEC has not been commercialised yet.

Chapter 3 : BACKGROUND THEORY

3.1 General

The aim of this chapter is to review relevant background knowledge and the modelling of OWC devices in order to justify the choice of modelling approaches utilised throughout this thesis and to identify the specific issues to be considered in testing and modelling the MC–OWC device.

3.1.1 Ocean Wave

Oceans represent a vast source of renewable energy that can be utilised and converted to large–scale sustainable electrical power. In general, ocean energy can be divided into six types of different origin and characteristics: ocean wave, tidal range, tidal current, ocean current, ocean thermal energy, and salinity gradient [16, 100, 101]. In the ocean, waves are derived from solar energy, through wind, which when blowing over the ocean surface generates the waves [43]. The waves will continue to travel over vast distances in the direction of their formation with very little energy loss, as long as the waves are in deep water conditions. When waves reach shallow waters, they tend to slow down, the wavelength is shortened, and the crest of the wave grows [82]. Therefore, a significant amount of wave energy is dissipated in the nearshore region and by breaking on beaches [102].

Wave energy has the advantages of high energy density, low negative environmental impact, reliability and energy can be extracted about 90% of the time compared to 20 – 30% for wind and solar [4, 43]. After the oil crises in the 1970s, more attention was given to the possibility of extracting the enormous energy potential of ocean waves.

Thus, the WEC devices have made significant progress in recent years [66]. Although some research on WEC devices has been ongoing intermittently for several decades, the technology is still in the early stages of development [17]. Given the apparent advantages of wave energy and the fact that it is a relatively new technology, ocean wave energy is considered a very attractive renewable energy source with a great potential for development over the next few years.

3.2 Linear Wave Theory (LWT)

Before the discussion of the numerical models used in this work and the subsequent use of the apparatus to identify OWC device hydrodynamic coefficients, a review of the fundamental theory used to define an OWC device parameters is necessary. Therefore, this section discusses the linear wave theory (LWT) and a list of model coefficients that are required in the numerical and experimental work in this thesis.

Linear wave theory or small–amplitude wave theory is a simple mathematical formulation of the propagation of gravity waves on the surface of an ideal fluid [103]. This theory, developed by Airy (1845), provides equations that define most of the kinematic and dynamic properties of surface gravity waves and predicts these properties within useful limits for most practical circumstances [104].

3.2.1 Limitations of the Linear Theory

Linear wave theory is based on the assumption that the wave height (*H*) is much smaller than the wavelength (*L*), and that the oscillation amplitude of the moving body is small. The LWT assumes that the water, seawater or fresh water, is homogeneous and incompressible, and the viscous effects are negligible (concentrated near the bottom). Thus, no internal pressure or gravity waves are affecting the flow. The flow is irrotational, so there is no shear stress at the air–water interface or on the bottom. Furthermore, the linear nature of this formulation allows for the free surface to be represented by the superposition of sinusoids of different amplitudes and frequencies [103].

3.2.2 Governing Equations

The energy in the ocean wave does not travel at the same velocity as the wave profile due to wave dispersion. The velocity of a wave crest is typically called the wave celerity (*c*) whereas the velocity of the energy propagation is called the group velocity (C_g) [104]. In deep water, the group velocity is equal to half of the wave celerity but in general the relationship for the group celerity, employs the dispersion relationship [105]

$$C_g = \frac{c}{2}\left(1 + \frac{2kh}{\sinh(2kh)}\right) \tag{3.1}$$

Also, the wave celerity varies with water depth and is given by

$$c = \frac{L}{T} = \frac{g}{\omega}(\tanh kh) \tag{3.2}$$

Eq.(3.3) is called the dispersion relationship, and it defines the wavelength (*L*) based on the wave period (*T*), and water depth (*h*), where *ω* is the angular wave frequency and *k* is the wave number and *g* is gravitational acceleration = 9.81 m/s^2.

$$\omega^2 = k \times g \times \tanh(kh) \tag{3.3}$$

It is useful to classify waves according to the water depth in which they travel. This classification is summarised in Table 3.1 and has been made according to the magnitude of the ratio *h*/*L* [104].

Table 3.1. Wave classification

Classification	Deep–water	Transition water	Shallow water
h/L	>1/2	1/25 < h/L < 1/2	< 1/25
c	$\frac{g}{w}$	$\frac{g}{w}\tanh\left(kh\right)$	$\sqrt{gh}$
C_g	$\frac{L}{2\,T}=\frac{c}{2}$	$\frac{L}{2\,T}\left[1+\frac{2kh}{\sinh\left(2kh\right)}\right]$	$C_g = c$

In this work, LWT was applied in the initial stages of the device investigations. Therefore, we assumed that the flow is irrotational and inviscid. As a result of these assumptions, the velocity potential (ϕ) will satisfy the Laplace equation for two–dimensional flow:

$$\frac{\partial^2 \phi}{\partial x^2}+\frac{\partial^2 \phi}{\partial z^2}=0 \tag{3.4}$$

where $u = d\phi/dx$ is the horizontal particle velocity, $w = d\phi/dz$ is the vertical particle velocity, x and z are the horizontal and vertical coordinates, respectively as shown in Figure 3.1.

Applying the velocity potential of Eq.(3.4) in the Bernoulli equation yields:

$$\frac{\partial \phi}{\partial t}+0.5\left[\left(\frac{\partial \phi}{\partial x}\right)^2+\left(\frac{\partial \phi}{\partial y}\right)^2\right]+\frac{P}{\rho}+g\ z\ =0 \tag{3.5}$$

By combining the velocity potential in Eq.(3.4), Laplace's equation in Eq.(3.5) and considering aforementioned assumptions (i.e. Section 3.2.1) the small amplitude wave theory can be developed. Further discussion on boundary conditions and the solution of the linearised water wave boundary value problem can be found in Refs.[104, 105].

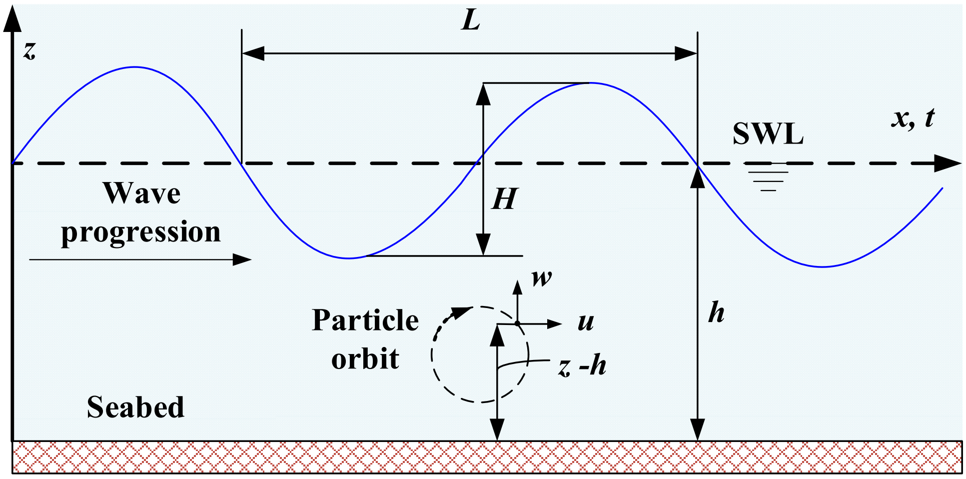

Figure 3.1. Definition of progressive surface wave parameters

The velocity potential of small amplitude linear waves

$$\phi = \frac{g\ H}{2\omega}\frac{\cosh k\left(h+z\right)}{\cosh kh}\sin\left(kx-\omega t\right) \tag{3.6}$$

The free surface profile is defined as

$$\eta\left(x,t\right)=\frac{1}{2}H\cos\left(kx-\omega t\right) \tag{3.7}$$

The horizontal (u) and vertical velocity (w) components of the fluid velocity can be derived from the free surface in Eq.(3.8) and the velocity potential in Eq.(3.9) as follows

$$u\left(x,z,t\right)=\frac{d\phi}{dx}=\frac{gHk}{2\omega}\frac{\cosh k\left(h+z\right)}{\cosh kh}\cos\left(kx-\omega t\right) \tag{3.8}$$

$$w\left(x,z,t\right)=\frac{d\phi}{dz}=\frac{gHk}{2\omega}\frac{\sinh k\left(h+z\right)}{\cosh kh}\sin\left(kx-\omega t\right) \tag{3.9}$$

The wavelength L can be defined as

$$L=\frac{gT^{2}}{2\pi}\tanh\frac{2\pi h}{L} \tag{3.10}$$

Pressure Field

The dynamic pressure field derived by substituting the velocity potential of Eq.(3.4) for the linearised form of Eq. (3.5) yields the following equation [103]

$$p_w = -\rho_w gz + \frac{\rho_w gH}{2}\left[\frac{\cosh k\left(h+z\right)}{\cosh kd}\right]\cos\left(kx-\omega t\right) \tag{3.11}$$

Wave Energy

The total energy (E_T) in a surface gravity wave is the sum of the kinetic and potential energies [106].

$$E_T = E_k + E_p = \int_{x}^{x+L}\int_{-h}^{\eta}\rho\frac{u^2+w^2}{2}dzdx + \int_{x}^{x+L}\rho g\left[\frac{\left(\eta+h\right)^2}{2}-\frac{h^2}{2}\right]dx \tag{3.12}$$

The kinetic energy (E_k) is associated with the water particle velocities while the potential energy (E_p) is due to the absolute elevation of the fluid mass above and below the still water level (SWL) [104].

After the integration Eq.(3.12), it can be seen that the kinetic and potential energies are equal and the total mean energy in a wave per unit crest width is given as

$$E_T = \frac{\rho gH^2}{8} \tag{3.13}$$

Wave Power

Sorensen et al. [104] defined wave power as “the wave energy per unit time transmitted in the direction of wave propagation”; it also is known as the wave energy flux. The product of the force acting on a vertical plane normal to the direction of wave propagation times the particle flow velocity across this plane is given as:

$$P_{in} = \frac{\rho g H^2 L}{16T}\left(1 + \frac{2kh}{\sinh 2kh}\right) \tag{3.14}$$

It could be simplified as

$$P_{in} = EC_g \tag{3.15}$$

3.3 Wave Modelling

As discussed in Section 3.1, as an ocean wave travels from deep to shallow water, its shape changes due to the increase of its height and decrease of its speed and length. Thus, the linear theory may fail to describe other phenomena that violate those assumptions that require higher–order wave theories [104]. There are many wave theories utilised in coastal and ocean engineering applications to model the wave at different water depths as presented in Figure 3.2[107]. The selection of the appropriate wave theory to be used for a particular application depends on two main factors: the relative water depth (h/gT^2) and the wave steepness parameters ($s = H/gT^2$). These are often used to distinguish between linear and non–linear waves [104]. From the Figure 3.2, if the values of H, T, and h are precisely known, it could be simple to select an appropriate wave theory. For instance, if the steepness $s < 0.001$ then the wave can be approximated by applying linear wave theory, but as the steepness increases ($s > 0.001$) then linear wave theory becomes less accurate and higher–order wave models such as the 5th order Stokes waves are more appropriate [105]. However, due to complexity in implementing high order Stokes theories in the WECs applications, linear wave theory is often used in the range of steepness larger than 0.01[82].

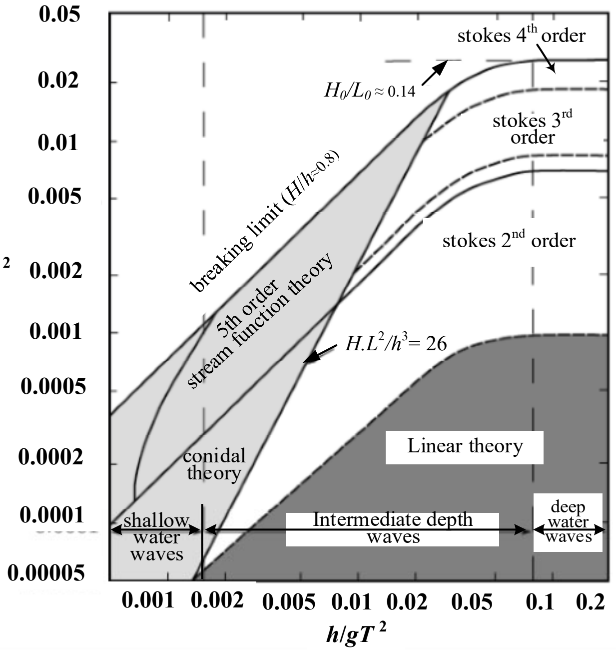

Figure 3.2. Wave model suitability, adapted from Ref. [107].

3.3.1 Regular Wave

Regular wave (monochromatic) conditions are usually employed during the fundamental stage of WECs development where wave motion, displacement, kinematics and dynamics can be determined for WECs design estimates. Thus, if we assume that wave energy converters operate in the range of sea states where linear wave theory is considered valid, the theory can be directly used as a mathematical representation of the ocean wave as a pure sinusoid as represented in Eq.(3.7).

3.3.2 Irregular Wave

Following the initial stage of the proposed model tests in regular wave conditions, it is logical to extend the test matrix to study device performance in irregular waves which are more close to realistic sea state conditions [108]. In reality, ocean waves are typically irregular and three–dimensional. These waves are unsteady in nature which means that their characteristics change in time, and it is very challenging to be exactly described in their full complexity. Therefore, a number of simplifying assumptions must be made to make the problems tractable, reliable and helpful through comparison to experiments and observations. In general, there are two common approaches that are utilized to model irregular waves. The first one is a superposition of a number of regular waves (wave components) with different frequencies,amplitudes and phases using Fourier theory as:

$$\eta(x,t)=\sum_{n}^{N}a_n\cos(\omega_n t-k_n x+\alpha_n) \tag{3.16}$$

where a_n is the wave amplitude, k_n and ω_n are related by the dispersion relation (Eq.(3.1)) and α_n is the phase.

The second approach is to describe a wave record at a specific point. These records are used to create a wave spectrum for real locations, giving the distribution of wave energy among different wave frequencies or wavelengths on the sea surface.

There are several classical spectral equations used to describe the frequency components of an irregular water surface elevation time history, such as the Pierson–Moskowitz [109], the JONSWAP spectra [110], the Bretschneider [111] and Ochi and Hubble spectrum [112]. In this work, JONSWAP spectrum was selected to express the energy content in the waves at different wave frequencies generated, based on measurements in shallow waters in the North Sea in 1968–1969 [103]. Its equation relating significant wave height (H_s) and peak period of measured spectrum (T_p) is given in Eq.(3.19) and it can be derived from the basic equation using

$$H_s=4\sqrt{m_0} \tag{3.17}$$

where m_0 is the zeroth moment of spectrum given by

$$m_0 = \alpha g^2 \omega^{-4} \left(0.06533\gamma^{0.8051} + 0.13467\right) \tag{3.18}$$

where *α* is a constant that relates to the wind speed and fetches length (*α*=0.23) and *γ* peak enhancement factor (*γ* =3.3).

The JONSWAP wave spectrum is formulated as in [103]:

$$S\left(\omega\right) = \frac{\alpha g^2}{\omega^5} exp\left(-1.25\left(\frac{\omega T_p}{2\pi}\right)^4\right)\gamma^{exp\left[-\frac{\left(\omega - \frac{2\pi}{T_p}\right)^2}{2\left(\frac{T_p}{2\pi}\right)^2\sigma^2}\right]} \tag{3.19}$$

where *S*(ω) is the spectral variance density.

The value of the spectral width parameter *σ* depends on the period (*1/f*)

$$\sigma = \begin{cases} 0.07 & f < f_p \\ 0.09 & f \geq f_p \end{cases} \tag{3.20}$$

For irregular wave conditions, the mean incident wave power (P_{in}) is calculated from Eq. (3.21) by the zeroth spectral moment of the incident energy density spectrum [113]

$$(P_{in})_{irrg} = \rho g \sum_{i}^{N} \left(C_g\right)_i S_i \Delta f \tag{3.21}$$

where *N* is number of frequency bands (each with a width of Δ*f*), and S_i and $(C_g)_i$ are (variance) spectral density and group velocity of the *i*th band, respectively.

3.4 Numerical Model Development

In the case of WECs technologies, numerical modelling enables the developers to: first, study from different geometries to numerous wave conditions avoiding the construction of different scale models; and second, carry out a wide number of physical tests at a lower cost than would be required for conventional laboratory tests. Therefore, numerical modelling can be a benchmark in the testing, designing and optimisation processes of the WECs technologies[22]. Most of WEC devices require several numerical models to represent device interactions with the surrounding environment [114]. The type of numerical model depends on where the device is to be deployed, the type of device being modelled, and the nature of the PTO system [22]. The fundamental theory of the hydrodynamic performance of the WEC device was first produced independently by Evans [115], Mei [116] and Budal [117]. This theory was then effectively simplified to linear wave theory (LWT) which was used over the next few years to develop numerical models of WEC devices in the frequency and time domain. It has been modelled using two approaches: the rigid piston model [81, 115, 118] and the uniform pressure distribution model [119]. These two models can be used for simple OWC device geometries such as a thin–walled vertical tube and two parallel vertical thin walls [114].

Recently, significant progress has been made in the development of the theoretical and numerical studies of the hydrodynamic performance of OWC devices [114]. These can be labelled with two categories; the first category is based on applying potential flow theory, which is usually solved with a boundary element method (BEM) [120]. It was applied by many research works like Brito–Melo et al. [121] and Le Crom et al. [122]. However, these methods cannot handle problems that require capturing detailed physics such as strong nonlinearity, complex viscous effects, turbulence and vortex shedding. The second main category is based on Reynolds–Averaged Navier–Stokes (RANS) equations, which provides more advantages in overcoming the potential flow weaknesses in handling problems that involve strong nonlinear dispersion and wave breaking [123].

Among the different approaches proposed for OWC modelling a simplified and less demanding model might be useful in the preliminary stages of device development. In this project, a simplified time–domain model implemented firstly to get a preliminary characterization of the range of the significant parameter values that are mostly affecting the OWC capture width ratio. Then a fully nonlinear incompressible 3D CFD model based on RANS–VOF was developed to perform an extensive investigation of the significant parameters that influence capture width ratio of the proposed device.

3.4.1 Time–domain model

Traditionally, the WECs can be modelled in the early stages of development by performing a frequency domain model under linear conditions [81]. However, the frequency domain has limited applicability, essentially restricted to linear problems. In this project, the PTO system used is a nonlinear PTO system as discussed in Section 3.4.3 3.4.3 In contrast to frequency domain modelling, time–domain models can produce a more accurate estimation of response and performance by the inclusion of nonlinear components [22].

In this work, two separate and isolated models were brought together in a time–domain to create an integrated mathematical model of the OWC device. The first model is the rigid piston model and second model is the thermodynamic model that was developed based on the ideal gas assumption to investigate the interaction between the differential pressure in the air chamber and the internal water surface motion inside the OWC device chamber.

3.4.1.1 Rigid Piston Model

Wave energy absorption is considered a hydrodynamic process; this process is complicated due to relatively complex diffraction and radiation wave phenomena. Modelling the motion of the internal water surface inside the OWC chamber is the key element to describe the hydrodynamic behaviour of the OWC device. The earlier studies indicated that the hydrodynamics of OWC devices could be modelled by replacing the internal free surface of the device with a weightless rigid piston moving only in heave [124-126]. Then Evans [115] and Ma [127] used the same approach to introduce a vertical velocity of the rigid plate which gave a more realistic representation of the interior of an OWC device. Recently, the rigid piston model was adopted by Gouaud et al. [128] to assess the efficiency of a fixed, bottom standing OWC device. Also, Falcão et al. [129] and Sykes et al.[130] utilised the rigid piston model in the hydrodynamic study aimed at the optimization of the OWC device. In the recent studies, Gervelas et al [131] employed a well–known approach conducted on trapped air cavities for marine vehicles developed by Harrisson et al [132] to model an OWC device in regular and irregular waves. Most of the previously mentioned studies have been developed using linear wave theory to represent the input waves. However, Gervelas et al.[131] combined the added mass phenomenon efficiently as a damping force on the system. Recently, in the case of OWC devices, a piston mode is normally an acceptable approach [22]. Thus, in this work, the behaviour of a heaving OWC device was compared to that of a mechanical oscillator, constituted of a mass–spring–damper system. The mathematical description of the rigid piston model will be addressed in Section 5.2.2 .

3.4.1.2 Thermodynamics Model

Most of the efforts in the field of OWC modelling focus on the system hydrodynamics. Therefore, there are relatively few researchers that have studied the thermodynamics of the air within the air chamber of an OWC and the effects of air compressibility [133]. The thermodynamic processes in the air chamber and the ducts connecting the air chamber with the air turbine may indeed significantly affect the OWC system dynamics. It usually modelled using mass conservation principles and based on the assumption of isentropic air compression/decompression in the OWC chamber. Fundamentally, the air volume above the water surface level inside the chamber is subject to the chamber differential pressure. Consequently, the air density also varies in time according to the pressure–density relation.

Sarmento et al.[134] proposed a first theoretical formula that represents the OWC chamber air compressibility under the assumption of a large volume of the air chamber (compared to air volume change) which is considered an isentropic process. This assumption was also adopted later by Josset and Clement [135] who present a time–domain numerical simulator for the OWC device, in which the problem has been divided into two sub–problems: an outer one, dealing with the incident, diffracted and radiated waves, and an inner one, concerning with the inner water volume behaviour which is linked with thermodynamics principles and a linear Power Take–Off (PTO) system. More refined thermodynamic models were developed and applied by Falcao & Justino [136] in which the viscous losses in the air turbine induce variation in the airflow entropy.

The theoretical analysis in this work was performed under the assumption of adiabatic processes in the OWC chamber as will be addressed in detail in Section 5.2.3

3.4.2 Computational Fluid Dynamics Modelling

Theoretical hydrodynamic modelling of OWC devices based on the linear water wave theory is still the most frequently adopted approach in the initial stage of WECs development. These models provide an acceptable level of accuracy and fast computational times required for design optimisation and performance analysis [22]. All of the MC–OWC devices addressed in Chapter 2 were modelled under linear water wave theory assumptions (except the turbines). Therefore, this approach cannot handle problems that require capturing detailed physics such as strong nonlinearity, complex viscous effects, turbulence and vortex shedding. Accordingly, the MC–OWC device could not progress to a TRL3 phase in the TRL approach [19]. In order to obtain a proper characterization of the aforementioned effects and drive the device development process to the advanced phase (i.e. TRL3), the TRL approach recommends using a nonlinear method based on Navier–Stokes equations that are implemented by employing Computational Fluid Dynamics (CFD) techniques [74].

In the last few decades, with increasing computational power, the CFD method became a valuable tool to study flow details of the wave–structure interaction and are the ideal complement to physical modelling [22]. This successfully provides an excellent numerical tool, enabling a cost–effective testbed for WECs experimentation, analysis and optimisation [113, 137-140]. A review of the different CFD modelling techniques for a wide range of WEC technologies is available in Ref.[141]. These models used commercial packages like ANSYS Fluent, CFX, FLOW–3D and Star–CD/CCM+ or free open–source packages like AMAZON, Code–Saturne, ComFLOW and OpenFoam.

Each of these packages has advantages and disadvantages, and some of them are easier to utilise than others. However, the packages' availability is playing an essential role in choosing appropriate packages for the modelling step.

Regarding the CFD modelling of OWCs, Luo et al. [142] applied a 2D numerical model using a commercial CFD code (Fluent) to identify the influence of wave nonlinearity on the hydrodynamic capture efficiency of fixed onshore OWC devices. López et al. [113, 143] applied 2D CFD (Stare–CCM+) model to study the effect of PTO damping on the performance of a bottom standing OWC device under regular and irregular waves. A similar study was performed in (REEF3D) by Kamath et al. [144] who developed a 2D CFD model to study the interactions of a fixed shore–based OWC with regular waves of different conditions under different values of linear PTO damping represented by a porous media. Vyzikas et al. [145] used 2D CFD (OpenFOAM) to model the hydrodynamic interaction between a fixed shore–based OWC device with regular and irregular waves. Recently, Elhanafi et al. [99] developed and validated a 2D CFD model based on RANS–VOF using a commercial CFD code (Stare–CCM+) to investigate the impact of increasing incident wave height and turbine–induced nonlinear damping on the energy conversion process in an onshore OWC. The research mentioned above was conducted on onshore and offshore OWC devices and was performed using 2D modelling. However, CFD modelling can be used to implement 2D or 3D numerical tests depending on the validity of 2D assumptions and the available computational resources and time. Elhanafi et al. [146] highlighted the impact of using 3D modelling/testing on estimating the hydrodynamic efficiency of an OWC. He proved that testing OWC devices in a 3D CFD model will be beneficial in avoiding overestimation of the device efficiency, especially at wave frequencies higher than the chamber resonant frequency. The device studied in this work, MC–OWC was designed to be aligned perpendicularly to the incident wave crests which means it allows the incident waves to pass not only underneath the OWC chamber but also around the device wall which increases the wave scattering. Therefore, using a 3D CFD model will expose this effect as reported in [146].

Realising the insight into the behaviour and hydrodynamic characteristics of a MC–OWC device that CFD modelling can provide, in this work a CFD model with a three–dimensional computational domain (numerical wave tank, NWT) will be employed using a commercial code STAR–CCM+ to simulate the hydrodynamics and aerodynamics of an MC–OWC device. This model solves the continuity and RANS (Reynolds Averaged Navier–Stokes) equations to describe the flow motion of the incompressible fluid. The model setting and validation procedure will be addressed in detail in Chapter 6.

3.4.3 Modelling the Power Take–off (PTO) System

The power take–off (PTO) system can be defined as the mechanism of transforming the absorbed power from the waves into useable electricity [82]. It is considered an essential part of the WECs due to its significant role in the capture efficiency of the wave energy converters. Thus, the WECs could be categorised based on the PTO system as we presented in Chapter 2 As shown in Figure 3.3, there exists a variety of PTO mechanisms which can be implemented with different technologies such as air turbines, power hydraulics, and electrical generators. Reviews of these systems have been presented by Pecher et al. [82].

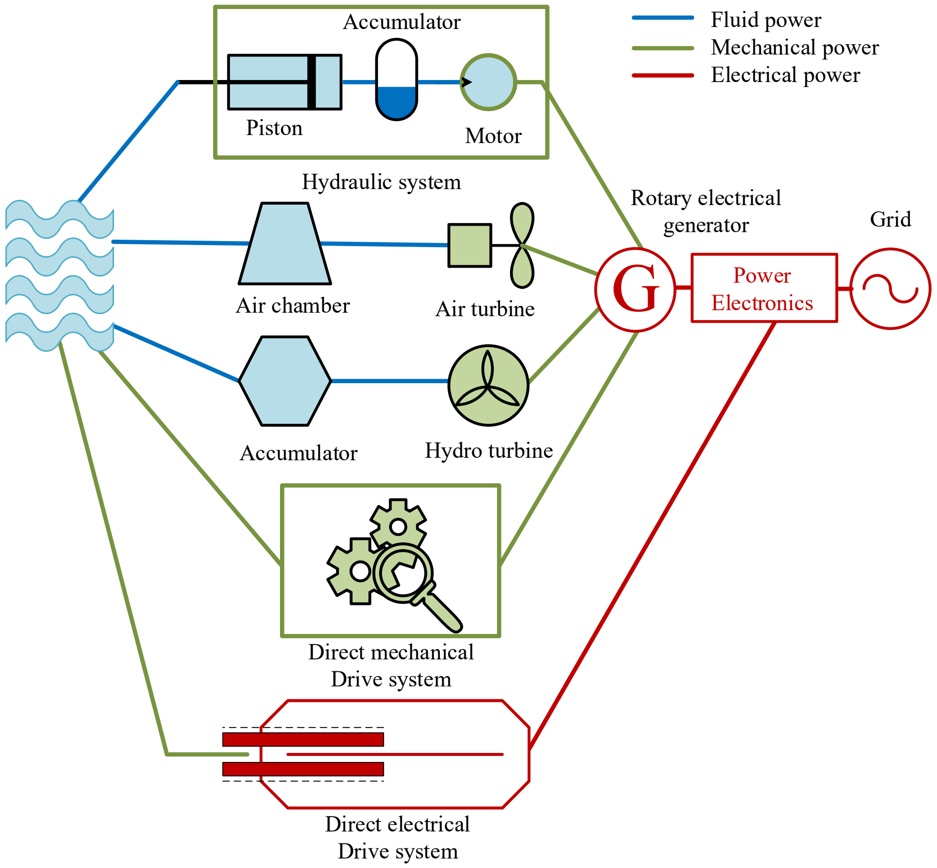

Figure 3.3. PTO mechanisms utilised for the wave energy conversion, adapted from [82].

At the initial stage of wave energy converter development, the numerical modelling studies have focused on the optimisation of the OWC devices geometry and the PTO characteristics based on the linear wave theory as discussed before in this chapter. In contrast, the physical test of the OWC devices is the most crucial path in different development stages, where there are many constraints like the scale of the wave tank, time, and funding [139].

3.4.3.1 Scaling of the PTO System of OWC Device

In physically designing test stages, not all components in the energy conversion chain, from wave–to–wire, of a WEC, can satisfy all similarity laws (geometric similarity, kinematic similarity, and dynamic similarity) [19, 147].

In the mechanical interactions between fluids and solids, three kinds of forces are of comparable importance: inertia, gravitational and viscosity forces. These forces can be quantified using two non–dimensional numbers: Froude number (the ratio of inertia force to gravity force, Eq.(3.22)) and Reynolds number (the ratio of inertial force to viscous force, Eq.(3.23))[148]. Most of WECs structure and some of PTO systems were tested based on the Froude similarity, Fr, which is based on the assumption $(Fr)_M = (Fr)_P$ (subscript M for model and P for prototype). In contrast, Reynolds similarity cannot be completely represented in small–scale model tests due to viscous effects which are generally negligible, though it is being considered in fully validated numerical models.

$$Fr = \sqrt{\frac{\text{inertia forces}}{\text{gravity forces}}} = \frac{u}{\sqrt{gl}} \tag{3.22}$$

$$Re = \sqrt{\frac{\text{inertia forces}}{\text{viscous forces}}} = \frac{\rho u l}{\mu} \tag{3.23}$$

where l, is the length scale, μ is the dynamic viscosity, and u is the fluid velocity.

The representation of the prototype to the model is reproduced in an undistorted manner. For similitude, the Froude number is given by,

$$\frac{u_p}{\sqrt{gl_p}} = \frac{u_m}{\sqrt{gl_m}} \tag{3.24}$$

Because the OWC device performance is highly dependent on the PTO system, the choice of PTO at the experimental scale is also critical to ensuring dynamic similarity. In OWC technologies, the Froude similarity is most often applied because the inertia force is the predominant force in the body–fluid interaction, although one of the important aspects of the OWC devices scaling is the air compressibility effect which cannot be completely represented in small–scale laboratory tests based on Froude similarity. Based on the small alteration in pressure and air volume inside the OWC chamber, most of the experimental and numerical work that is performed at small–scale is based on ignoring the air compressibility effect [149]. In contrast, the air compressibility effect may become important for the full–scale device when the air chamber volume and chamber pressure are large enough. Under such a circumstance, it is possible to measure the power extraction of the wave energy converter model in the wave flume conditions by using a simple PTO system.

In OWC devices, the incoming waves induce the internal water column to oscillate and force the trapped air to flow through the PTO system which consists of a self–rectifying axial–flow air turbine. In most OWC technologies, there usually are two different types of PTO systems, namely the linear Wells turbine and the nonlinear Impulse turbine [24]. It is placed in a channel connecting the air chamber with the outside atmosphere. In the experimental tests performed in the wave flume, the output power of Wells and Impulse turbines are known to be low due to the small amount of power being available (~10 W) for conversion [150], and it drops sharply due to aerodynamic losses produced by rotor blade stalling. However, small–scale OWC devices are not intended to convert the scale model mechanical power into usable electricity. Therefore, the developer of OWC devices proposed a simple PTO system that mimics the equivalent influence of the turbine on the wave motion to overcome the difficulties above [43, 149].

Generally, accepted practice is to simulate the PTO mechanism using an orifice (to simulate a nonlinear PTO representing an Impulse turbine) [97-99, 151, 152] or a porous material (to simulate a linear PTO representing a Wells turbine) [153, 154]. The power extracted by the orifice or a porous material is the so–called ‘pneumatic power’ in the literature which is defined as a relationship between the pressure change (Δp =

chamber pressure p_c minus the atmospheric pressure p_{atm}) and the airflow rate through the orifice (Q) [81]. Therefore, by changing the geometry of the orifices, the flow characteristics of the PTO can be altered.

In this work, the orifice plate was used to model the Impulse turbine due to its simplicity and its well representative relation between pressure drop and flowrate. The pressure drop across the Impulse turbine (Δp) can be approximated as proportional to the flowrate squared [90]. This relationship was quantified in this work for each orifice by means of the damping coefficient (τ), which has been shown to have a significant effect on the performance of OWC devices [113, 155]. This relationship is almost quadratic with a constant damping coefficient as shown by López, I. et al. (2014) and Simonetti et al. (2015) [113, 156].

$$\tau = \frac{\sqrt{\Delta p}}{Q} \tag{3.25}$$

For steady flow, the pressure change Δp (in Pascals) can be calculated mathematically by using time–domain model or by 3D CFD model. The airflow rate across the orifice Q (in m^3/s), was determined by using the standard orifice theory given by

$$Q = C_d A_2 \sqrt{\frac{2|\Delta p|}{\rho_{air}}} \tag{3.26}$$

3.5 Modelling of the Device Performance

In the development stages of WECs, one of the important aspects is to assess the device performance (i.e. efficiency). Generally, in the engineering applications, the efficiency concept is defined as the ratio of output power to input power [43].

In WECs systems, the efficiency could be obtained as the product of the efficiencies of three energy transformation processes: the transformation from wave energy to pneumatic energy, transformation of pneumatic energy into mechanical energy and conversion of mechanical energy into electrical energy.

The three–dimensional effects permit the WECs to absorb power from the total wavefront incident upon the device and are not restricted to a wavefront possessing the same width as the device, therefore, the device relative capture width may reach a value of greater than one, which is not true for efficiency concepts. To overcome this problem, many concepts and terminology are introduced in the investigation studies of the WECs. A common concept employed to evaluate the WECs performance is the capture width, capture width ratio and non–dimensional absorption length [157]. In this work, a capture width ratio (ε) is utilised to define the theoretical and experimental power conversion capacity of the MC–OWC device. It is defined as the ratio between the mean power extracted by the device and the mean power per unit crest wave width

$$\varepsilon = \frac{\bar{P}_n}{b \times P_{in}} \tag{3.27}$$

of the incident wave train across the width of the device (b).

where P_{in}, is defined in Eq. (3.14) and, in this work, the first process of energy transformation is considered (i.e. from wave energy to pneumatic energy). Therefore, for incompressible air, the pneumatic power (P_n) that an OWC device can extract is expressed as in Eq. (3.28) [153].

$$P_n = \frac{1}{T}\int_0^T Q\left(t\right).\Delta p.dt \tag{3.28}$$

3.6 Resonance

Enhancing the performance of OWC devices is one of the significant features for marketing the technologies, and hence it has been the subject of extensive study by many researchers [46]. A wide range of studies and modifications was conducted to improve the efficiency of OWC devices, like adding new control devices to the standard OWC device, which is applicable for phase control in each individual wave [158]. One of the most effective approaches to improve device performance is to enable the OWC device to work under the resonance conditions, which will provide further possibilities to design and improve the performance of the devices in various sea states.

Theoretically, there are two distinct possible resonance phenomena that can occur in the conventional fixed type OWC devices: piston or sloshing [159]. The first resonance mechanism occurs due to the adaption of the frequency of the incoming waves and the natural frequency of the water column inside the chamber of the OWC device. The sloshing resonance mechanism occurs when the incident wave frequency is such that the fluid inside the chamber is excited into an anti–symmetric sloshing mode [160].

In this project, the time domain model presented in Chapter 5 is particularly useful for investigating the first resonance phenomena. For the case with no damping and assuming a sinusoidal displacement of the internal water surface, the undamped natural frequency can be calculated from time–domain model. The displacement η, is taken to vary with angular frequency ω and magnitude $\tilde{\eta}$, as $\tilde{\eta}e^{i\omega t}$. If B and $f(t)$ in Eq.(5.1) is assumed zero, and the added mass was neglected then the undamped natural frequency for the oscillator can be represented as

$$\omega_n = \sqrt{\frac{g}{d}} \tag{3.29}$$

It clearly appears from the Eq.(3.29), the only design parameter that is important is *d*, the draught of the OWC. However, the added mass may influence the predictions of the resonance conditions significantly. In this regards, Veer and Thorlen [159] introduced an approximate formula to estimate the device natural frequency by considering the influence of the added mass as follows, and neglecting the pneumatic damping induced by the PTO system:

$$\omega_n = \sqrt{\frac{g}{d + 0.41\sqrt{A_1}}} \tag{3.30}$$

The factor 0.41 in the above equation is obtained experimentally and hence does not necessarily provide accurate results in the case of the OWC device [155]. The dependence of the natural frequency on the draught and the chamber area can be clearly seen in Eq. (3.30).

3.7 Summary

This chapter provides an overview of the relevant theories and numerical modelling techniques utilised throughout this thesis. The emphasis in this chapter was on the two numerical models which are the time–domain model and the 3D CFD model. Further details of these models will be introduced in Chapter 5 and 6 respectively.

Chapter 4 : PHYSICAL MODEL EXPERIMENTS

4.1 Introduction

Both experimental wave tank testing (which is the objective of this chapter) and numerical modelling (which will be discussed in Chapters 5 and 6) are the most common and powerful approaches utilised during the design and development of a wave energy converter, [114]. However, simplified mathematical models that can describe the WEC are still beneficial for their inexpensive computational time and resources while providing an initial insight into device performance.

In general, physical scale model experiments of WECs are usually performed for different objectives, which mainly include: 1) concept verification, 2) validation of mathematical and numerical models, 3) quantification of the technical performance parameters that could influence the device performance and survivability and 4) provision of data for optimized performance design [147, 161]. Therefore, model experiments in wave tanks under idealised and controlled environmental conditions are a crucial step in the development of wave energy converters. It is, however, important to mention that physical model experiments are costly and might require several trials prior to completion of the final design [147, 161]. Therefore, model experiments in wave tanks under idealised and controlled environmental conditions are a crucial step in the development of wave energy converters.

This chapter describes the key aspects in the development stages of the MC–OWC physical model and experiments, which can be considered as the milestone experimental studies of MC–OWCs device for the current project and upcoming investigations.

4.2 Experimental Testing

There were two series of experimental tests performed to provide a better understanding of the hydrodynamic performance of two small–scale MC–OWC devices in two different wave flumes. The first experimental campaign was conducted in a small wave flume in the University of Technology Sydney (UTS) with a primary objective of initially validating MC–OWC mathematical and numerical models and observing the device response when subjected to regular wave conditions. On the other hand, the second experimental session was carried out in the wave flume at the Manly Hydraulic Laboratory (MHL) in New South Wales, Australia. The wavemaker of this flume is more capable of generating a wide range of regular and irregular wave conditions compared to the wavemaker at UTS wave flume. This session was performed with a main focus centred on investigating the influence of different design parameters such as power take–off (PTO) damping and device draught under a variety of wave conditions.

4.3 First Experimental Test (UTS Wave Flume)

4.3.1 Model Geometry

The MC–OWC model used in this experiment and shown in Figure 4.1 was initially designed and manufactured by Professor David Dorrell as an extension of the models developed by Dorrell et al. [72] and Hsieh et al. [41] to be used for teaching purposes at University of Technology Sydney to assist demonstrating the principle of the wave energy generation. The geometry of the model used in this test is relatively simple with a rectangular cross–section with the interior dimensions of each chamber being 365 mm in length, 150 mm in breadth, and 256 mm in height as illustrated in Figure 4.2. The model was attached to a fixture of two supports mounted to the top of the wave flume side walls as shown in Figure 4.1. This model was made of 10 mm thick Perspex sheets to enable viewing of internal water movement during the test. The cover of each chamber included a hole to simulate the PTO system which was used to mimic an impulse turbine as presented in Section 3.4.3 . The device was perpendicularly aligned to the incident wave crests so that it allows the incident waves to pass not only underneath the OWC chamber but also around the model side walls. A thin triangular sheet of metal was attached to both the front and the rear walls of the terminal chambers to disperse the incident wave around the device and reduce wave reflection effects.

Figure 4.1. A photo of the MC–OWC model tested in the UTS wave flume.

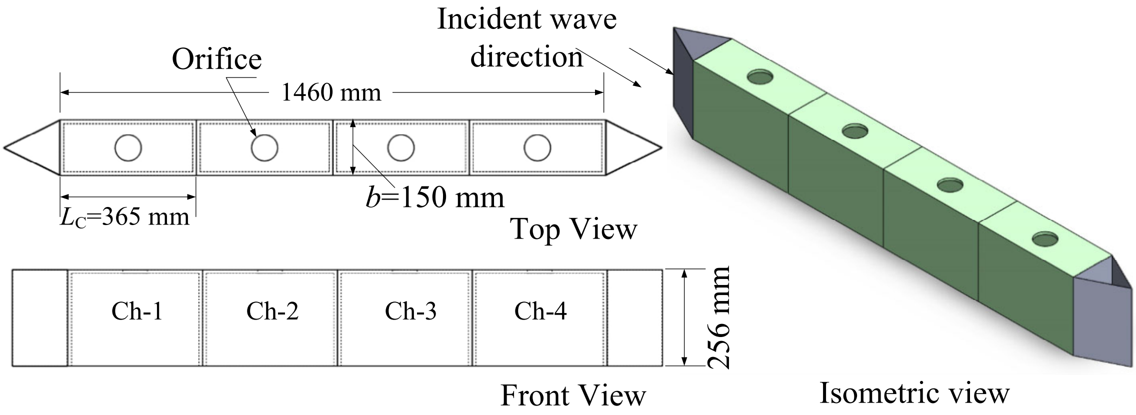

Figure 4.2. MC–OWC model geometry tested in UTS wave flume

4.3.2 Overview of UTS Wave Flume

This section describes the UTS wave flume, experiment setup and test procedure. The wave flume shown in Figure 4.3 has a length of approximately 4.3 m, a width of 0.9 m and a depth of 1.0 m. The flume is equipped with a hydraulic hinged flap paddle that is installed on the left side of the flume. The wavemaker has the ability to generate regular waves with a maximum wave height of 0.1 m at a maximum water depth of 0.5 m for a limited number of wave periods. The water depth in the wave tank is kept constant during the test by the water circulation system (see the front view in Figure 4.4). This system works to reduce the wave reflection alongside the inclined over–topping beach (sloped at 1:4) which is covered with an absorbent layer of foam at the end of the wave tank. The reflection coefficient was found to be less than 2% in the range of wavelengths tested, which met the standard characteristic of the absorbing beach mentioned in [43]. The waves generated by the paddle travel about twice the length of the paddle depth (*h* = 0.5 m) before settling, thus the waves become fully developed in the test section which is located at 1.3 m away from the paddle and has a glass–wall as shown in Figure 4.4. The flume sidewall effect was neglected considering that the ratio of the flume width (0.9 m) to the physical model width (*b*) was 6 which is larger than 5 as defined in Ref. [162]. The wave tank system was equipped with a data acquisition system (I/O) to control the wavemaker and collect the raw data from the sensors as shown in the front view in Figure 4.4. The sampling rate of the data acquisition system was 10 Hz. In order to avoid the re–reflection of waves from the wavemaker, the data were collected for a period of time equal to 20 s.

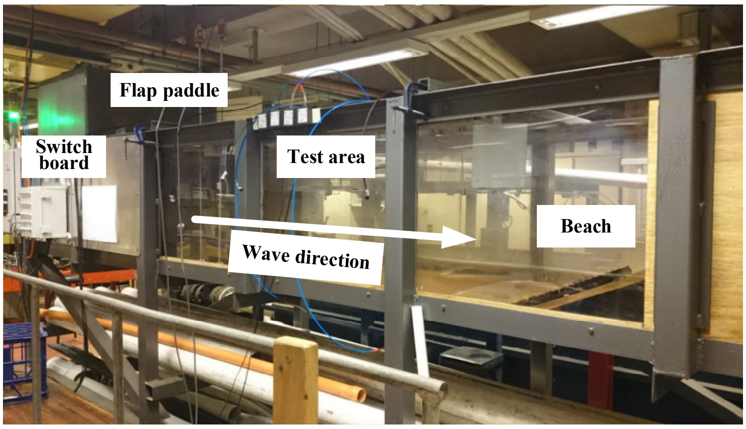

Figure 4.3. A photo of UTS wave flume

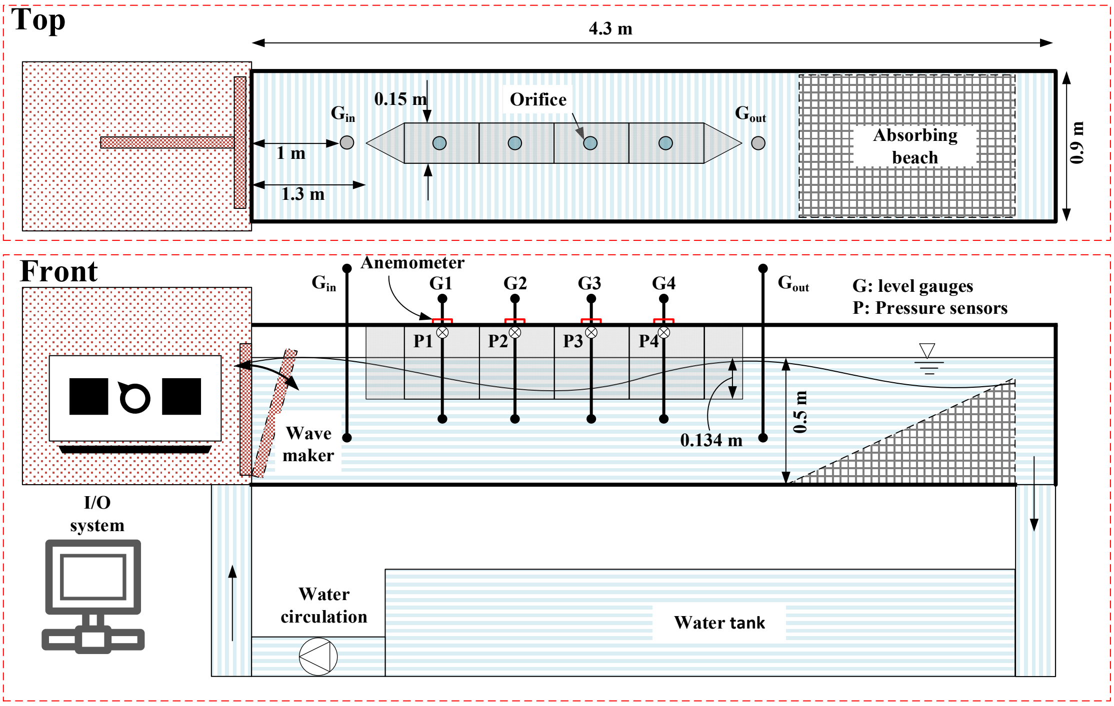

Figure 4.4. The layout of the experiment conducted in UTS wave flume

4.3.3 Test Conditions

The wave conditions considered for this experiment were selected based on the data available at one of the potential deployment sites in New South Wales, Australia. These sites have more than 54 berths ranging in length from 8 to 40 m with a water depth which varies between 6 and 12.5 m, and they have an average wave power of about 20 kW/m which is within the acceptable range of a good average wave power content (>15 kW/m) [82]. The physical model was scaled based on Froude's similitude law (Eq. (3.24)). The scale factor (λ) in this experiment was 1:25 such that the 0.5 m water depth in the wave flume represented 12.5 m at full scale and the model length of 1.46 m represented 36.5 m length at full scale. The target wave height (H) was set at 0.087 m and three different wave periods (T) of 1.12, 1.20 and 1.25 s were tested.

4.4 Instrumentation and Measurement

4.4.1 Wave Height Measurement

Because of the ratio of the chamber length (L_c) to the shortest wavelength (L) tested in this experiment was 0.24, which was quite enough to avoid sloshing modes (L_c/ L) [97], the free surface was assumed to be uniform. Therefore, the water elevation oscillation (η) inside each chamber was measured using one wave gauge. Therefore, four–wave gauges (G1–G4, model: C–Series Core Sensor, CS), one in each chamber as shown in Figure 4.4, were used to measure the water free surface oscillation (η) at the centre of the chamber ($L_c/2$, $b/2$). Each wave gauge comprised of a magnetic float level transmitter of 5 mm in diameter with a stroke length of 250 mm. The induced voltages were digitized at 1500 Hz (0.6 ms period), and the free surface displacement (η) was calculated based on the relationship $\eta = \delta \times V(t)$ where the coefficient δ was obtained through a static calibration of each wave gauge.

Two wave gauges (G_{in}, G_{out}, model: G–Series) were placed at the distance of 0.3 m from the front and back faces of the device to measure the incoming and transmitted wave heights. All the wave gauges were calibrated manually at the beginning of each test as per the manufacturer's instructions.

4.4.2 Pressure Measurement

The differential air pressure fluctuation inside the OWC chamber (i.e., the difference between the air pressure inside the chamber, p_c, and the atmospheric pressure, p_{atm}) is the most significant parameter in the estimation of OWC device performance. It is frequently measured at a single point [160, 163]. Therefore, differential pressure transmitters (P1–P4, model: 616–20B, accuracy ± 0.25% full–scale (F.S) with a range of ±10 inch water column (in.w.c) were utilised to measure the differential air pressure (Δp) in each chamber as shown in Figure 4.5. All pressure transmitters were calibrated, by Fluke 717 Series Pressure Calibrators, before the test session and were installed at a distance of 10 mm from the upper edge of the rectangular section of each chamber as shown in Figure 4.4.

Figure 4.5. Pressure transmitters (model: 616–20B, ±0.25% F.S)

4.4.3 Airflow Measurement

The vertical air velocity component (V_a) through the orifice was measured at the centre of the orifice of each chamber by a Hot–film Anemometer with Real–Time Data Logger (HHF–SD1). This anemometer has the capability of measuring bi–directional flow rates and measuring air velocities down to 0.05 m/s. Also, its relatively fast frequency response of 0.01s allows sampling the oscillations of the air velocities at a suitable rate. The airflow rate (Q) was then calculated from ($Q = V_a \times A_2$, where A_2 is the orifice cross–sectional area).

4.4.4 Calibration of the Orifice Plates

As discussed earlier in Section 3.4.3 , the PTO system in this research was represented by an orifice to simulate an impulse turbine. The orifice plate was circular, classified as a thin–walled opening orifice (the ratio between the orifice thickness and orifice diameter was less than 0.5 [164, 165]) and was manufactured using a laser cut machine..

The diameter of the orifices used in this experiment was in range of $0.1 < \beta < 0.75$ (where $\beta = D_{\text{orifice}}/D_{\text{pipe}}$) as recommended by International Organization for Standardization (ISO 5167–2) [166]. Each orifice plate was experimentally calibrated using Testo 480 IAQ Measurement Kit to determine its Coefficient of Discharge (C_d) according to ISO 5167–2 standardisation. The apparatus used in this calibration is illustrated in Figure 4.6, which contains two pressure taps that are normally located at a distance of D_{pipe} and $0.5D_{\text{pipe}}$ (D_{pipe} is the internal diameter of the pipe = 150 mm) upstream and downstream of the orifice, respectively [166]. These two taps are connected to Dwyer 477AV–0 Handheld Digital Manometer to measure the differential pressure (p_2–p_1). The apparatus also includes a butterfly valve that can be used to adjust the airflow rate (Q).

The atmospheric pressure and temperature during the calibration were measured to be 940 mbar and 22 °C, respectively. The dry air density, ρ_{air}, at this temperature was taken as 1.2 kg/m^3. The calibration was conducted by changing the airflow rate, and a series of pressure drops across the orifice plate was measured. Under known pressure and airflow rate results, the standard orifice theory (Eq. (3.26)) was applied to determine the C_d. The mean coefficient of discharge was estimated to be $C_d = 0.597$.

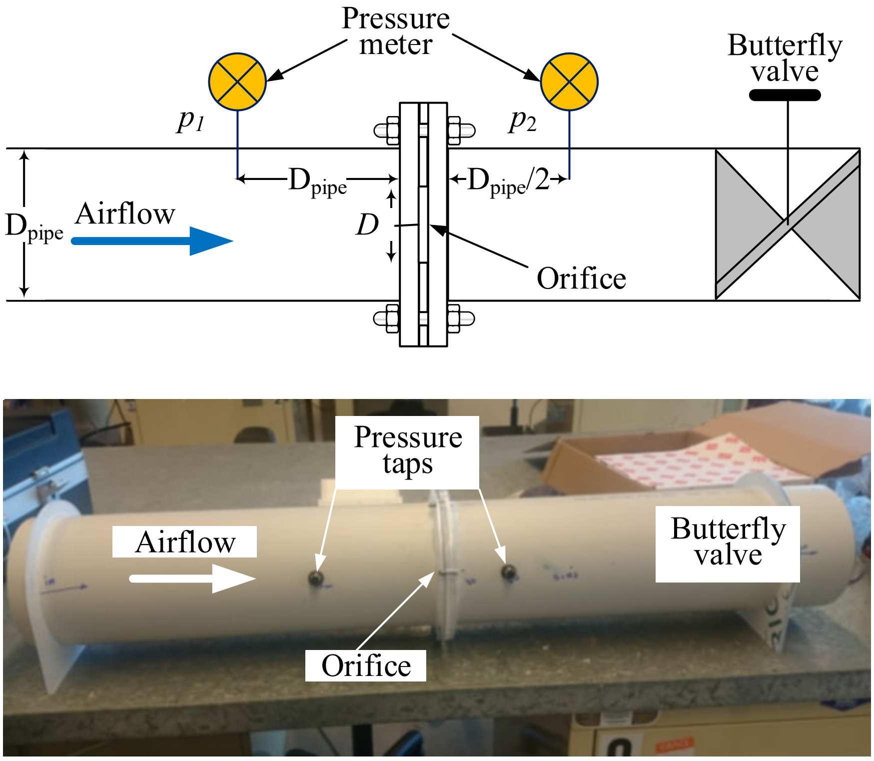

Figure 4.6. Orifice calibration test rig

4.5 Data Analysis of the UTS Wave Flume

The raw data from the wave gauges and pressure transmitters during each individual run were captured by a data acquisition computer and then converted into actual measurements using the calibration coefficients. The chart in Figure 4.7 describes the procedure used for experimental data collection and processing.

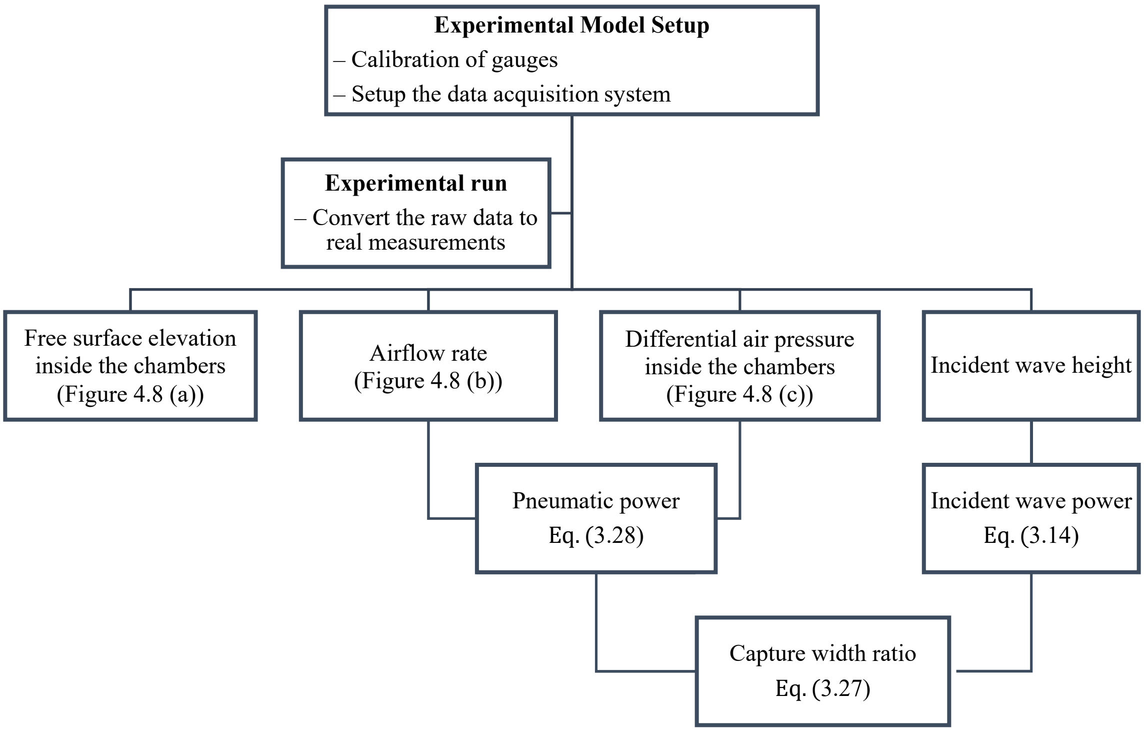

Figure 4.7. Experimental data collection and processing flow chart

Figure 4.8 shows an example of the experimental data measured in each chamber for free surface elevation (η), airflow rate (Q) and differential air pressure (Δp). It is important to note that in this figure, the experimental values of Δp were not measured using the pressure transmitters due to large uncertainties coming from the difference between the sampling frequency of the sensors and the sampling rate of the data acquisition system which was solved later in the second test; instead, Δp was calculated using the orifice pre–calibration approach as discussed in Section 4.4.4 . In this experimental session, the device was tested in limited regular wave conditions for the main purpose of numerical models validation, which will be discussed in Chapter 5 and 6.

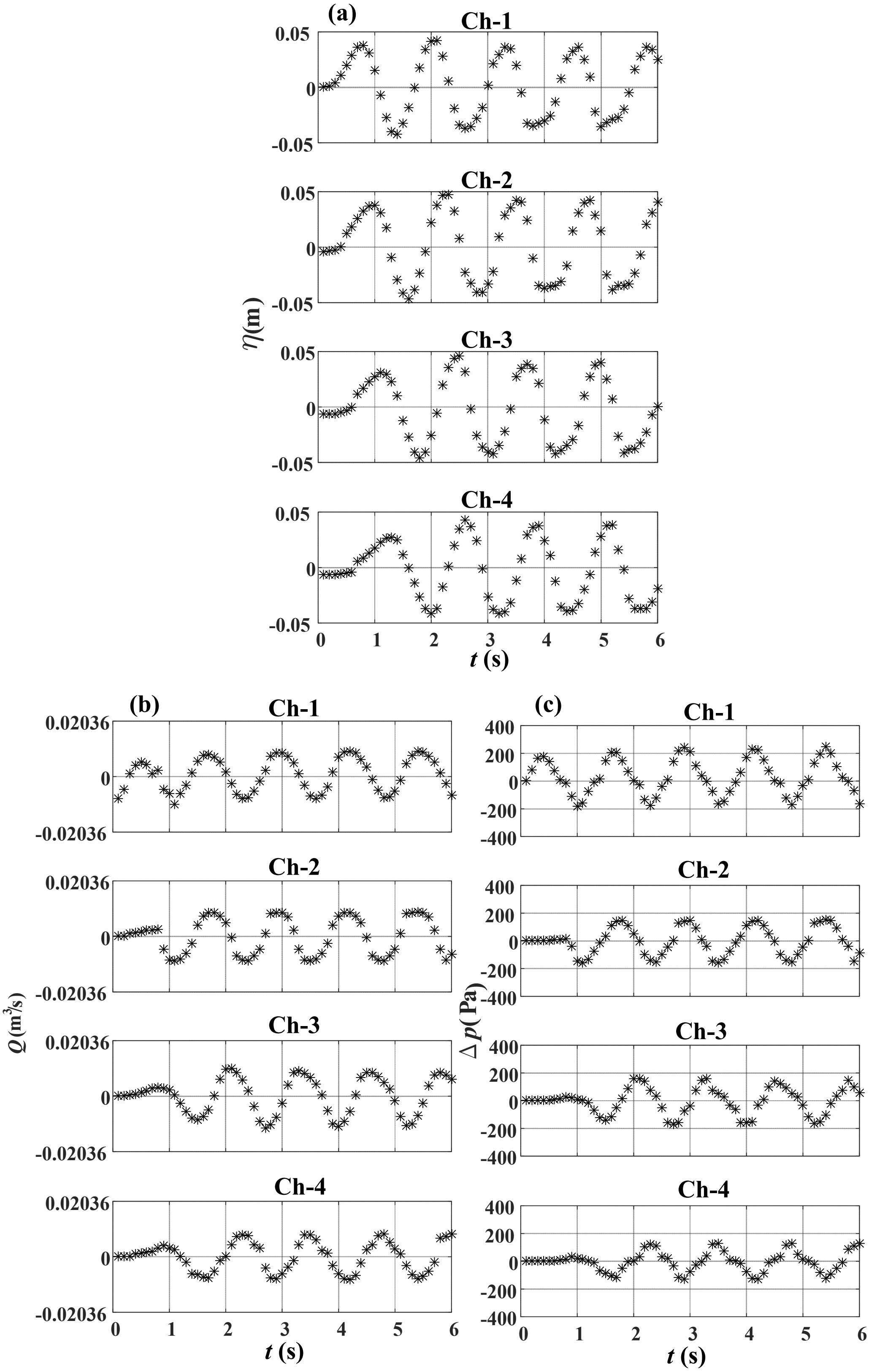

Figure 4.8. Sample time–series data of (a): free surface elevation (η), (b): the airflow rate (Q), (c): differential air pressure (Δp) in each chamber for a wave condition of H = 0.087 m and T = 1.0 s.

4.6 Second Experimental Testing (MHL)

Due to the limitations experienced with the wavemaker of the UTS wave flume during the first test session, and the renovation work in the UTS laboratories, the second experimental session of this research project was resumed in the wave flume at Manly Hydraulics Laboratory (MHL) that provides specialist services in the area of water, coastal and environmental solutions.

The second test session was carried out with the following objectives:

[1] Assess the device performance over a wide range of regular and irregular wave conditions.

[2] Investigate the effect of the pneumatic damping induced by the power take–off (PTO) system on device performance.

[3] Study the impact of wave height, wave period and device draught on the performance of a MC–OWC device.

4.6.1 Overview of Manly Hydraulics Laboratory Wave Flume

The wave flume in MHL, shown in Figure 4.9, has a length of 30 m, a width of 1 m and a depth of 1.8 m. The test section in the flume is about 7 m long and starts 15 m away from the wavemaker. The flume is equipped with a flap paddle wavemaker driven by an electrical actuator that is located at the left–side end of the flume. The specifications of the wavemaker allow it to generate regular and irregular waves with a maximum regular wave height of 0.35 m at a maximum water depth of 1.3 m over a range of wave period of 0.75–3.0 s. At the right–side end of the flume, there is an absorption beach consisting of multiple sponge layers and hollow bricks to minimise the waves reflecting back towards the test section.

Figure 4.9. A photo of MHL wave flume

4.6.2 MC–OWC Model Geometry

The physical model used in this experiment was similar to the model previously tested in UTS wave flume, except for a few modifications that were performed to increase the accuracy of the measured data. First, the dimensions of the model were doubled as shown in the 3D CAD drawing in Figure 4.10. A second modification was made in the air duct to avoid the disturbance in the water surface during the inhalation stage. According to Falcão et al. [149], a typical design value of the air chamber volume divided by the area of the OWC free surface ranges between 3 and 8 m, and any increase in this ratio is not necessarily detrimental to the efficiency of the energy conversion. This ratio was 3.7 m in the model used in this experiment.

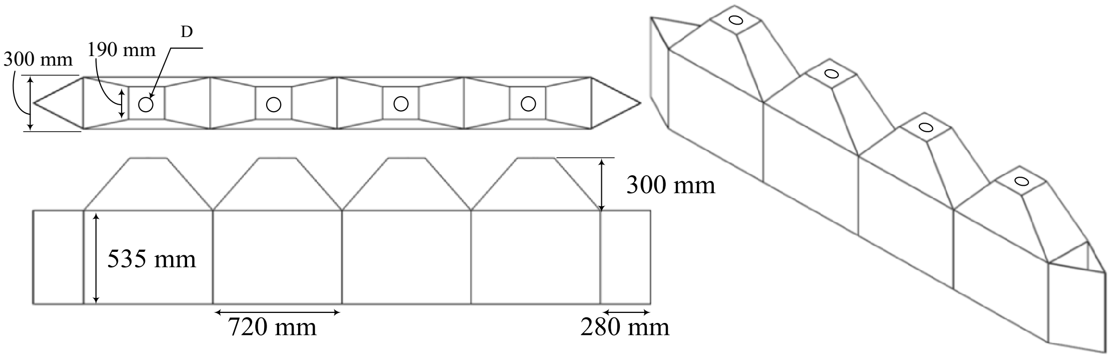

Figure 4.10. Geometry and dimensions of the MC–OWC model tested in MHL wave flume

The model was scaled based on Froude's similitude law, Eq. (3.24), with a scale factor (λ) of 1:16, which made the 0.8 m water depth in the wave flume represented 12.8 m at full scale and the model length of 3 m represented 48 m at full scale.

The MC–OWC model was constructed of 10 mm Perspex sheets and glued together. The dimensions of the Perspex chambers are shown in Figure 4.11. To disperse the incoming waves around the device and reduce the wave reflection, two triangle galvanized–steel sheets were attached to the first chamber (Ch–1) and the last chamber (Ch–4) as shown in Figure 4.11 (a). This figure also shows that the model was mounted on the flume side walls by three horizontal rectangular sections, which were locked to the flume side walls using clamps (see Figure 4.11 (b)). Each of these sections had two threaded rods to straighten the device and adjust the draught of the device to the desired value as shown in Figure 4.11 (c). Three draughts of 200 mm, 250 mm, and 300 mm were examined in this test. The power take–off system was simulated using a circular orifice situated on the roof of each chamber as illustrated in Figure 4.11 (d).

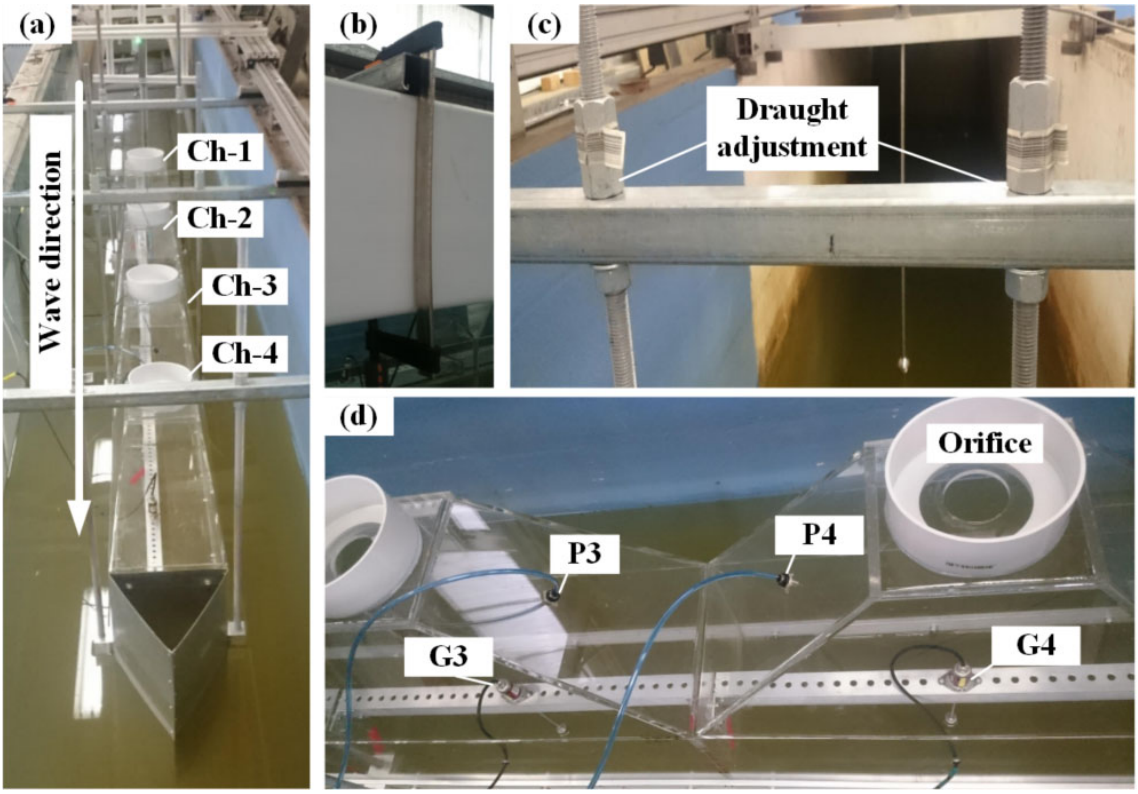

Figure 4.11. Photo of MC–OWC model tested in MHL wave flume

4.6.3 Experimental Setup

A schematic diagram of the experiment setup and the position of data collection gauges is presented in Figure 4.12. The MC–OWC device was placed at a distance of 15 m from the wavemaker, which was more than two wavelengths to ensure that fully developed waves are incident on the model chambers for the range of wave frequency tested.

In this experiment, the same wave gauges and pressure transmitters used in the first experimental session were utilised. Additionally, all the approximations and assumptions made for the previous test were maintained in this test (i.e. data collections and calibration procedure). The water free surface oscillation inside the chamber was measured at the center of each chamber ($L_c/2$, $b/2$) using wave gauges G1–G4, while four differential air pressure transmitters P1–P4 were used to measure the dynamic differential air pressure in the chamber (Δp). By applying a standard orifice theory Eq. (3.26) the airflow rate Q through the orifice was calculated where the mean coefficient of discharge $C_d = 0.597$ was used. In order to determine the incident wave power P_{in} for both regular and irregular waves, the data measured by the wave gauges G_{in} and G_{out} were used to estimate the energy of the incoming waves.

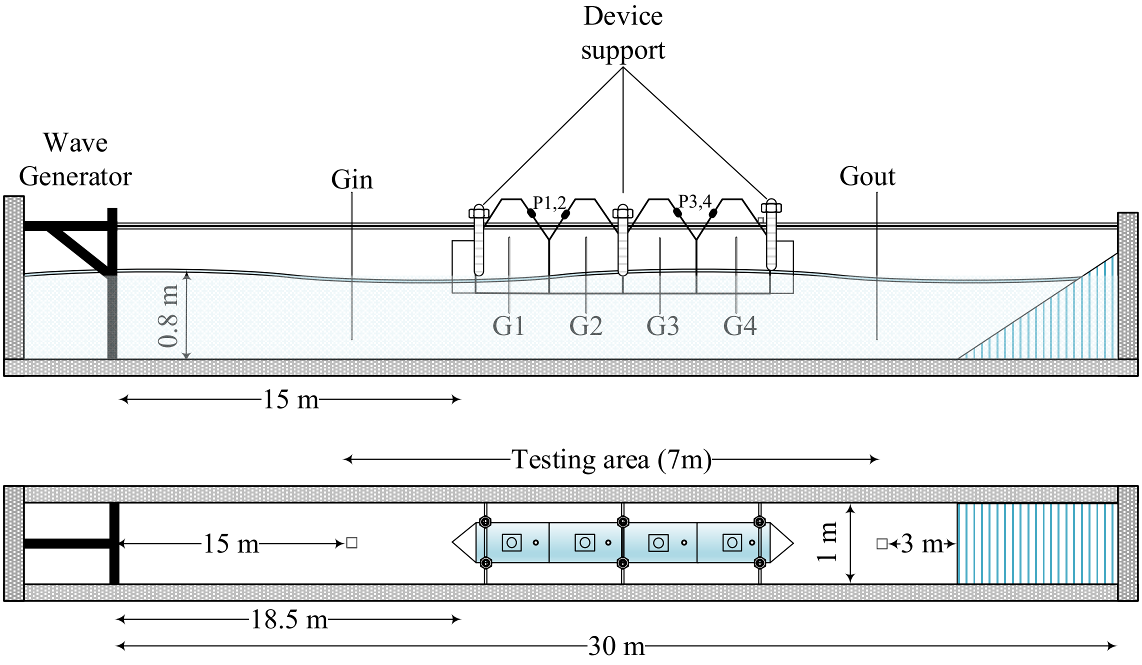

Figure 4.12. Experimental setup of the MC–OWC model in MHL wave flume

4.6.4 Regular Wave Tests

In this section, a total of 198 tests were performed under regular wave conditions to investigate the effect of incoming wave period, wave height, device draught and PTO damping on the hydrodynamic performance of the MC–OWC model. The experiments systematically investigated the following variables: two regular wave heights H = 50 and 100 mm, eleven wave periods T = 1.0 –2.0 s in steps of 0.1 s, three orifice diameters and three draught values as summarised in Table 4.1. The water depth was fixed at h = 0.8 m. Within the range of wave conditions tested, the wave steepness varied between

0.010 and 0.032. The time–series measurements from all gauges were collected for 50 seconds.

Table 4.1. Experimental test conditions and parameters

Orifice diameter D (mm)	Draught d (mm)	Wave height H (mm)	Wave period T (s)
30	200	50	1.0,1.1, 1.2, 1.3, 1.4, 1.5, 1.6, 1.7, 1.8, 1.9, 2.0
		100	
	250	50	
		100	
	300	50	
		100	
60	200	50	
		100	
	250	50	
		100	
	300	50	
		100	
80	200	50	
		100	
	250	50	
		100	
	300	50	
		100	

The main objective of this experimental campaign was to investigate the influence of the wave period, incident wave height, device draught and PTO damping on the parameters that control the MC–OWC device performance such as chamber water surface elevation η, airflow rate Q, differential air pressure Δp, and pneumatic power P_n. An example of the time–series measurement of these parameters is shown in Figure 4.13. In the context of the analysis, the time–averaged extracted pneumatic power ($\overline{P}_n$) and the hydrodynamic efficiency (or capture width ratio, ε) were calculated from Eqs. (3.28) and (3.27), respectively. The airflow rate through the PTO was calculated using

Eq. (3.26). The three different orifice plates used in this test to introduce different damping factors were characterized by the orifice opening ratio (R_i), which is defined as the opening area of the orifice (A_2) divided by the cross–sectional area of OWC chamber (A_1) as summarised in Table 4.2.

Table 4.2. Orifice diameter and its opening ratio

D (mm)	30	60	80
R_i (%)	0.34	1.35	2.40

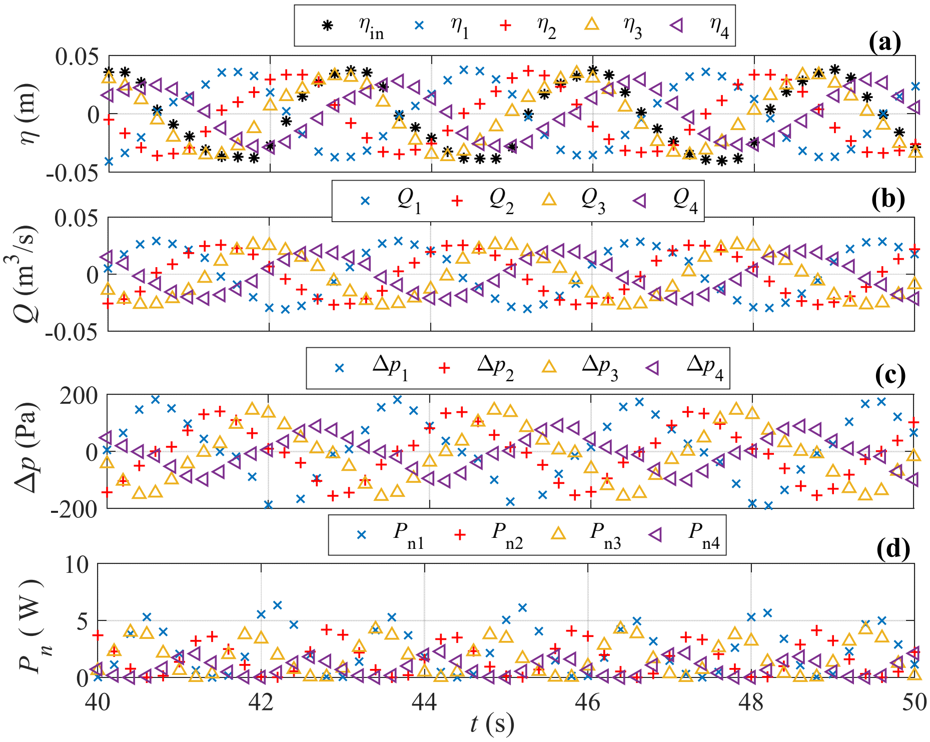

Figure 4.13. Sample of time–series data of (a): water surface elevation η, (b): airflow rate through the orifice Q, (c): differential air pressure Δp, (d): pneumatic power P_n in each chamber for a wave condition of H =100 mm, T =1.5 s, a draught d = 250 mm and an orifice of D = 60 mm

4.6.4.1 Effect of Wave Period and Height

This section investigates the effect of incident wave period and height on device performance parameters and capture width ratio. Therefore, the results of two different wave heights H = 50 and 100 mm over a range of wave periods T = 1.0–2.0 s (see Table

4.1) were considered under a constant orifice opening ratio R_2 = 1.35 % and a draught d = 250 mm. Figure 4.14 demonstrates the effect that the wave period and height have on the water surface elevation (η), the airflow rate (Q), the differential air pressure (Δp) and the pneumatic power ($\overline{P}_n$). Overall, it can be seen that among the four chambers, the highest performance was observed in the first chamber, while the performance gradually decreased up to the fourth chamber where the lowest performance was found. This could be assigned to the energy absorbed by each chamber and the energy lost in each chamber, which reduced the available energy to be absorbed by the fourth chamber [137, 167].

For each chamber, it is known that changing the wave period has a significant effect on device interaction with incoming waves such that it affects different energy components such as reflected energy, transmitted energy and energy losses [99], which in turn impact device performance. This effect is shown in Figure 4.15 for the time–series results of the performance parameters at a constant wave height H = 50 mm, an orifice opening ratio R_2 = 1.35 % and a draught d = 250 mm.

Results in Figure 4.14 illustrate that each performance parameter has a similar trend for both wave heights, but increasing the wave height increased the absolute values of each parameter tested, which is attributed to the increase in the energy content in the larger wave height. An example of this effect is summarised in Table 4.3 as the ratio between the average results over the whole period range tested (1.0–2.0 s) for H = 100 mm and H = 50 mm. These results also show that the four chambers have a similar response to increasing the wave height.

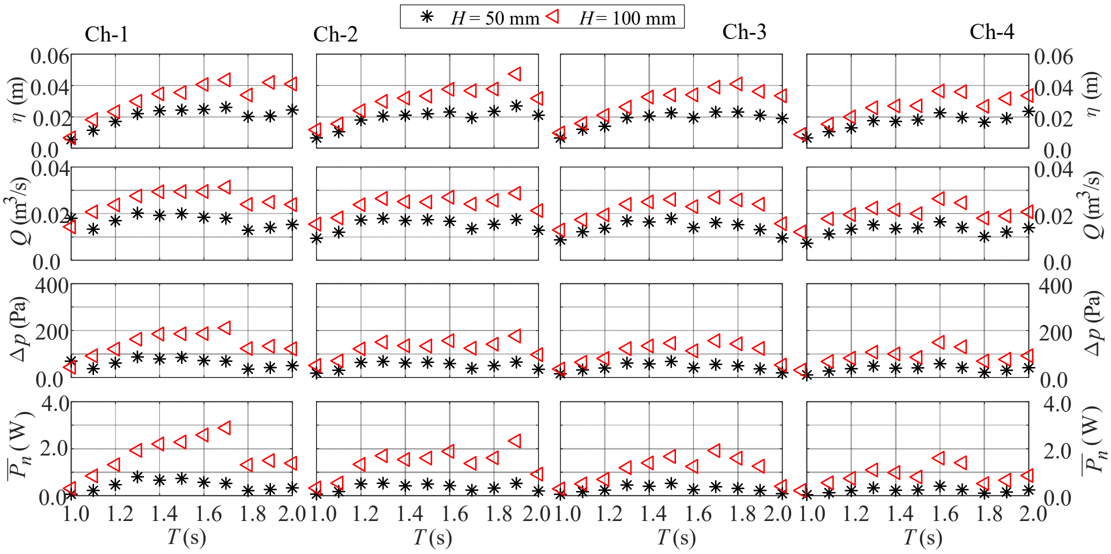

Figure 4.14. Effect of wave height on water surface elevation η (1st row), airflow rate Q (2nd row), differential air pressure Δp (3rd row), and pneumatic power $\overline{P}_n$ (4th row) for different wave periods under a constant orifice opening ratio R_2 = 1.35 % and a draught d = 250 mm

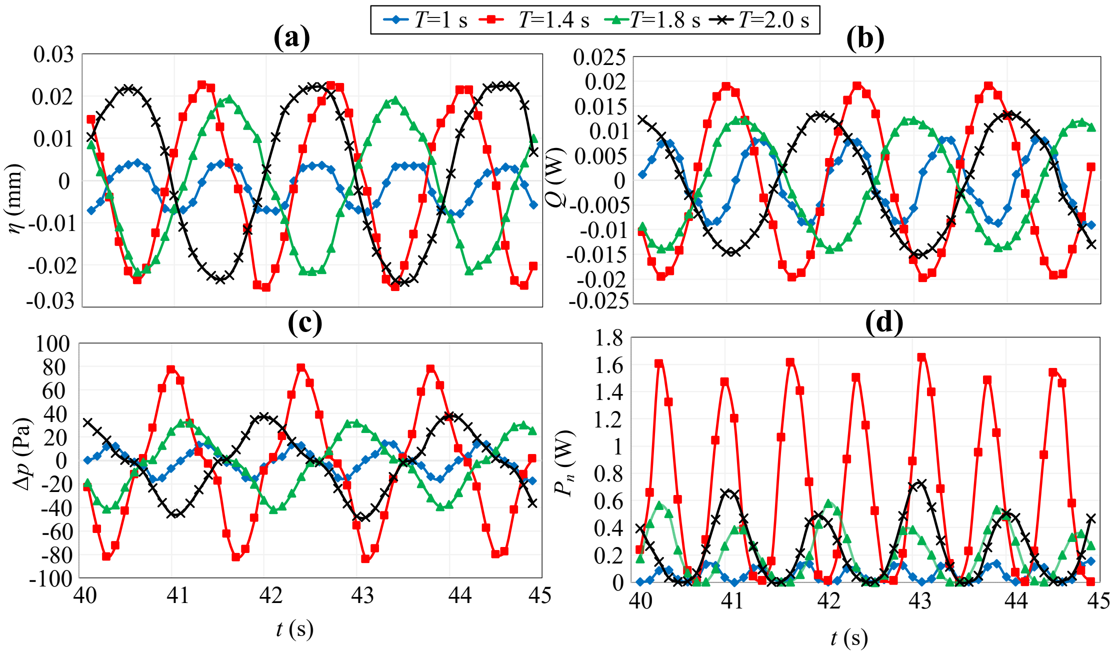

Figure 4.15. Sample time–series data of (a): the water surface elevation η, (b): airflow rate Q, (c): the differential air pressure Δp, (d): and the pneumatic power P_n in the first chamber over four different wave periods at constant wave height H= 50 mm and opening ratio R_2 = 1.35 %

Table 4.3. The absolute average of the changes in the significant parameters as a result of wave height change from 50 mm to 100 mm

Parameters	Ch–1	Ch–2	Ch–3	Ch–4
η (mm)	1.56	1.59	1.58	1.55
Q (m^3/s)	1.51	1.57	1.56	1.58
Δp (Pa)	2.37	2.49	2.47	2.51
P_n (W)	4.25	4.10	4.13	4.21

The overall performance of an OWC device can be assessed based on its capture width ratio (ε) as given by Eq. (3.27). Figure 4.16 illustrate the capture width ratio for each chamber (ε_C) in the MC–OWC device when subjected to a wave height H = 50 mm. It can be observed that the maximum capture width ratio for all chambers (Ch–1 to Ch–4) was achieved at a wave period of about T = 1.3 s, and this ratio was 0.77 in Ch–1, 0.54 in Ch–2, 0.44 in Ch–3 and 0.32 in Ch–4. The drop in the capture width ratio from Ch–1 to Ch–4 follows the drop in the pneumatic energy shown in Figure 4.14 (4th row) considering that the incident energy is constant for all chambers.

The capture width ratio reported in this study, especially Ch–1, is quite a lot larger than what was experimentally found for a typical single chamber OWC device with a vertical plane of symmetry (i.e., identical draught for the front and rear lips) [61, 167-169]. For example, He, et al. [168] reported using 2D wave flume experiments for an OWC device with a single chamber maximum capture width ratio of 0.35, which is lower than the maximum capture width ratio of the first chamber of the model tested in this study. Elhanafi et al. [169] tested a 3D offshore–stationary OWC device that yielded a maximum capture width ratio about 0.26 which is even lower than the capture width ratio for Ch–4 (0.32) of the MC–OWC device considered in this study.

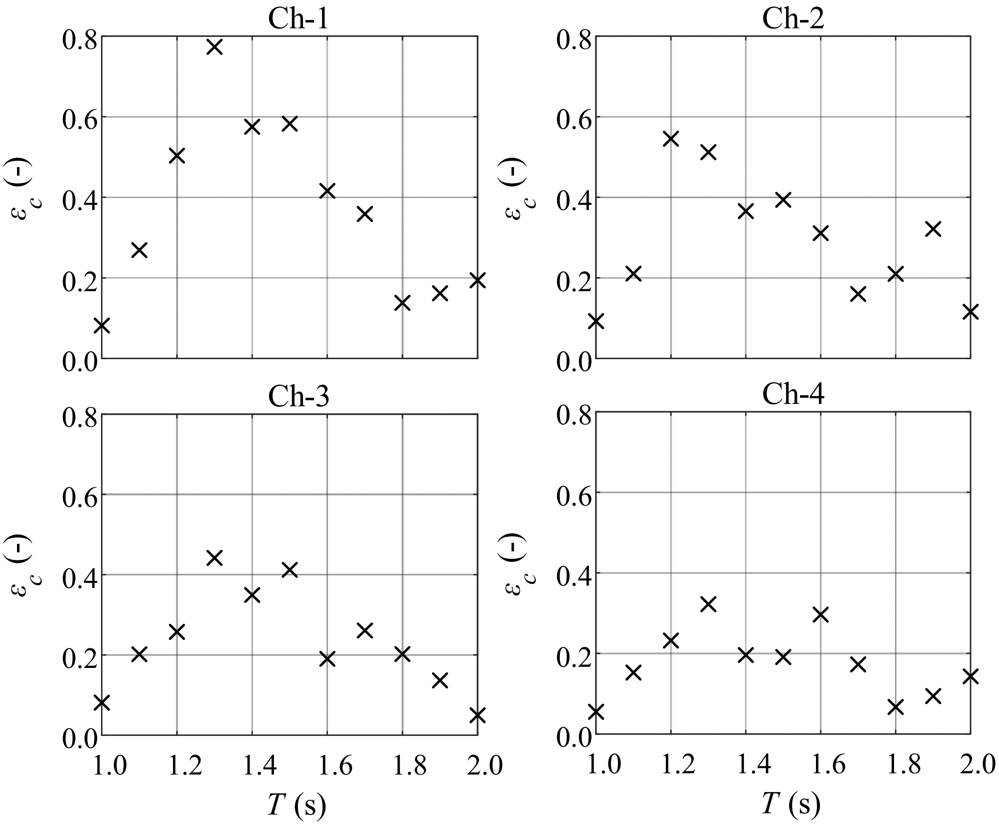

Figure 4.16. Capture width ratio (ε_c) for each chamber of the MC–OWC device at a constant wave height H = 50 mm, a device draught d = 250 mm and an orifice opening ratio R_2 = 1.35 %

During the early stage of research and development of such a MC–OWC device, Dorrell et al. [61] tested a three–chamber MC–OWC and reported a maximum total capture width ratio of 1.07, which is about 39 % less than the maximum value achieved with the first three chambers of the current device. Hsieh et al. [41] developed a two–chamber MC–OWC model and found a maximum total capture width ratio of 0.93, which is about 29 % less than the value captured by Ch–1 and Ch–2 of the model tested herein. This difference could be related to the setup of Hsieh et al. [41] and Dorrell et al. [61] experiment where the devices were mounted on the tank side wall; therefore, the devices were only capable of harvesting the incident energy from underneath the front lip and one side wall of the device (see Figure 2.5). A more closely related work to the present model is the Seabreath that has a total capture width ratio of 0.92 [170]. Recently, He et al. [167] proposed a floating box–type breakwater with dual OWC chambers that was experimentally shown to provide a maximum capture width ratio of about 0.36 with the majority of this value coming from the front chamber (ε = 0.31) that is, in total, about half the value captured by Ch–1 of the model tested in this study.

Figure 4.17 shows the impact the wave period and height have on the total capture width ratio (ε) for the MC–OWC device for a constant device draught d = 250 mm and an opening ratio R_2 = 1.35%. The results demonstrated that ε initially increased with increasing the wave period until a peak value at the resonant period (T = 1.3 s), then ε reduced with a further increase in the wave period. Under a wave height H = 50 m the total capture width ratio (ε) reached a maximum value of 2.1 at T = 1.3 s, but this peak value decreased to 1.4 at the same resonant period when the wave height increased two–fold (H = 100 mm). However, over the entire wave period range, increasing the wave height from 50 to 100 mm had inconsistent effect on device capture width ratio such that ε improved by about 1.1 to 1.3 times in the long–period regime (T > 1.6), but the larger wave height negatively impacted device performance in the short–period regime (T < 1.6) resulting in a reduction in ε by 0.70 to 0.90 times. The improvement in capture width ratio for long–period regime could be attributed to the significant increase in the extracted pneumatic power at these periods (see the 4th row in Figure 4.14), with respect to the energy losses that also increase with increasing the wave height as explained in the energy balance analysis for a single OWC device presented in (i.e., [123]). Overall, the higher capture width ratio shown is Figure 4.17, compared to what was reported in previous research, highlights the effectiveness and significance of the present MC–OWC device.

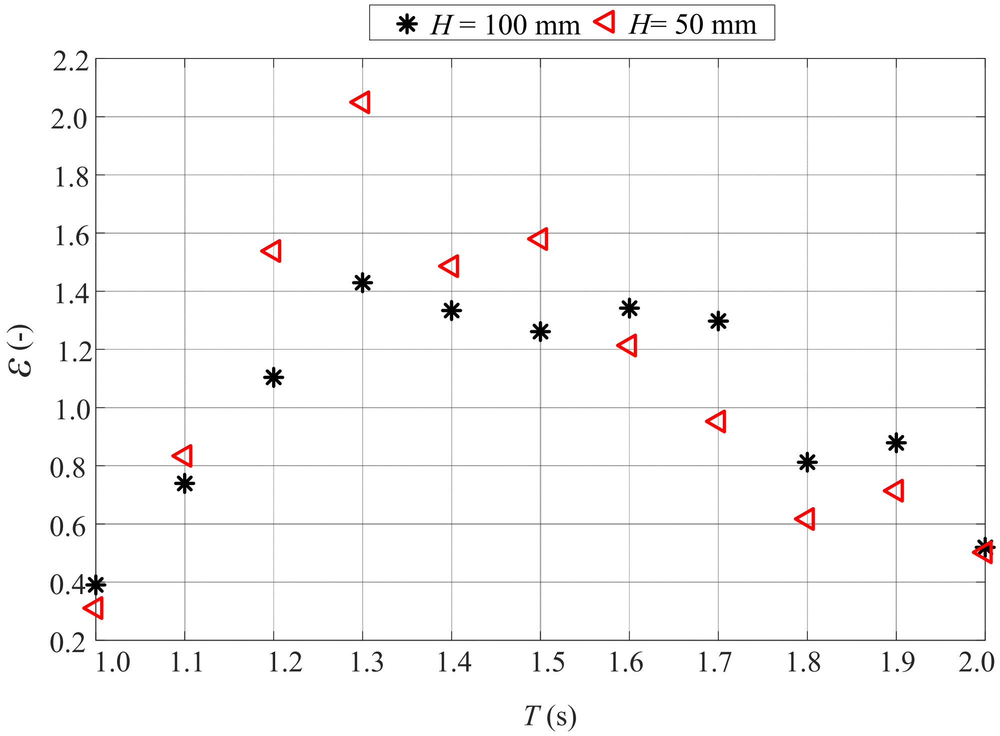

Figure 4.17. Effect of wave height on the total capture width ratio (ε) of the MC–OWC device for different wave periods at a constant device draught d = 250 mm and an opening ratio R_2 = 1.35 %

4.6.4.2 Effect of Device Draught

The results discussed in the previous section were limited to a constant device draught of d = 250 mm; however, it is known that device draught plays an important role in designing an OWC device such that it can be used to tune the device to a range of wave conditions. Therefore, in this section, the device performance was tested for three draught values of d = 200 mm, 250 mm and 300 mm when subjected to a wave height of H = 50 mm over a range of wave periods and under a constant orifice opening ratio R_2 = 1.35 %. The results of these tests are shown in Figure 4.18 for water surface elevation (η, 1st row), the airflow rate (Q, 2nd row), differential air pressure (Δp, 3rd row) and pneumatic power ($\overline{P}_n$, 4th row). It can be seen that as device draught decreased, the device became more tuned to the short wave period regime, which is presented in the higher values of all parameters tested. This effect can be explained, as reported by Ning et al. [155] for a single OWC chamber, by the relation between wavelength and chamber draught as follows. The variation in chamber draught was small enough compared to the wavelength in the long wave regime; hence, a negligible impact on device performance was observed. On the other hand, the sensitivity of device performance to the change in the draught could be related to that the wavelength of the short wave regime was comparable to device draught (i.e., device draught was large enough to impact the incoming wave field).

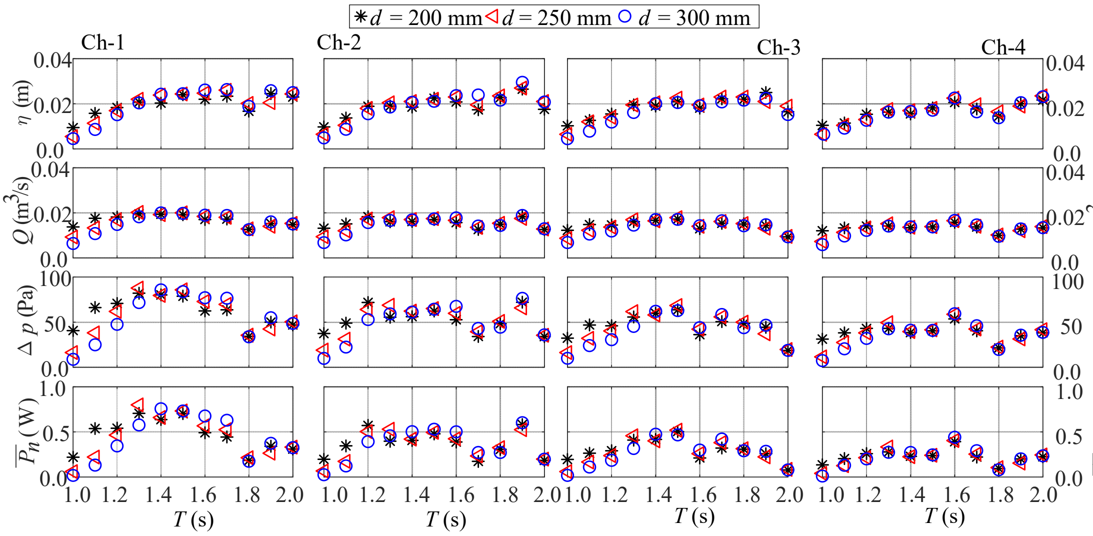

Figure 4.18. Effect of the draught on the water surface elevation η (1st row), airflow rate Q (2nd row), the differential air pressure Δp (3rd row), and the pneumatic power $\overline{P}_n$ (4th row) at constant wave height (H =50 mm) and an orifice opening ratio R_2 = 1.35 %

Changing device draught changes the mass of the water column inside the OWC chamber, which in turn alters its resonant period such that the resonant period decreases as device draught decreases. This observation was quite similar to that of a fixed OWC device [171]. The resonant period of each chamber of the MC–OWC device calculated from Eqs. (3.29) and (3.30) is summarised in Table 4.4 .The results presented in Table 4.4 are highly compatible with the resonant period shown in Figure 4.19 which was calculated by Eq. (3.30). It can be noted that the resonant periods computed by Eq. (3.30) are, on average, 25 % less than those calculated from Eq. (3.30). These differences are due to the parameters used in each formula. In Eq. (3.29) only one design parameter (i.e., draught) was used to estimate the resonant period, while in Eq. (3.30) both device draught and the added mass were used to predict the resonance (see Section 3.6).

Table 4.4. OWC chamber approximated resonant period

Device draught	Approximate formula	
d (mm)	Eq. (3.29)	Eq. (3.30)
200	0.90 s	1.25 s
250	1.00 s	1.33 s
300	1.10 s	1.40 s

The effect of the draught on chamber resonance can also be observed in the results of device capture width ratio presented in Figure 4.19 where the peak capture width ratio (ε) values was shifted to a shorter wave period as draught decreased. During the experiment, the changes in the resonant period as device draught changed were in good agreement with the approximated values from Eq. (3.30) considering that the PTO damping effects were not counted in the approximated values and the wave period resolution (increment) used in the experiment was 0.1 s. Among the three draught values, $d = 250$ mm provided a slightly higher peak capture width ratio of 2.1 compared to 1.8 for the other draught values. It is not only the peak value of ε that changed with device draught but also moving the resonant period from 1.4 s at $d = 300$ mm to 1.2 s at $d = 200$ mm increased and slightly decreased ε for the short and long wave regimes, respectively.

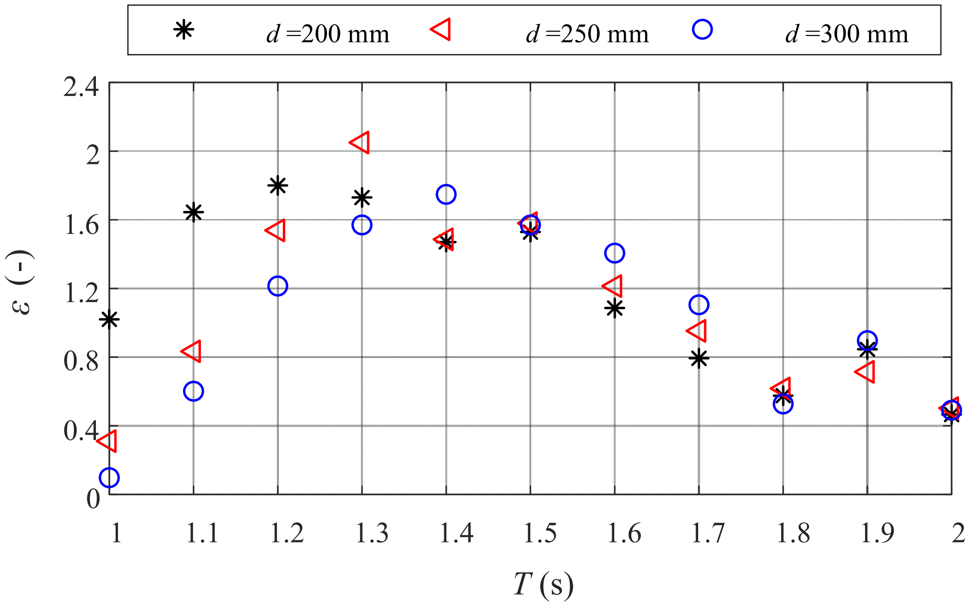

Figure 4.19. Effect of the draught change on the total capture width ratio (ε) at constant wave height H =50 mm and an orifice opening ratio R_2 = 1.35 %

4.6.4.3 PTO Damping Effect

In the previous sections, the results of the tests carried out with one value of PTO damping were discussed. This section elucidates the influence of the PTO damping on the performance of the MC–OWC device. For this purpose, experiments were carried out under three different orifice diameters (i.e. PTO damping values). As addressed in Section 3.5, the pressure drop across the orifice (Δp) can be approximated as proportional to the airflow rate squared. This relationship was quantified in this work for each orifice by the means of a damping coefficient (τ). This coefficient (τ) is considered a key controlling factor of the capture width ratio of an OWC device [113, 155], and can be computed by Eq. (3.25). The values of the damping coefficients used in this study are presented in Table 4.5.

Table 4.5. PTO damping coefficient (τ)

	R_1	R_2	R_3
R_i (%)	0.34	1.35	2.40
τ ($kg^{1/2}$ $m^{-7/2}$)	1854.6	463.7	260.8

In order to better comprehend the impact the PTO damping has on the performance parameters (η, Δp and Q), Figure 4.20 shows the variation of these parameters for all the damping coefficients used in these tests under a wave height H = 50 mm. Overall, it is clear that PTO damping has a similar effect on the performance parameters for all chambers of the MC–OWC device. Figure 4.20 (1strow) shows that the free surface elevation inside each chamber (η) decreased as the damping coefficient increased. For instance, η decreased from 0.035 m in Ch–1 at T = 1.3 s to just about 0.01 m at the same wave period when τ increased from 260.8 to 1854.6 $kg^{1/2}$ $m^{-7/2}$. Since the airflow rate (Q) is related to the free surface vertical velocity, V_z, (assuming incompressible flow), which can be calculated as the rate of change in the free surface elevation (η) with respect to the time (i.e., $V_z = d\eta/dt$), it was expected that the airflow rate follows the changes in η. This correlation is shown in the results presented in Figure 4.20 (2nd row) where it is clear that Q in all chambers has the same trend of η with maximum and minimum values of about 0.03 and 0.005 m^3/s, respectively in Ch–1 at T = 1.3 s. These observations are in line with the results reported in previous research [99, 140, 144] focused on single chamber OWC devices. On the other side, Figure 4.20 (3rd row) illustrates that the differntial air pressure (Δp) had a opposite trend to the airflow rate (Q) such that Δp gradually increased, for example, in Ch–1 from a minimum of 20 Pa to a maximum of 166 Pa at T = 1.6 s with an increase in the damping coefficient . The pneumatic power ($\overline{P}_n$) is influenced by both Δp and Q; hence, the results in Figure 4.20 (4th row) illustrate that there is an certain damping value of 463.7 $kg^{1/2}$ $m^{-7/2}$ at which $\overline{P}_n$

is maximum, and that maximum values was also found to decrease from 0.8 W in Ch–1 to 0.4 W in Ch–4 at $T = 1.3$ s.

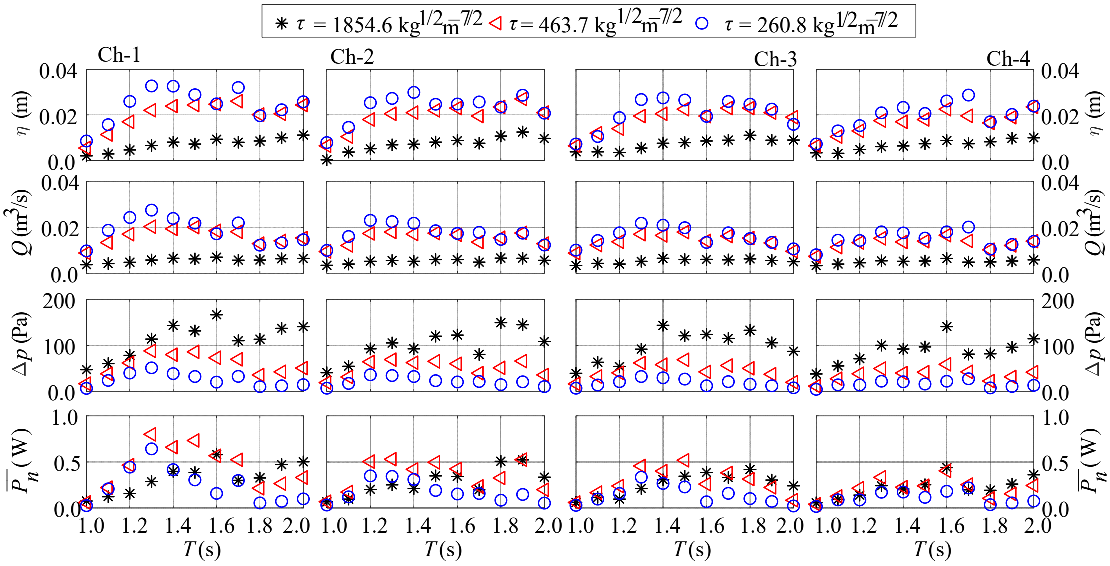

Figure 4.20. Impact of PTO damping on the water surface elevation η (1st row), airflow rate Q (2nd row), the differential air pressure Δp (3rd row), and the pneumatic power $\overline{P}_n$ (4th row) at constant wave height (H =50 mm) and device draught (d = 250 mm) over the wave period listed Table 4.1.

The device capture width ratio depends not only on the wave conditions but also on the PTO damping that the turbine exerts on the system. In order to quantify this influence, Figure 4.21 illustrates the impact of three values of PTO damping on total capture width ratio (ε) of the MC–OWC device when subjected to two different wave heights under a constant draught $d = 250$ mm.

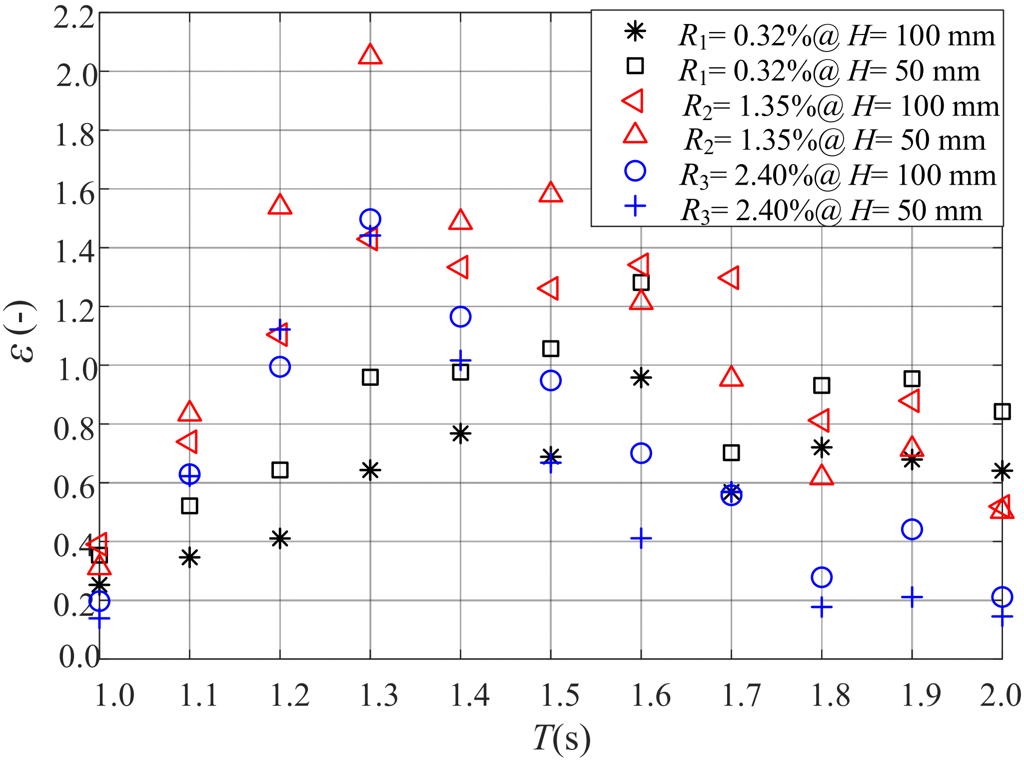

Figure 4.21. The impact of three orifice opening ratios (PTO damping) and two wave heights on the total capture width ratio (ε) under constant draught d = 250 mm

Figure 4.21 also shows that the maximum capture width ratio shifts to a lower wave period as PTO damping decreased (i.e., the opening ratio increased from 0.32 % to 2.4 %). This can be attributed to the decrease in the resonant period of the water column inside the OWC chamber as PTO damping decreased. These observations agree with the experimental and numerical results of onshore and offshore OWC devices reported by [171-173]. This figure also shows the importance of PTO damping that can be utilised to maximise the capture width ratio of the device over a certain wave period range. For example, an intermediate PTO damping (R_2) could improve device capture width ratio for the entire wave period range under both wave heights, but a larger PTO damping (R_1) could be more beneficial for the large–wave period regime, especially for the smaller wave height H = 50 mm.

4.6.5 Irregular Wave Tests

The results in previous sections highlighted the performance of the MC–OWC device under several regular wave conditions, but in reality sea waves are random in nature. Therefore, in this section, the hydrodynamic interaction between irregular waves and the MC–OWC device was examined in the MHL wave flume. Two sea states were characterised by the significant wave height (H_s) and the peak period (T_P) for a constant device draught d = 250 mm under three PTO damping as summarised in Table 4.6.

Table 4.6. Irregular wave test conditions and parameters

Test No.	τ ($kg^{1/2}\ m^{-7/2}$)	H_s (m)	T_z (s)	T_P (s)
Test–1	1854.6 463.7 260.8	0.05	2.5	3.23
Test–2	1854.6 463.7 260.8	0.1	2.75	3.55

The irregular wave conditions of these tests were selected based on the environmental conditions around the Coffs Harbour on the north–coast of New South Wales, Australia. The peak period (T_P) was estimated from the zero–crossing period (T_Z) using the relation of $T_P = 1.29\ T_Z$ [82]. A JONSWAP energy spectrum with a shape parameter (γ) equal to 3.3, Eq. (3.19), was chosen as an input spectrum to the wavemaker paddle to generate the desired sea states spectrum as shown in Figure 4.22. Each test lasted for a duration of an equivalent 20–30 minutes at full scale, which corresponded to approximately 1000 waves. This duration was recommended by [147, 174] to obtain appropriate statistical information for the reconstruction of the energy spectrum.

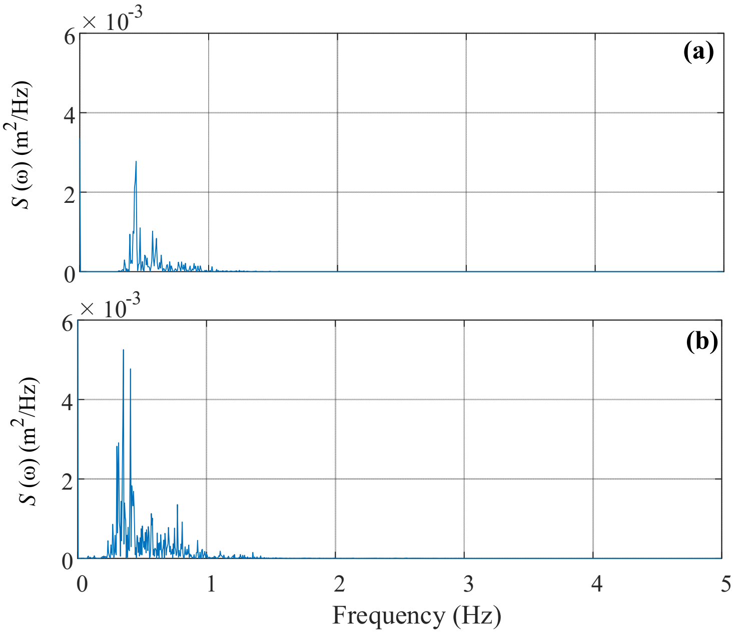

Figure 4.22. JONSWAP energy spectrum, *S* (ω), of the two irregular wave tests described in Table 4.6. (a): Test–1, (b): Test–2

In this test campaign, the mean incident wave power $(P_{\text{in}})_{\text{irrg}}$ was calculated from Eq. (3.21) by the zeroth spectral moment of the incident energy density spectrum, whereas the pneumatic power was calculated in a similar way to the regular wave tests using Eq. (3.28). Figure 4.23 shows the effect of the PTO damping on the total pneumatic power for each test condition listed in Table 4.6. It is obvious that the pneumatic power increased with increasing the significant wave height and the peak period. For example, under an intermediate PTO damping (τ = 463.7 kg$^{1/2}$ m$^{-7/2}$), increasing the significant wave height and peak period increased the extracted pneumatic energy by about 1.8 times. These observations agree with those found for the regular wave conditions shown in Figure 4.20.

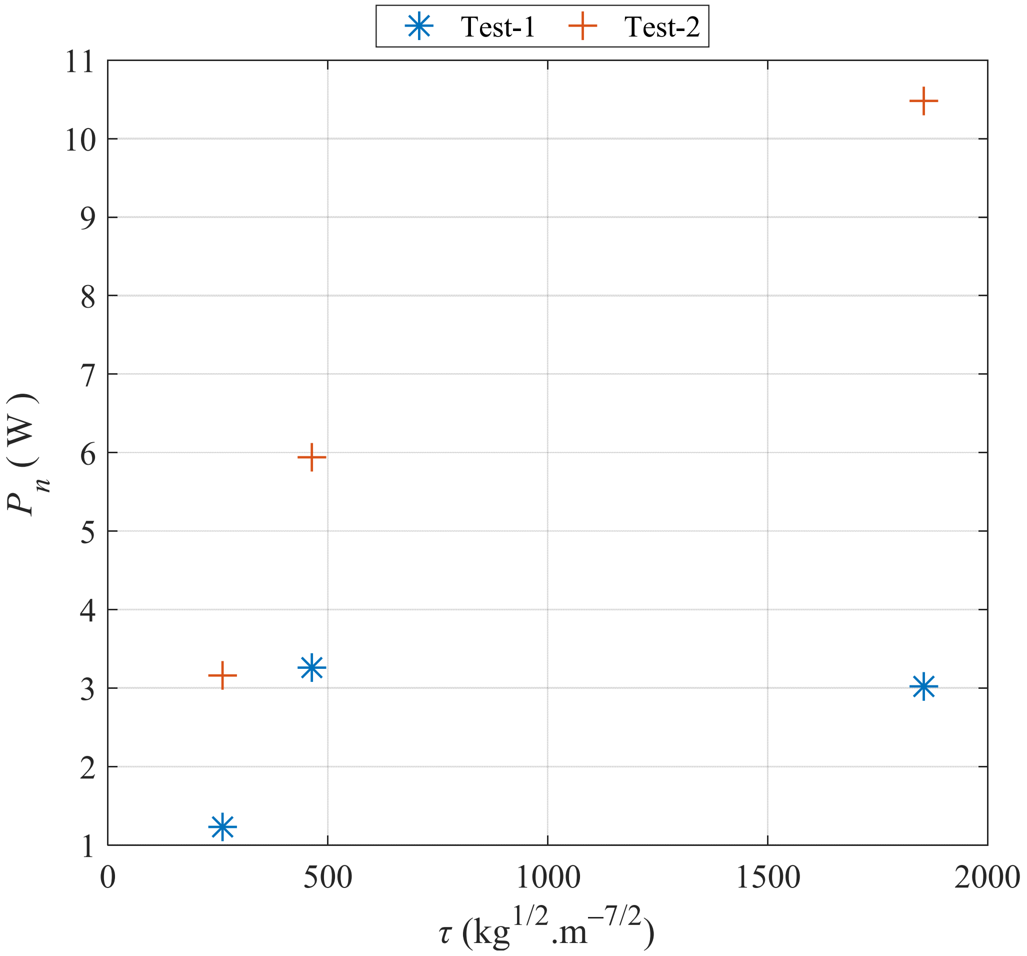

Figure 4.23. Effect PTO damping Variation on the pneumatic power (P_n) of the MC–OWC under the irregular wave conditions listed in Table 4.6

The total capture width ratio of the device when subjected to irregular wave conditions for different PTO damping is shown in Figure 4.24 and summarised in Table 4.7. It can be seen that the device provided a maximum capture width ratio for the irregular wave condition of about 0.95 for Test–1 and 0.80 for Test–2 at a PTO damping τ = 463.7 kg$^{1/2}$ m$^{-7/2}$, which is similar to the damping value found for the regular wave conditions (see Figure 4.21).

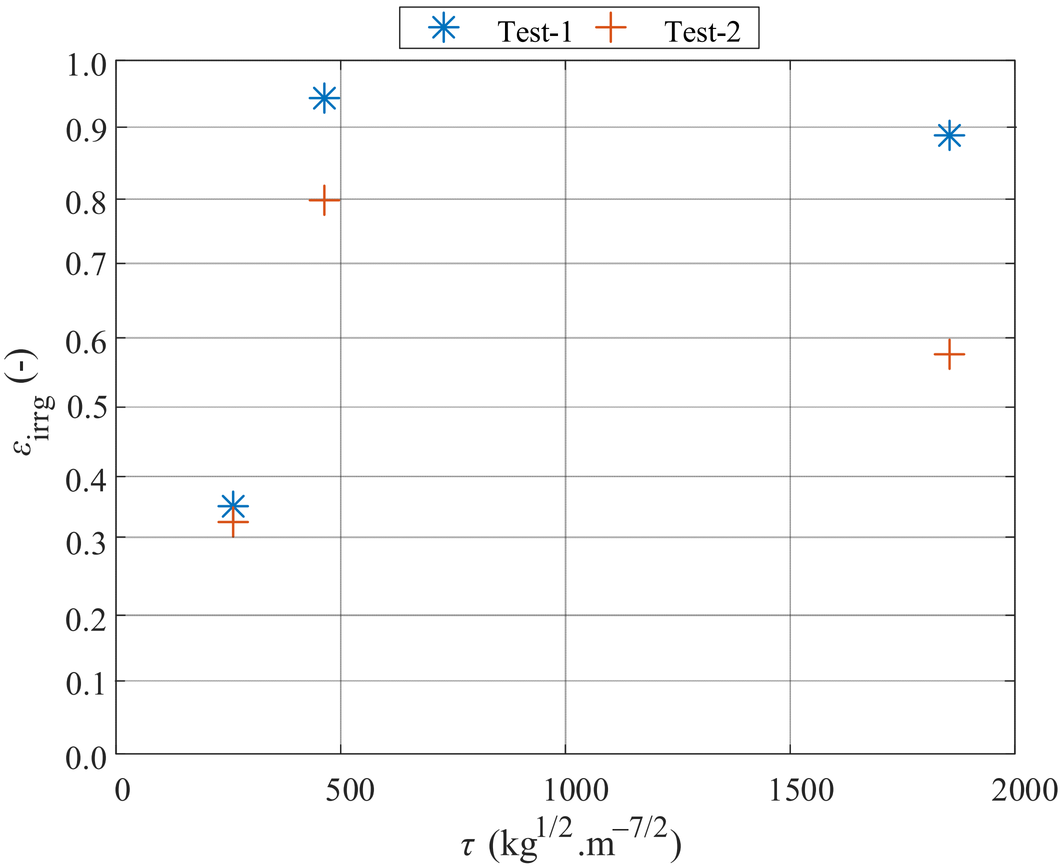

Figure 4.24. Effect of PTO damping on the total capture width ratio (ε_{irrg}) of the MC–OWC under the irregular wave conditions listed in Table 4.6

Table 4.7. The capture width ratio (ε_{irrg}) under irregular wave conditions for different PTO damping

Test No.	τ (kg$^{1/2}$ m$^{-7/2}$)	ε_{irrg} (–)
Test 1	1854.6	0.88
	463.7	0.95
	260.8	0.36
Test 2	1854.6	0.57
	463.7	0.80
	260.8	0.33

4.7 Uncertainty Analysis and Repeatability

Experimental uncertainty analysis is fundamental to ensure high quality and reliable measurements. This section summarises uncertainty study for the measured parameters used in this project. This analysis is based on the comprehensive International

Organization for Standardization (ISO) Guide to the Expression of Uncertainty in Measurement [175], also called GUM and the method adopted by the International Towing Tank Conference (ITTC) [176, 177].

Indeed, the objective of measurements in this project is to determine the value of the particular quantity of the water surface elevation, the differential pressure inside the device chambers and the incident wave height. However, the real value of a measurement is unknown. Thus, the objective of the uncertainty analysis is to estimate the reasonable limits of the measured variable [176]. According to the ISO (2005), uncertainty analysis can be classified as 1) Standard uncertainty grouped into two types. They are: Type A uncertainties and Type B uncertainties; 2) Combined Uncertainty; 3) Expanded Uncertainty.

A standard uncertainty (Us) of the result of measurement expressed as a standard deviation. Type A are used to the results of measurements which were obtained based on the statistical analysis of a series of repeats readings. From these repeats, the standard uncertainty (U_{S-A}) is defined as

$$U_{S\text{-}A} = \frac{S}{\sqrt{n}} \tag{4.1}$$

where S and n are the standard deviation and the number of repeated observations.

Type B is a method of evaluation of uncertainty by means other than the statistical analysis of series of observations such as manufacturer specifications and calibration of the gauges [176].

Firstly, to estimate the uncertainty Type A, it may only select unique test conditions for which repeat runs be undertaken. Therefore, three runs for three test conditions under two wave heights are selected as described in Table 4.8. The estimated results of uncertainty Type A were presented in Table C.1 in Appendix C.

Table 4.8. Repeatability test conditions

Test Number	Wave height H (mm)	wave period T (s)
Test 1	50	1.6
Test 2	100	1.6
Test 3	50	1.2

Secondly, uncertainty Type B can be evaluated in this type of experiment by considering the calibration process of the gauges [176]. All of the gauges utilised in this project are linear and calibrated through the end–to–end approach by using the same data acquisition system and LabVIEW software utilised in data collection. Therefore, uncertainty Type B can be evaluated by the stander error of estimate (σ_{est}) as in Eq.(4.2)

$$\mathrm{U_{S\text{-}B}} = \sigma_{est} = \sqrt{\frac{\left(Y_i - \grave{Y}_i\right)^2}{N-2}} \tag{4.2}$$

where N is the number of calibration sample, Y_i is the calibrated data, and $\grave{Y}_i$ is the fitted value. The estimated results of uncertainty Type B were presented in Table C.2. in Appendix C.

As a result, the standard uncertainty can be evaluated by the combination of Type A uncertainty and Type B uncertainty as given by Eq.(4.3).

$$\mathrm{Us} = \sqrt{\left(\mathrm{U_{S\text{-}A}}\right)^2 + \left(\mathrm{U_{S\text{-}B}}\right)^2} \tag{4.3}$$

The third type of uncertainty is a combined standard uncertainty which is obtained from the values of a number of other quantities. Based on ITTC recommended procedures, this type of uncertainty cannot be computed in this project because of using one gauge in each measurement values (e.g. P1 and G1 gauges used to measure the differential air pressure and water surface elevation inside the first chamber).

The expanded uncertainty could be computed by using Eq.(4.4) according to ITTC [176]

$$\mathrm{U_E} = \mathrm{Us} \times k_c \tag{4.4}$$

where k_c is a coverage factor which equals to 4.303 based on T–Distribution table that achieved 95% confidence level for the three runs applied.

Table 4.9 summarised all of the above uncertainty analysis for the experiments conducted in this project. The measured data in the second test (MHL) displays excellent repeatability, as shown in Figure 4.25 and Figure 4.26 (see Appendix C for further test condition). These conditions included non–sequentially repeated runs as recommended by ITTC [38] to demonstrate experiment repeatability.

Table 4.9. Experiment uncertainty

	Standard Uncertainty					Expanded Uncertainty	
Instruments	U_{S-A} (H=50mm)	U_{S-A} (H=100mm)	U_{S-B}	Us (H=50mm)	Us (H=100mm)	(H=50mm)	(H=100mm)
G_{in} (mm)	±0.265	±0.271	±0.0020	±0.265	±0.271	±1.140	±1.166
G_{out} (mm)	±0.124	±0.125	±0.0420	±0.131	±0.132	±0.563	±0.567
G1 (mm)	±0.008	±0.008	±0.1341	±0.134	±0.134	±0.578	±0.578
G2 (mm)	±0.015	±0.015	±0.0086	±0.017	±0.017	±0.074	±0.074
G3 (mm)	±0.011	±0.011	±0.0126	±0.017	±0.017	±0.072	±0.072
G4 (mm)	±0.003	±0.003	±0.0163	±0.017	±0.017	±0.071	±0.071
P1 (Pa)	±0.833	±0.775	±0.0012	±0.833	±0.775	±3.584	±3.335
P2 (Pa)	±2.087	±1.443	±0.0020	±2.087	±1.443	±8.980	±6.209
P3 (Pa)	±0.549	±0.662	±0.0004	±0.549	±0.662	±2.362	±2.849
P4 (Pa)	±1.259	±0.692	±0.0041	±1.259	±0.692	±5.418	±2.978

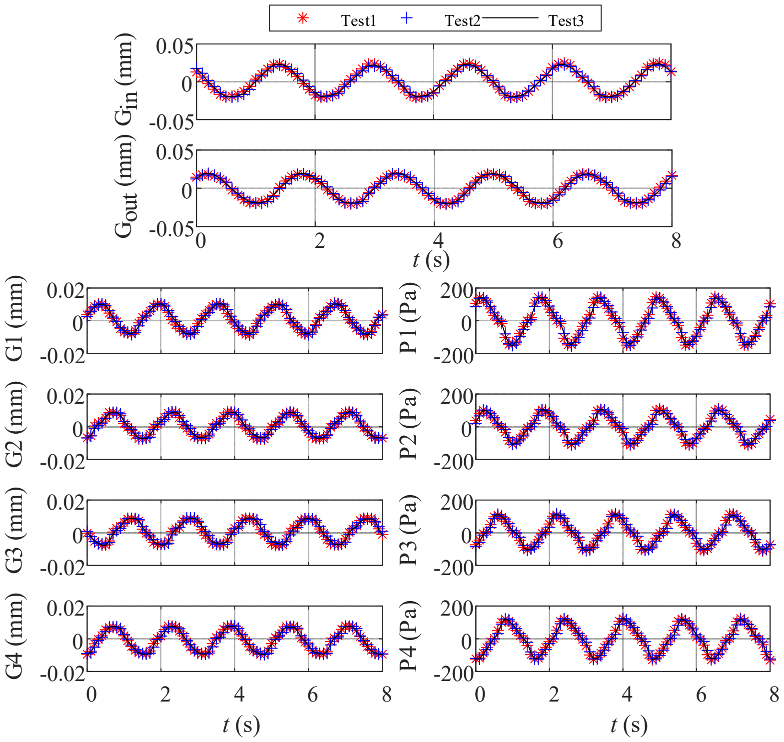

Figure 4.25. Sample time–series data of the experiment repeatability for a wave condition of *H*= 50 mm, *T*= 1.6 s and a constant opening ratio of R_i= 1.34%

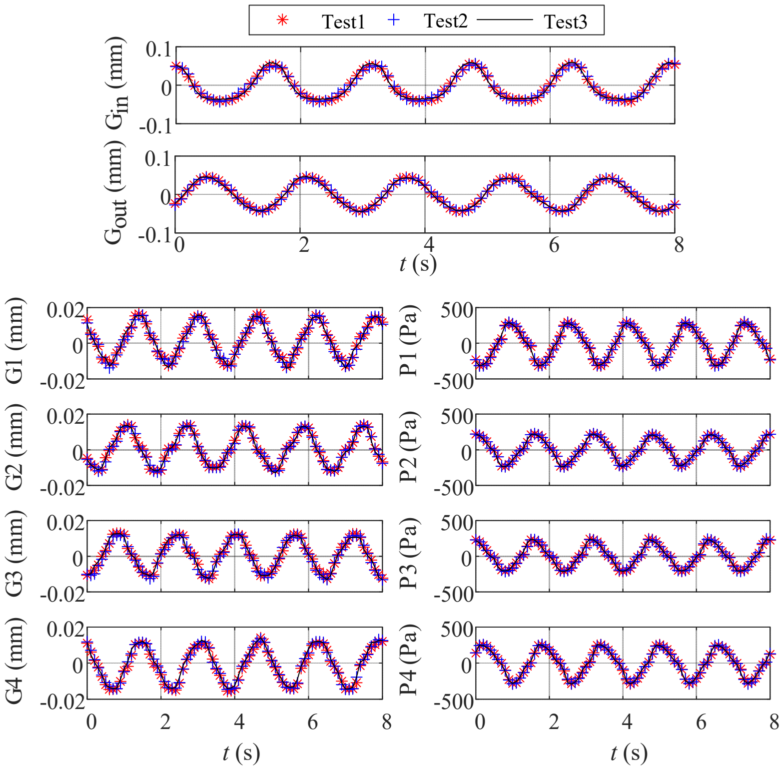

Figure 4.26. Sample time–series data of the experiment repeatability for a wave condition of *H*= 100 mm, *T*= 1.6 s and a constant opening ratio of R_i= 1.34%

4.8 Summary

In this chapter, a comprehensive series of 198 physical model tests were carried out to understand how different parameters affect the capture width ratio of an MC–OWC chamber. The parameters investigated were 1) the wave conditions including wave height and period for the regular wave tests and significant wave height and peak period irregular wave tests, 2) device draught and 3) the PTO damping representing the damping exerted by the turbine on the motions of the oscillating water column. The PTO damping was modelled by an orifice (circular opening) of varying diameters, each diameter corresponding to a value of a damping coefficient.

From the results discussed in this chapter, the following main conclusions can be drawn. The damping induced by the PTO damping on the system is a key factor that most affects the device performance. Increasing the PTO damping leads to a higher chamber pressure, a lower free surface motion and a lower airflow rate for all the incident wave periods. The wave period at which the peak capture width ratio occurs was found to reduce as the PTO damping decreases. Furthermore, among the three damping values tested, the intermediate with an orifice opening ratio R_2 = 1.35 % was found to be the optimum damping that can maximise the capture width ratio for all chambers over whole regular and irregular wave conditions tested. Device draught was also found to be a crucial parameter that could tune the device to a range of wave conditions; hence improving the capture width ratio. There was a draught value (250 mm) that could maximize device capture width ratio (ε = 2.1) for a given wave condition (H = 50 mm and T = 1.3 s). However, decreasing device draught shifts in the maximum capture width ratio to a shorter wave period, which in turn tunes the device over the short wave period regime, allowing for more energy to be extracted.

Chapter 5 : TIME–DOMAIN MODEL

5.1 Introduction

Among the different methods proposed for OWC modelling, a simplified and less computational time domain model might be useful in the initial stages of a device development. Such a simplified model might be used to preliminary specify the variables to be measured (e.g. differential air pressures, water surface level).

In this chapter, governing equations of the coupling between the hydrodynamic (i.e. rigid piston model) and the thermodynamic effects for the MC–OWC device with an orifice used to represent the nonlinear PTO system, are applied in the time domain. The time–domain model equations were then implemented in MATLAB/Simulink.

The MATLAB/Simulink model enables the generation of the water surface elevation and differential pressure inside the chamber in the time–domain for regular wave conditions. The numerical predictions are compared with experimental data performed on a model scale MC–OWC at the UTS wave flume. The modelling methodology was first applied to the single chamber. Then it was extended to study the four chambers.

5.2 Mathematical Model

This section is focused on the development of a compound system of the hydrodynamic and thermodynamic operations in time–domain to analyse the performance of a single OWC device in regular wave conditions. This model also has been used for modelling trapped air cavities for marine vehicles [13].

5.2.1 Theoretical Considerations

Most of the time–domain models are based on the hypothesis of incompressibility. Despite this, air compression has a significant effect on the model efficiency at the full–scale. However, often it has been ignored in small–scale models when its pressure change and air volume are both small [149, 178]. Besides, in this model, the diffraction of the wave field has been neglected. The flow field is considered as a two–dimensional irrotational flow. The vortex and viscous effects that may occur inside the chamber are also not considered. Since the dimensions of the proposed model are small compared to the wavelength, LWT is applied to represent the incident wave in this model [20].

5.2.2 Rigid Piston Model

The most straightforward way of modelling an OWC device is to treat it as a simple harmonic oscillator. Hence, vertical motions of the OWC device chamber (in this project a rectangular chamber is used) are determined by the solid mass *m* of the rectangular chamber and the hydro–mechanical loads on the chamber.

For a spring mass damper system, shown in the top–right corner in Figure 5.1, which simulates a hydrodynamic behaviour of the rectangular chamber, Newton's second law

$$\left(M + M_a\right)\frac{d^2\eta}{dt^2} + B\frac{d\eta}{dt} + K\eta = f\left(t\right) \tag{5.1}$$

gives:

The terms η, $d\eta/dt$ and $d^2\eta/dt^2$ are displacement, velocity and acceleration caused by the hydrodynamic reaction as a result of the movement of the rectangular chamber with respect to the water. The water is assumed to be ideal and thus to behave as in a potential flow.

M in Eq.(5.1) is the mass of the water column inside the OWC chamber at SWL which can be assumed as

$$M = \rho_w \times d \times A_1 \tag{5.2}$$

where A_1 is the chamber area, ρ_w is the water density (998.2 kg/m^3 at 293 K) and d is the length of the wet surface (draught) of the chamber at SWL as illustrated in Figure 5.1.

M_a is the added mass (kg); it is considered as a problematic characteristic to determine due to inflow/outflow variations caused by the incident wave [179]. M_a could be approximated by assuming the added volume of the rectangular chamber is a function of the area of the internal free surface area of the chamber, and the density of water [179]. Moreover, Patel et al. [180] utilized this assumption to compute the added mass of semisubmersible vessels. In this work, the added mass to the rectangular chamber can be expressed as

$$M_a = \rho_w \times \eta \times A_1 \tag{5.3}$$

B in Eq.(5.1) is the damping coefficient. The significant causes of damping in an OWC are radiation of waves caused by the motion of the water column and turbulent losses within the water [181]. Both of these effects are highly dependent on the frequency of oscillation. Patel et al. [180] used another way to estimate the damping value for semisubmersible vessels. They assumed that B is a function of the M, M_a and hydrostatic restoring coefficient, K. B is defined as 10% of its critical value ($\sqrt{K\left(M + M_a\right)}$. This hypothesis was validated from the iterative technique that was used by Patel et al. [180] to account for the non–linear drag damping force; hence, the damping coefficient B of the OWC device can be expressed as

$$B = 0.2\sqrt{K\left(M + M_a\right)} \tag{5.4}$$

K is the hydrostatic restoring coefficient attributed to hydrostatic pressure and is expressed as

$$K = \rho_w \times g \times A_1 \tag{5.5}$$

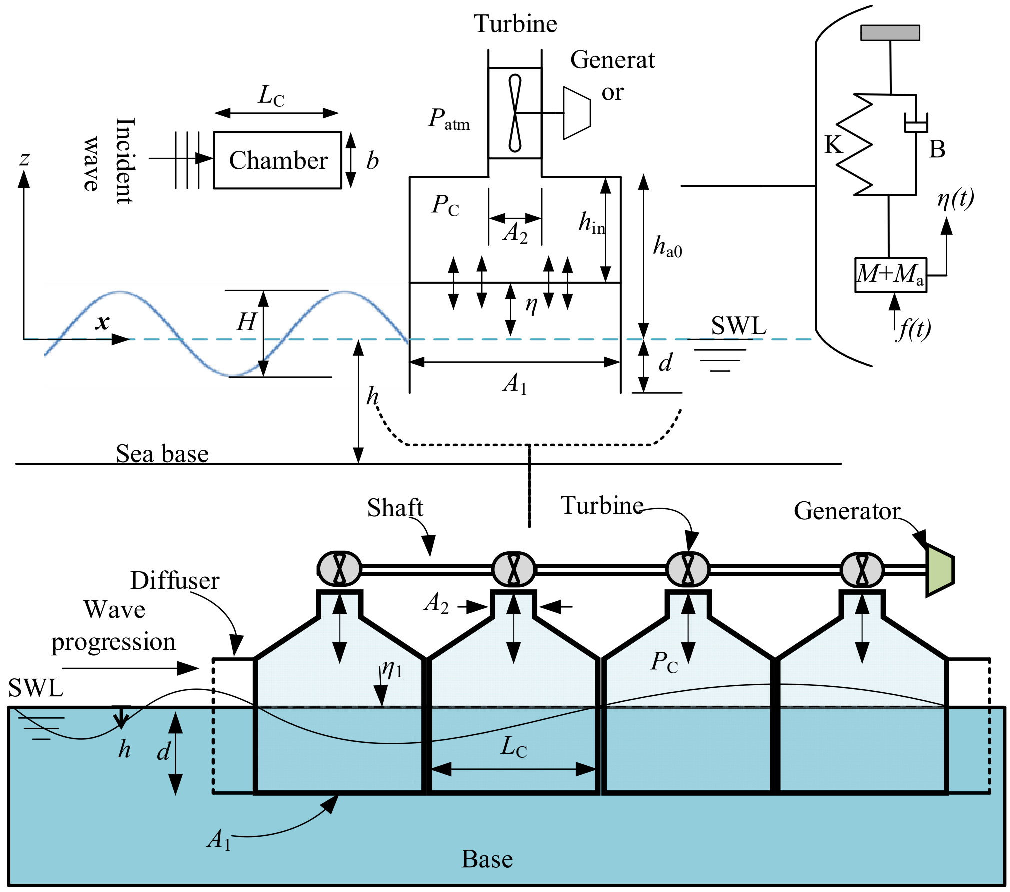

Figure 5.1. Schematic representation of the numerical model OWC

Excitation force

The right–hand side of Eq.(5.1) is the time–varying excitation force $f(t)$ that acts on the water column. It is made up of three forces which includes the added mass force $F_a(t)$, the Froude–Krylov force $F_{FK}(t)$ at the bottom and the vertical force due to the varying air pressure inside the chamber $F_{\Delta p}(t)$. Figure 5.2 illustrates these forces where forces that are directed toward positive z–axis are assigned positive signs. These forces are computed through numerical integration to account for spatial phase variations in wave–particle velocities and accelerations and the attenuation of these properties with depth as labelled in [180].

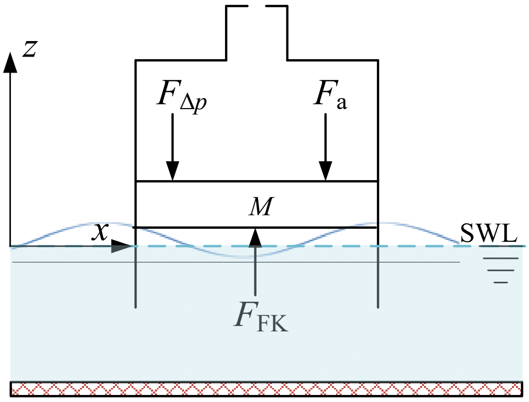

Figure 5.2. OWC chamber free body diagram

The total force acting on the water column can be represented as

$$f(t) = F_{FK} - F_a - F_{\Delta p} \tag{5.6}$$

$F_a(t)$ is the added mass force that acts as the damping force and is defined by

$$F_a = M_a \times \left(\frac{d^2 w}{dt^2} - \frac{d^2 \eta}{dt^2} \right) \tag{5.7}$$

d^2w/dt^2 is the time derivative of the vertical component of the water particle velocity and was defined in Eq.(5.1) and $d^2\eta/dt^2$ is the second time derivative of Eq. (3.7).

$F_{FK}(t)$ is the Froude–Krylov force term, which is generated by the pressure field that is acting on the bottom of the water column and drives the water upwards [182]; it can be represented by

$$F_{FK} = p_w \times A_1 \tag{5.8}$$

where p_w(t), was defined in Eq.(3.11).

The last element in the total force is the variation of the air force in the chamber $F_{\Delta p}$ (t), which is defined by

$$F_{\Delta p} = \Delta p \times A_1 \tag{5.9}$$

where Δp, is the difference between the pressure inside the chamber and atmospheric pressure which will be defined in the next section.

Finally, the equations of motion need to be rewritten such that the right–hand side does not include the accelerations ($d^2\eta/dt^2$). Therefore, the governing equation of motion that describes the motion of the water column in regular waves is

$$\frac{d^2\eta}{dt^2} = -\left(\frac{0.2}{d}\sqrt{g\left(d+\eta\right)}\right)\frac{d\eta}{dt} - \frac{g}{d}\eta + \frac{\psi}{d}\frac{\Delta p}{d\,\rho_w} \tag{5.10}$$

where

$$\Psi = \begin{cases} -g\dfrac{cosh\left[k\left(h-d\right)\right]}{cosh\left(kh\right)}-\eta\times\omega^2 \\ +\dfrac{sinh\left[k\left(h-d\right)\right]}{sinh\left(kh\right)}\times\dfrac{H}{2}\times cos\left(\omega t+\theta\right) \end{cases} \tag{5.11}$$

5.2.3 Thermodynamics Model

The theoretical analysis was performed under the assumption of adiabatic processes in the OWC chamber. The adiabatic assumption is justified, since the amount of heat exchanged is a small fraction and could be neglected in the relatively short period of a wave cycle where the air inside the chamber is a constant temperature [136]. Thus, the mass of air in the chamber can be expressed as

$$m = \rho_{air}V \tag{5.12}$$

where m, is the time–dependent air mass in the air chamber, V, is the air volume of the chamber and ρ_{air}, is the density of air inside the chamber in kg/m^3.

By differentiating Eq. (5.12) the change of mass within the air chamber can be represented by the Eq. (5.13). Further, the airflow across the orifice which is dictated by the movement of the internal water surface is simply expressed as in Eq.(5.14).

$$\frac{dm}{dt} = \rho_{air}\frac{dV}{dt} + V\frac{d\rho_{air}}{dt} \tag{5.13}$$

$$Q_w = -\frac{dV}{dt} \tag{5.14}$$

where Q_w, is the rate of airflow in m^3/s based on the change in volume of the air chamber caused by the motion of the internal water surface.

There are significant differences in air condition between the inhalation and exhalation processes. In exhalation, the air that passes through the orifice (turbine) to the atmosphere and has a high density. The air during the exhalation could be considered as a uniform body because it does not go through any mixing as no new air is introduced to the system during this process. In the inhalation process, the air within the chamber is depressurised, and its density is lower than the atmosphere. When air at atmospheric pressure is breathed in, a complex mixing process occurs between the air within the chamber and the air induced from the atmosphere that has passed through the orifice. Hence, the process is under the compressibility effect of air and air density changing across the orifice. So, the air volume flowrate must be considered for exhalation and inhalation differently due to the airflow through the orifice with different densities as shown in Eq.(5.15)

$$\begin{cases} Q_p = -\dfrac{1}{\rho_{air}}\dfrac{dm}{dt}, p \geq 0 \\ Q_p = -\dfrac{1}{\rho_{atm}}\dfrac{dm}{dt}, p < 0 \end{cases} \tag{5.15}$$

where p is the gauge pressure of the OWC chamber in Pa and Q_P is the rate of volumetric airflow across the turbine in m^3/s.

For the compressible air assumption, the input power in the OWC device is calculated by the chamber pressure multiplying the flow rate driven by the water surface, as

$$P_w = pQ_w \tag{5.16}$$

where the output power available to the PTO system is

$$P_n = pQ_p \tag{5.17}$$

In the case of the incompressible air assumption which is usually applied to a small–scale model, the chamber air density and temperature are constant. Thus, the mass change rate is purely caused by the change of the air volume, and the flow rate through the orifice ($Q_p = Q_w$). As a result, the wave generated power is fully transferred to the power take–off system and therefore $P_n = P_w$

The thermodynamic problem of the OWC device has been simplified in order to model the differential pressure inside the OWC chamber, therefore, the periodic compression and expansion of the air contained inside the chamber is considered as an isentropic process. Under such an assumption, a state equation for the open system of the air chamber can be simply expressed as

$$\frac{p_{atm} + \Delta p}{\rho_{air}^{\gamma}} = \frac{p_{atm}}{\rho_{air}^{\gamma}} \tag{5.18}$$

where $p_c = p_{\mathrm{atm}} + \Delta p$ and γ denotes the heat capacity ratio which is equal to 1.4 for the fresh air at 293 K.

Sheng et al.[133] linearised Eq.(5.18), so that the air density in the chamber is linear with the chamber pressure as

$$\rho_{air} = \rho_{atm}\left(1 + \frac{\Delta p}{\gamma p_{atm}}\right) \tag{5.19}$$

The ideal gas law states

$$p_c V = m\dot{R}T_k \tag{5.20}$$

where m is the mass of air inside the chamber, $\dot{R}$ is the ideal gas constant which is equal to 287.1 J/kg.K for dry air. The ambient temperature T_k is in Kelvin, which is assumed 293 K.

The temperature changes due to the changes of the pressure in the chamber given by an equation

$$T_c = T_k\left(1+\frac{\Delta p}{p_{atm}}\right)^{\frac{\gamma-1}{\gamma}} \tag{5.21}$$

where T_c is the chamber temperature in Kelvin.

Gervelas et al.[131] performed a logarithmic differential to the Eq. (5.21) and inserted it in the time differential of the ideal gas equation to produce Eq.(5.22)

$$\gamma\frac{P_c}{V}\frac{\partial V}{\partial t}+\frac{\partial P}{\partial t}=\frac{\gamma\dot{R}T_k}{V}\frac{\partial m}{\partial t} \tag{5.22}$$

where $\partial m/\partial t$ can be expressed as $\dot{m}$ the mass flowrate which flows out of the chamber and ($g.\ \dot{R}.\ T_k$) is equal to the speed of sound in the air c_s. Therefore, Eq.(5.22) can be rearranged to

$$\frac{\partial\Delta p}{\partial t}+\frac{c_s^2}{V}\dot{m}=\frac{\gamma p_c}{V}\frac{\partial V}{\partial t} \tag{5.23}$$

At this point of derivation, a relation between the differential air pressure Δp and the mass flow rate $\dot{m}$ has been described. Further simplifications can be obtained by using the standard orifice theory as given in Eq.(3.26).

Inserting Eq.(3.26) into Eq. (5.22) yields the governing equation for the pressure drop inside the chamber Δp:

$$\frac{d\Delta p}{dt}=\frac{RT_kC_dA_2}{A_1\left(h_{a0}-\eta\right)}\sqrt{2\Delta p\,\rho_{air}}+\gamma\left(\frac{P_C}{h_{a0}-\eta}\right)\frac{d\eta}{dT} \tag{5.24}$$

where A_2 is the circular orifice area, and h_{a0} is the height of the top cover of the chamber relative to the SWL as illustrated in Figure 5.1.

5.3 MATLAB/Simulink Model Structure

In this section, the details of the time–domain model (i.e. hydrodynamic and thermodynamic models) implementation is presented. The MATLAB/Simulink modelling methodology is explained as a flow–chart in Figure 5.3 and is applicable for modelling both single–chamber and four–chambers OWC devices with simple geometry. This model consists of three main parts: 1) system input (the wave conditions and device geometry), 2) the time–domain equations of the physical system of Eqs.(5.10), (5.11) and (5.24) (see Figure D.1 in Appendix D), and 3) the output of the simulation results which are the superposition of the internal water surface elevation η, the differential air pressure Δp inside the chamber and the airflow rate through the orifice Q.

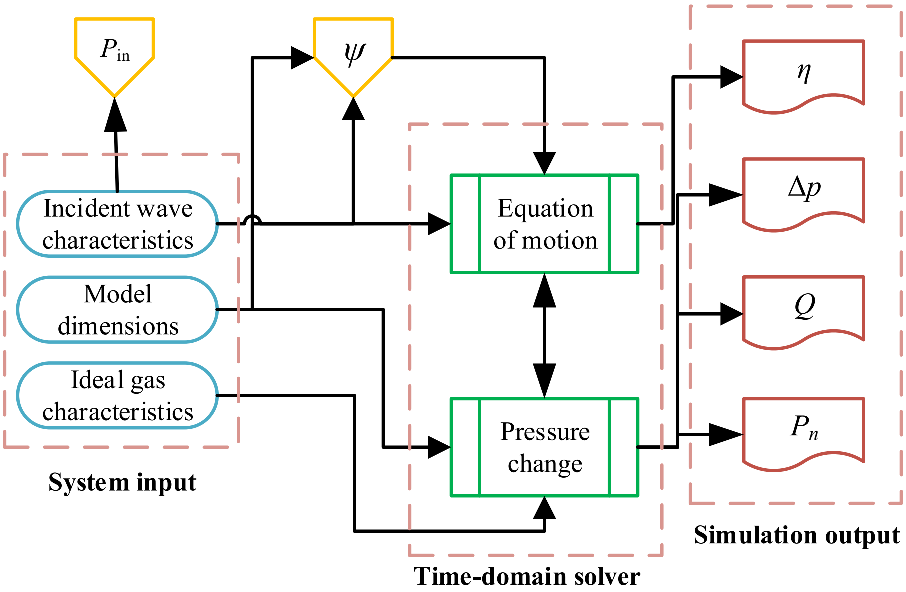

Figure 5.3. The complete single chamber OWC model in MATLAB/Simulink.

The MATLAB/Simulink model solves the system of equations using the ode45 numerical solver. This is both robust and a relatively fast solver and is based on the Dormand–Prince Runga–Kutta formula [183]. Such modelling uses the data collected through UTS tank testing that has been previously obtained in Section 4.3 . In the first stage of such model development, the single chamber OWC model with a rectangular cross–section includes a block calculation of the heave motion of the water column and the pressure inside chambers with input blocks parameters as given in Table 5.1 (see Figure 4.2). A wave condition of $H = 87$ mm and $T=1$ s was used for all the simulations performed in this section. For clarity, the simulation results of only 10 s are presented as shown in Figure 5.4. The values of incident wave power, P_{in}, calculated in Eq. (3.14) and pneumatic power, Pn, calculated in Eq.(3.28) were used to estimate the performance of the MC–OWC device. The time–series MATLAB reults of these parameters is shown in Figure 5.4.

Table 5.1. Geometrical parameters of the MC–OWC device illustrated in Figure 4.2

Parameters	Descriptions
Chamber length L_c	365 mm × 4 chambers
Chamber width b	150 mm
Front and back wall ($h_{out} + d$)	265 mm
Orifice diameters d_o	36 mm
Draught (d)	134 mm

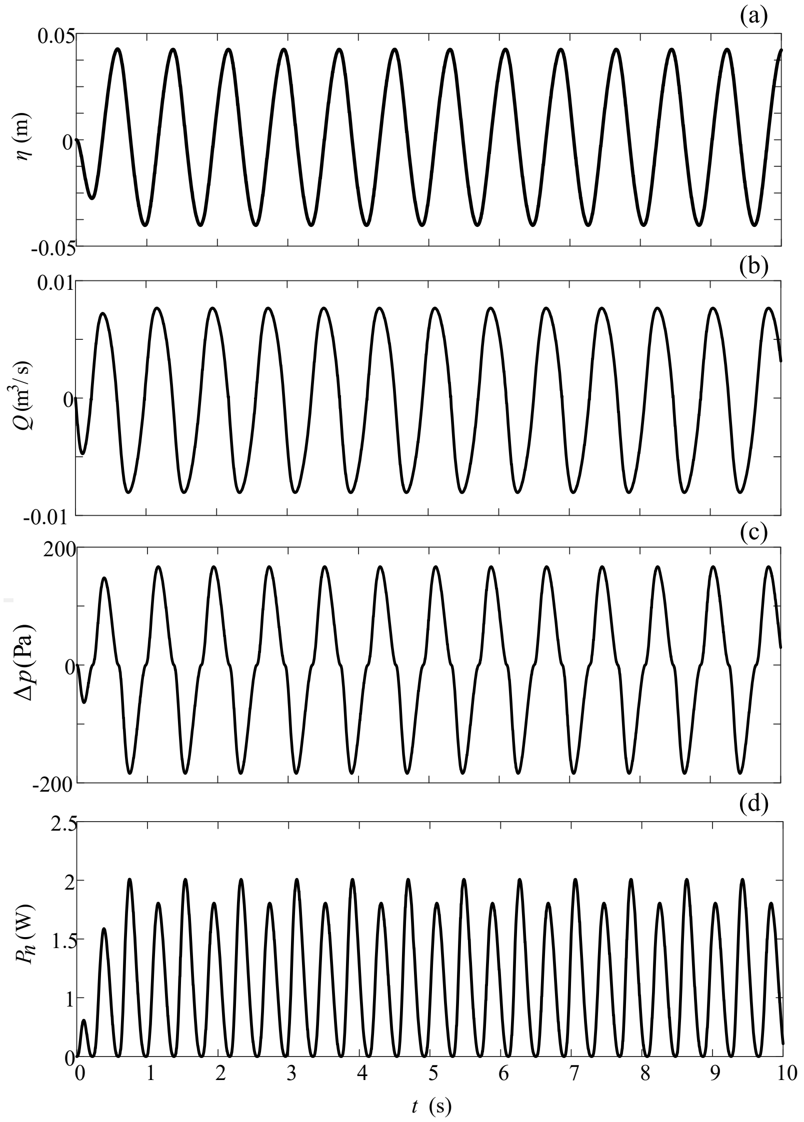

Figure 5.4 Sample of the temporal data of MATLAB/ Simulink for single chamber OWC device at H= 87 mm and T=1s for (a): water surface elevation inside chamber η, (b): airflow rate Q, (c): the differential pressure Δp, (d): pneumatic power P_n.

In the second part of the time–domain model development, the geometry of the four chambers OWC model was chosen. Similar to the single–chamber OWC time–domain model, the four–chamber OWC time–domain model takes the coupling of Eq. (5.10) and Eq.(5.24) as its input and solves for the water surface elevation inside chamber η, airflow rate Q, the differential pressure Δp, and pneumatic power P_n. The experimental data conducted at the UTS wave flume was used to tune the damping coefficient (B) defined in Eq. (5.10) for all device chambers. The results in Figure 5.5 show that the simulation models were able to predict the internal water elevation η (see Figure 5.5

(a)), the airflow rate through the orifice Q (see Figure 5.5 (b)) and the pressure difference Δp (see Figure 5.5 (c)) to a certain degree as will be discussed in the next section. Figure 5.5 (d) shows a time–dependent plot of the pneumatic power available for each chamber.

The plots presented in this section demonstrate the abilities of the simulation models to predict time–dependent variables. This model is validated in Section 5.4 using the experiment results of the MC–OWC device.

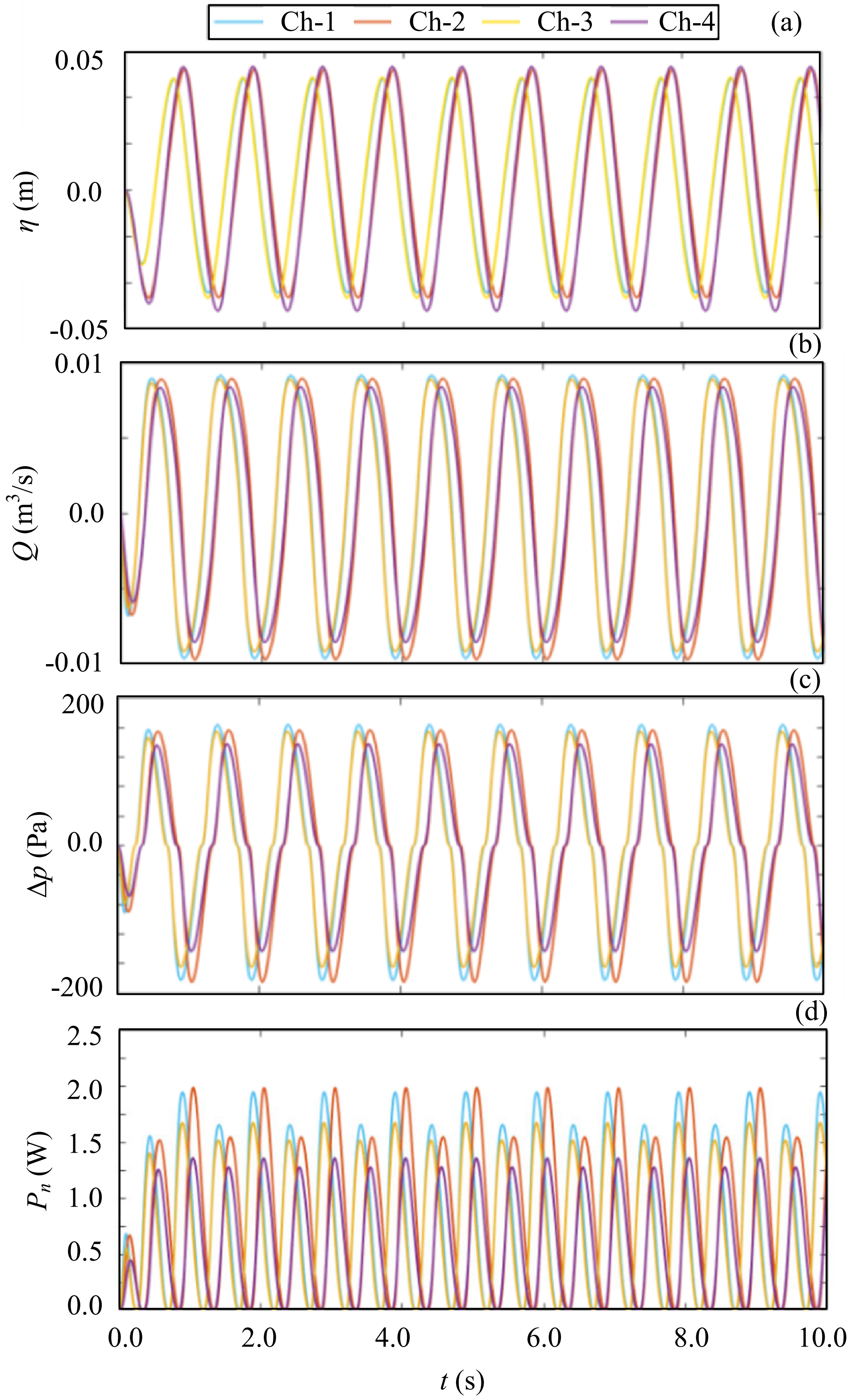

Figure 5.5. Sample of the temporal data of MATLAB/ Simulink for four chambers OWC device at H= 87 mm and T=1s for (a): water surface elevation inside chamber η, (b): airflow rate Q, (c): the differential pressure Δp, (d): pneumatic power P_n.

5.4 Validation of the Numerical Model

One of the objectives of this chapter is to validate the numerical model. This objective was achieved by comparing the numerical results of Δp, Q and η to a series of physical measurements obtained from the UTS wave flume which were previously discussed in Section 4.3 The MATLAB/Simulink model was executed on a sample–by–sample basis, with a sampling frequency of 10 Hz, which was selected to match the 10 Hz sampling frequency of the data acquisition system of the UTS wave flume. To start the model simulation, the wave conditions of the flume was given an initial condition to match the experimental data. The MATLAB/ Simulink model diagrams are presented in Appendix D.

Initially, consider Figure 5.6 (a). The time history of the water surface elevation inside the chamber $\eta(t)$ is presented to compare the numerical and the experiment results (the results of the first experimental test, Section 4.3) for wave conditions H = 87 mm, T = 1 s and orifice diameter D_1 = 36 mm. It is well known that the water surface profile and the pressure in the chamber are strongly related to the frequency of the incident waves [171].

For the case of period T = 1 s, the wavelength is equal to 1.5 m, which matches the total length of the physical model. Thus, each chamber works at a different wave phase which causes the internal free surface to be smoother and converge between the numerical and the experimental result as is apparent in Figure 5.6. Figure 5.7 presents the airflow rate Q at a constant value of orifice diameter (D = 36 mm). In Figure 5.8 the values of Δp that have been derived numerically using Eq.(5.24) and measured experimentally using a differential pressure transmitter are compared. Although a simplification was applied to the nonlinear term of the wave condition in the numerical model, the overall agreement between the numerical results and the experimental data is useful for the scaled model. This agreement was quantified via the Normalized Root Mean Square Error (NRMSE) for the pressure difference Δ*p,* the airflow rate through the orifice plate *Q*, and water surface elevation inside the chamber *η*. This is given by

$$\mathrm{NRMSE} = \frac{\sqrt{\frac{1}{N}\sum_{i=1}^{N}\left(x_i - y_i\right)^2}}{\left(X_{\max} - X_{\min}\right)} \tag{5.25}$$

where x_i is the experimental data, y_i is the corresponding MATLAB data, $x_{\max}$ and $x_{\min}$ are the maximum and minimum values of the experimental results, respectively. Overall, the NRMSE was found to be less than 16.5% for all the parameters tested, as illustrated in Table 5.2

Table 5.2 NRMSE of the MATLAB/Simulink.

Parameters	NRMSE (%)
Δp	12.9
Q	16.4
η	13.1

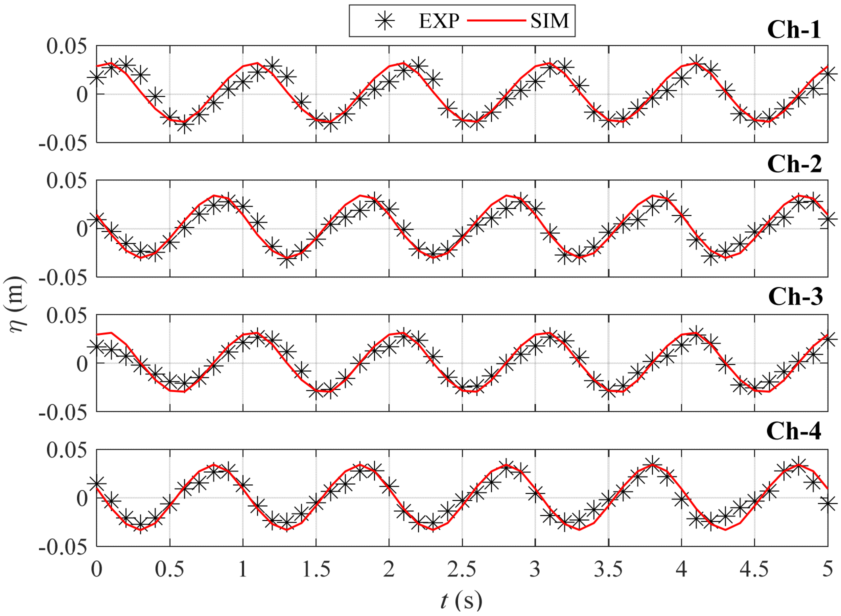

Figure 5.6. Comparisons between simulation and experimental values of the water surface elevation (*η*)

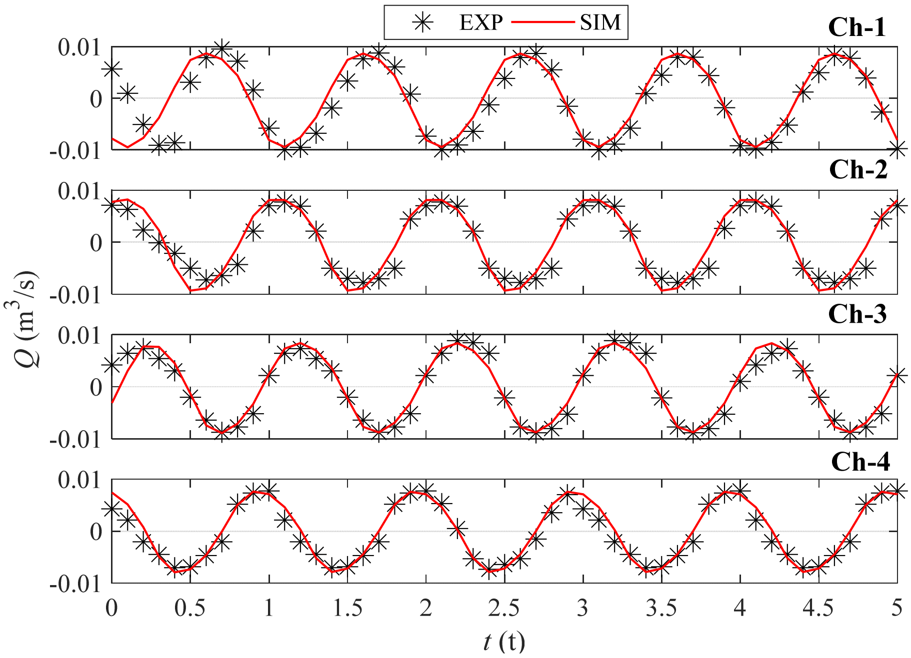

Figure 5.7. Comparisons between simulation and experimental values of the airflow rate through the orifice (Q)

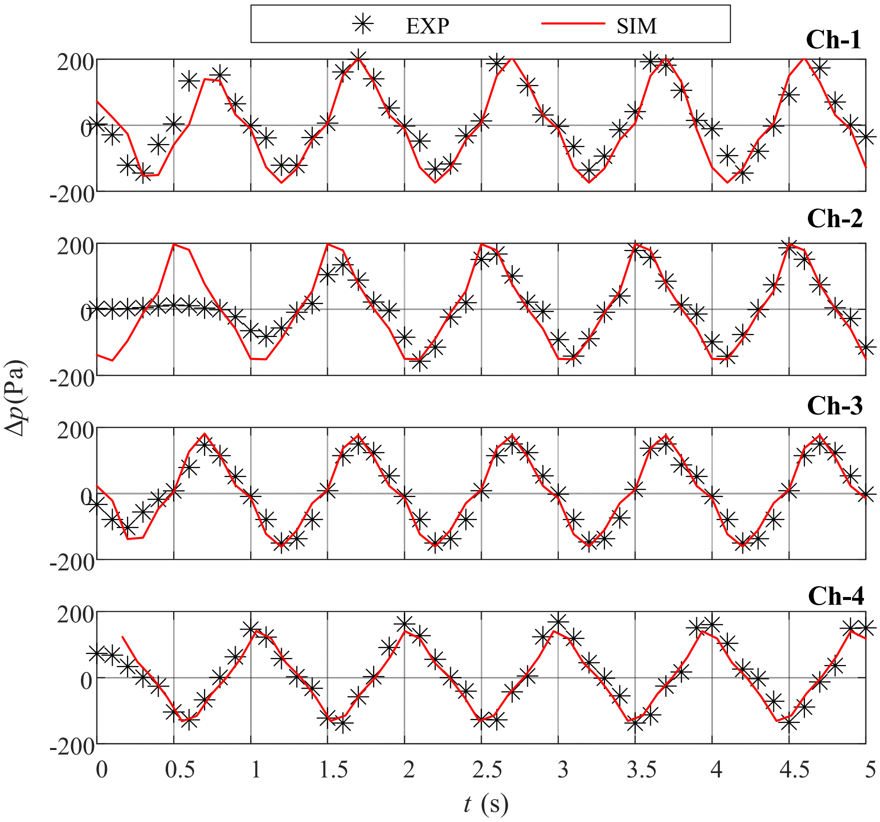

Figure 5.8. Comparisons between simulation and experimental values of the pressure difference (Δp)

5.5 Summary

In this chapter, the time–domain model successfully predicted the water surface elevation, airflow rate, differential air pressure and the pneumatic power of the MC–OWC device. This model was validated against a scale model experiments performed in a UTS wave flume, and a good agreement was found. The average Normalized Root Mean Square Error was 16.4% which is deemed acceptable. Consequently, the preliminary characterisation of the range of these variables was used in the setup of the second laboratory experiment (i.e. MHL tests).

In the approaches adopted in this chapter, the viscous damping term was tuned under one wave condition (i.e. H=87 mm, T=1s). Therefore, to improve the characteristics of this model, it required a wide range of experimental results to tune the viscous damping term. The recommendations have been made for further investigations on this subject.

This model utilised a linear wave theory, and hence, it cannot be used to handle problems that require capturing detailed physics such as strong nonlinearity, complex viscous effects, turbulence and vortex shedding. Thus, in the next chapter, a Computational Fluid Dynamic (CFD) method was deployed to allow consideration of complex nonlinearities that cannot be handled with the current model.

Chapter 6 : CFD MODELLING

6.1 Introduction

Computational Fluid Dynamics (CFD) is a numerical simulation tool that solves the fundamental Navier–Stokes (NS) fluid flow equations. The STAR–CCM+ commercial CFD code was employed in this work to solve the NS equations using the finite volume method over a specified domain. In STAR–CCM+, the Volume of Fluid (VOF) method was utilised to simulate and track the water–air interface. The main objective of this chapter was to develop an incompressible three–dimensional CFD model to simulate the MC–OWC device tested at UTS wave flume. In order to achieve this, a 3D numerical wave tank (NWT) was first developed. Then, the MC–OWC device was incorporated into the NWT and tests were conducted. For CFD validation, the numerical and experimental test results were compared. The validated CFD model was then used to carry out a numerical benchmark study of 84 tests, which were designed to investigate the effects of the pneumatic damping induced by the power take–off (PTO) system on a MC–OWC device performance. Lastly, the performance is assessed for a range of regular wave heights and periods.

6.2 Numerical Model

In the case of a Newtonian, incompressible and isothermal fluid, the set of governing equations for the fluid dynamics are the equation of conservation of mass Eq. (6.1) and conservation of momentum Eq. (6.2) which are often referred to as the Navier–Stokes equations (NS) [184].

$$\nabla . u = 0 \tag{6.1}$$

$$\frac{\partial(\nabla u)}{\partial t}+\nabla.(\rho\ u\ u)=\nabla p+\nabla.\Gamma+\nabla g+f \tag{6.2}$$

where u is the fluid velocity field, ρ is the fluid density, p is the pressure, Γ is the deviatoric viscous stress tensor, g is the acceleration due to gravity, f is the source of momentum due to surface tension, t is time and ∇ is the gradient operator.

The CFD models require accurate modelling and simulation of complex turbulent flows [185]. However, the number of required operations would exceed the maximum number of the most powerful computers that are currently available. Therefore, although a large number of studies have been performed on the development of turbulence models, there has not been a universal turbulence model that is applicable to all turbulent flows.

In this work, a Reynolds–Averaged Navier–Stokes equations (RANS) was utilized in the CFD model, in which the equations were discretised using a Finite Volume Method (FVM). RANS equations are based on the concept of Reynolds decomposition, the instantaneous velocity and pressure fields of Eq. (6.2) are decomposed into mean and fluctuating components, and the subsequent time–averaging of the set of equations. As a result, new terms called Reynolds stresses associated with the turbulent motion were introduced [186].

Several methods are being utilized to describe the air–water interface (free surface). The most common ones are the Volume–of–Fluid (VOF) method [187] that uses compression terms for the gravity (∇g) and surface tension effects (f) at the interface as shown in the right—hand side of Eq. (6.2) and described by Berberović et al. [188]. To solve these equations, a commercial code STAR–CCM+ has been chosen in this work due to the package availability.

6.2.1 Numerical Settings

In the CFD model developed in this chapter, the flow motion of the incompressible fluid was simulated by solutions of the Reynolds Averaged Navier–Stokes (RANS) equations. To enclose the equation systems, the Reynolds stresses were modelled using the two–equation Shear Stress Transport (SST) k–ω turbulence model. Ten prism layers with a stretching factor of 1.5 and a y–plus value of 1.0 were utilized to capture the boundary layer around OWC surfaces. These prisim layers are important to capture the boundary layer developed on OWC chambers non–slip walls. These layers consist of a constructed mesh with the distance from the first mesh line to the non–slip wall called "y–plus" in non–dimensional form. Figure 6.1 illustrates the boundary conditions and detailed mesh views of the CFD model used in this study. The NWT had an overall length of ten wavelengths (L) plus the length of the MC–OWC model. To reduce wave reflection from the outlet boundary assigned to the right side of the NWT, a distance of one wavelength was allocated to the damping zone in front of the pressure outlet boundary. Within this zone, the vertical velocity component was modified by adding a resistance term to dampen the waves before approaching the outlet boundary [189]. It is important to note that the absolute NWT length was not fixed for all the wave periods tested; instead, this length was adapted for each wave period to allow a total length of five wavelengths on the up–wave and down–wave sides of the MC–OWC device. This setup allows for collecting of a reasonable amount of data (about eight wave cycles) before waves reflected from the OWC and the outlet boundary interfere with the incoming waves [123]. The height of the NWT was one metre that was equally split between the air and water phases. Usually, fully 3D CFD simulations are very expensive; therefore, it is beneficial to use symmetry planes when applicable. Using a vertically–longitudinal symmetry plane in OWC devices was proved to have a negligible impact on device performance [190]. As a result, only half–width of the physical wave flume (0.45 m) was modelled in the NWT of this study with a symmetry plane as shown in Figure 6.1 (a). Since the ratio between the OWC breadth to the NWT width was 0.167 (i.e., < 0.2), the tank sidewall effects were expected to be nil as stated by Chakrabarti [162]. Regular wave velocity components were provided to the NWT on the left side through on the inlet boundary, whereas the top outlet boundary had a hydrostatic wave pressure assigned to it and the tank side and bottom boundaries were defined as slip walls. The free surface zone height was set to 1.5H (H is wave height).This was found to be sufficient and reduced the computation cost while still capturing the waves reflected by the OWC and minimizing unwanted numerical wave height damping within the area of interest [190]. This height was further increased to 2H inside each chamber (see Figure 6.1 (c)) to capture any free surface amplification.

The computational domain mesh is crucial for confidence in the CFD results. STAR–CCM+ offers a user–friendly automatic meshing technique that was used in this study. The whole domain was initially meshed using a cell size of 400 mm and then reduced with more refinements using a trimmed cell mesher and a surface remesher. For the free surface refinement, the minimum number of cells that was used in the z–direction was 16 cells per wave height and in the x–direction was 74 cells per wavelength. These settings are very close to the recommendations given by ITTC [191] and CD–Adapco [192]. The cell aspect ratio (i.e., the ratio between the cell size in the longitudinal (Δx) and vertical (Δz) directions) was not allowed to exceed 16 [99]. Elhanafi et al. [190] recommended that the cell size in the y–direction (tank traverse) was set to Δy = 100 mm. The mesh refinement for the MC–OWC model was done following the mesh convergence study carried out by Elhanafi et al. [137] for a two–chamber 3D OWC. An OWC cell size of 6.25 mm was used (see Figure 6.1 (d)) and the PTO surface was refined using a cell size of 0.781 mm (see Figure 6.1 (e)). It is worth mentioning that these settings have previously provided a good agreement with experiments for an OWC device with one chamber [169, 172, 173]. The time–step (Δt) for each wave period (T) was carefully selected as recommended by CD–Adapco [53] to ensure the Courant number was always less than 0.5.

(a): 3D computational domain (not to scale) and boundary conditions

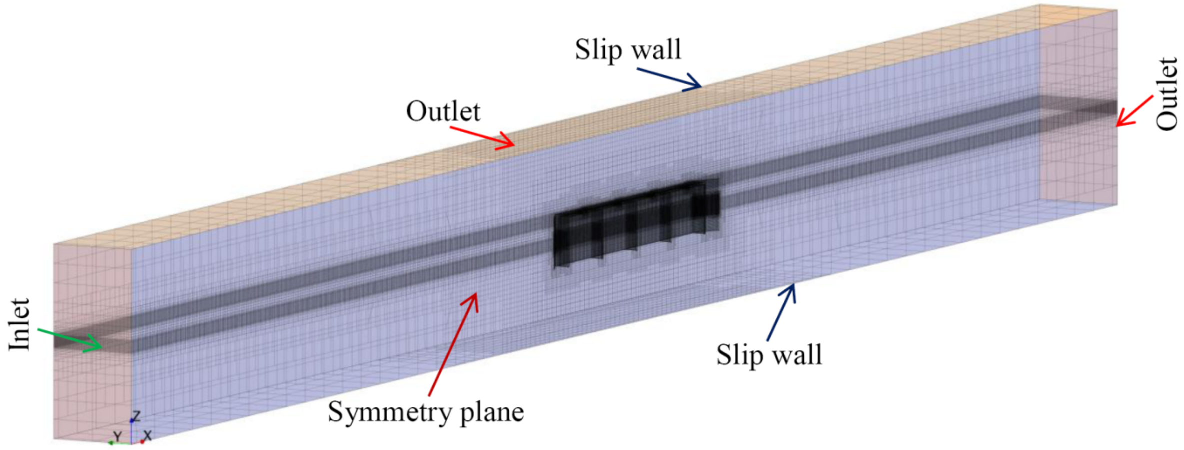

(b): Zoom-in of 3D MC-OWC device **(c): Zoom-in of free surface refinement**

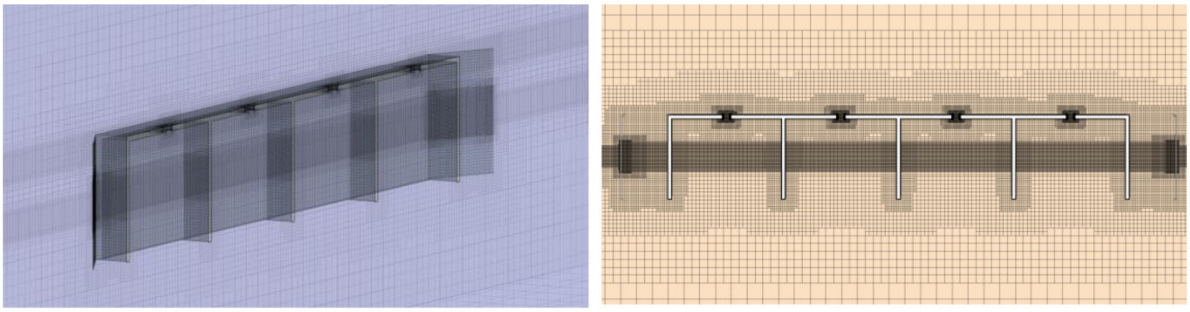

(d): Zoom-in of MC-OWC device refinement **(e): Zoom-in of orifice refinement**

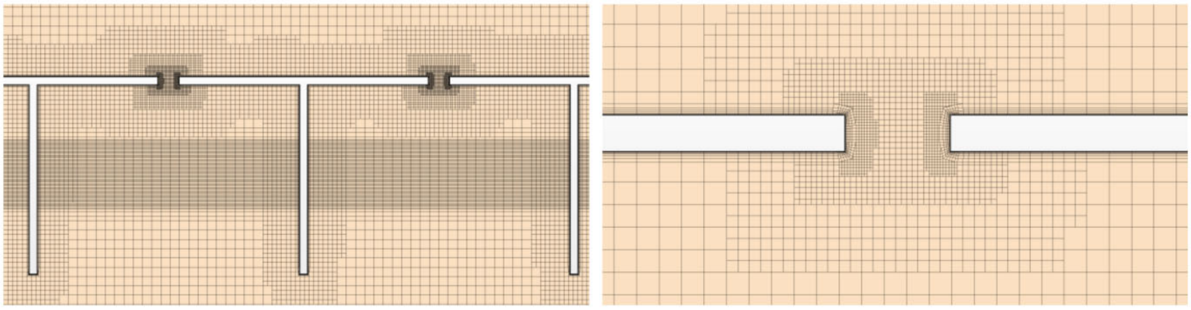

Figure 6.1. Computational fluid domains.

6.3 MC–OWC Device Performance

The differential air pressure (Δp) was numerically monitored in each chamber by air pressure measurements at two points: the first was inside the chamber and the second was on the top outlet boundary domain. The airflow rate (Q) was directly monitored by integrating the vertical air velocity over the entire area of the orifice. In each chamber, the free surface elevation (η) was measured using a virtual wave probe installed in a similar location to the physical model.

6.4 Validation of the CFD model

One of the aims of this chapter is to experimentally validate the CFD model of a complex hydrodynamic problem involving wave and MC–OWC interactions. Only one regular wave of height H = 87 mm and period T = 1.0 s was used to validate the CFD model for the following performance parameters: η, Q and Δp with a constant PTO damping simulated with an orifice diameter D_2 = 36 mm (R = 1.9 %). The CFD and experimental time history results are compared in Figure 6.2. It can be seen that the CFD results show good correlation with the experimental data. This agreement was quantified via the average correlation coefficient R and the Normalized Root Mean Square Error (NRMSE) given by Eq. (5.25).

The average NRMSE and correlation coefficient R for all the validated parameters (η, Q, Δp) were found to be about 10 % and 0.89, respectively, as summarized in Table 6.1.

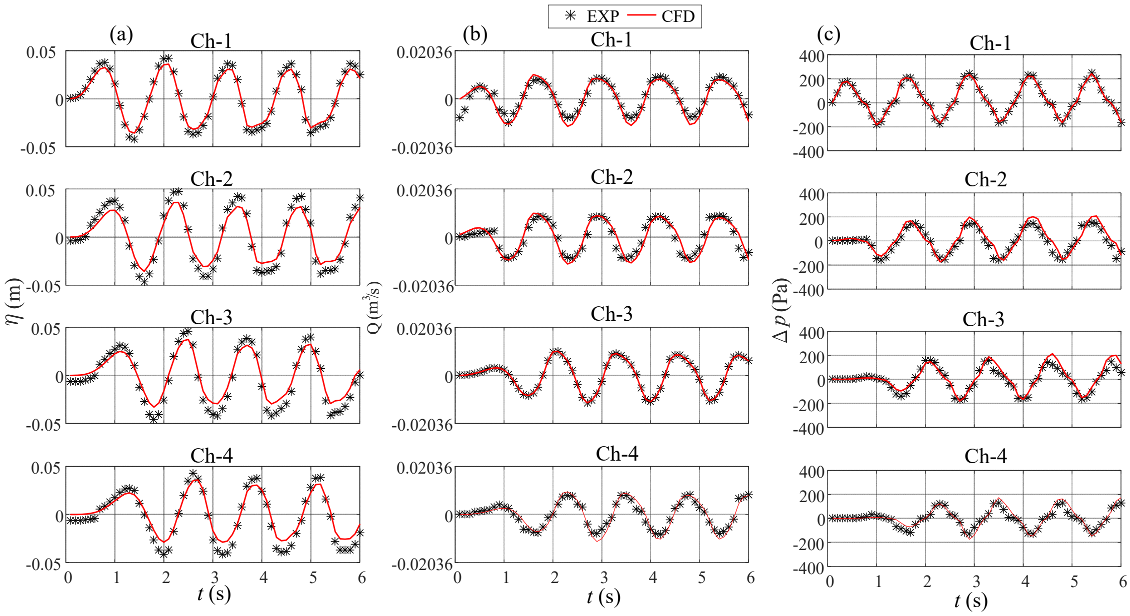

Figure 6.2. Comparison experimental and CFD results for device performance parameters under a regular wave of height $H = 87$ mm, period $T = 1.0$ s and orifice diameter $D_2 = 36$ mm. (a): water surface elevation (η), (b): airflow rate (Q) and (c): differential air pressure (Δp)

Table 6.1. The correlation coefficient R and NRMSE between the CFD and the experimental results for water surface elevation (η), airflow rate (Q) and differential air pressure (Δp)

Parameters		Ch–1	Ch–2	Ch–3	Ch–4	Average
η	NRMSE (%)	10.48	11.37	11.69	11.54	10.00
	R	0.97	0.86	0.85	0.86	0.89
Q	NRMSE (%)	10.05	12.03	0.61	7.87	7.64
	R	0.90	0.86	0.91	0.93	0.90
Δp	NRMSE (%)	1.83	11.51	9.05	8.70	7.77
	R	0.99	0.83	0.88	0.87	0.89

The good agreement achieved indicated the capability of the CFD model in simulating the behaviour of the MC–OWC device considered in this study. Therefore, the CFD model was utilized, as will be discussed in the following sections, to test the performance of the device under different wave conditions and various PTO damping coefficients.

6.5 Results and Discussion

6.5.1 Test Conditions

After the numerical model was verified, a second set of tests was performed to study the effect of PTO damping on the performance of the MC–OWC. The validated CFD model was used to carry out numerous numerical simulations. In all, 84 simulations were carried out which comprised of six different PTO damping values simulated with different orifice diameters as summarised in Table 6.2. Each orifice was defined by its diameter (D_i) and the opening ratio (R_i). The opining ratio is the ratio between the orifice area and the chamber waterplane area (L_c x b) in percentage, %. Tests were performed for two wave heights H = 45 mm (H1) and 87 mm (H2) over the eight wave periods summarized in Table 6.3.

Table 6.2. Orifice diameter and its opening ratio

D (mm)	17	24	29.5	34	38	41.7
R_i (%)	$R_1 = 0.5$	$R_2 = 1.0$	$R_3 = 1.5$	$R_4 = 2.0$	$R_5 = 2.5$	$R_6 = 3.0$

Table 6.3. The wave period values used in CFD

T (s)	0.8	1.0	1.12	1.2	1.3	1.6	1.8	2.0
Ti	T0	T1	T2	T3	T4	T5	T6	T7

6.5.2 Estimating Device Resonance

The resonant angular frequency ($\omega = 2\pi/T_\mathrm{R}$) of an OWC device can approximately be estimated from Eq. (3.32). For the device tested in UTS wave flume (see Section 4.3) that was used in CFD validation in this Chapter, the estimated angular frequency was found to be $\omega = 6.67$ rad/s (the resonant period $T_\mathrm{R} \cong 0.94$ s). It is worth noting that this equation does not account for the penumatic damping induced by the PTO system as addresed in Section 3.6.

6.5.3 Effect of PTO Damping on Device Performance

In this section, the CFD model was utilised to verify the validity of the quadratic relationship in Eq. (3.27) under a constant wave height H2 (0.087 m). It can be seen in Figure 6.3 for a wave period T2 (1.12 s) that the relationship between Q and Δp follows a simple parabolic curve (the fitting curves are not shown in this figure) with a correlation coefficient R of not less than 0.9. Additionally, the damping coefficient (τ) in all chambers was quite similar and found to be in the range of $\tau_{\min} = 1036$ kg$^{1/2}$ m$^{-7/2}$ at R_6 to $\tau_{\max} = 5200$ kg$^{1/2}$ m$^{-7/2}$ at R_1.

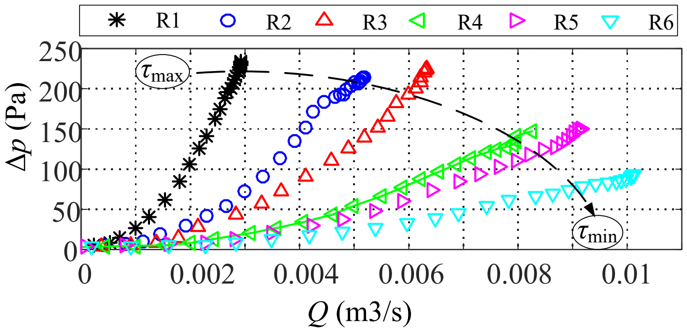

Figure 6.3. The relation between the air volume velocity (Q) and the instantaneous differential air pressure (Δp) for different PTO damping conditions simulated via various orifice opening ratios R_i (listed in Table 6.3)

The impact of the pneumatic damping on Q, Δp and η is illustrated in Figure 6.4 at a constant wave condition (H2, T1). Starting with the impact of the pneumatic damping coefficient (τ) on the water surface elevation (η), Figure 6.4 (a) shows that η decreased from more than 0.04 m to just above 0.01 m as τ increases from 1036 to 5200 kg$^{1/2}$ m$^{-7/2}$. Furthermore, the first chamber (Ch–1) and the last chamber (Ch–4) experienced the highest and lowest free surface oscillations, respectively. Since the airflow rate (Q) is related to the free surface vertical velocity V_z (assuming incompressible flow), which can be calculated as the rate of change in the free surface elevation (η) with respect to time (i.e., $V_z = d\eta/dt$), it was expected that the airflow rate follows the changes in η

inside the chamber. This is shown in the results presented in Figure 6.4 (b) where it is clear that Q in all chambers had the same trend of η with maximum and minimum values of about 0.01 and 0.0025 m^3/s. These observations are in line with the results reported in [99, 140, 144] for a single chamber OWC device. With the relationship between Δp and Q shown in Figure 6.3, Δp is seen in Figure 6.4 (c) to gradually be increased from a minimum of 130 Pa to a maximum of 214 Pa with increasing damping coefficient. The penumatic power ($\overline{P}_n$) is always influenced by both Δp and Q; hence, the results in Figure 6.4 (d) illustrate that there was a certain damping range of 1326 to 1500 $kg^{1/2}\ m^{-7/2}$ over which $\overline{P}_n$ peaked. The maximum pneumatic power was also found to decrease from 0.67 W in Ch–1 to 0.5 W in Ch–4.

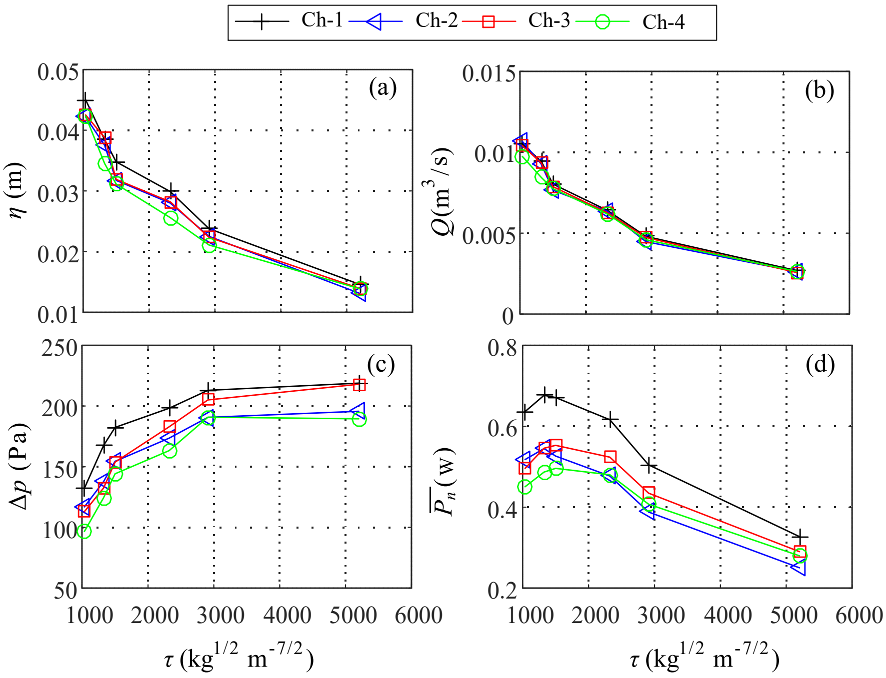

Figure 6.4. Impact of PTO damping coefficient (τ) on the values of (a): the instantaneous water surface elevation inside chamber (η), (b): the airflow rate (Q), (c): differential air pressure (Δp) and (d): the pneumatic power ($\overline{P}_n$)

One of the most important characteristics of a WEC device is the capture width ratio (ε). The influence of the pneumatic damping on ε for each chamber of the MC–OWC model is shown in Figure 6.5 for different wave periods (listed in Table 6.3). The results in this figure show a resonant period of 1.0 s (T1), which is very close to what was estimated from Eq. (3.32). For all chambers, the capture width ratio had optimum value at a damping value corresponding to R_5, especially for wave periods shorter than T2. The importance of the PTO damping in tuning the device to the incident wave condition is obvious for all chambers over the intermediate wave period range (T2–T6), where a lower PTO damping of orifice R_3 provided a higher capture width ratio. The reduced damping of R_1 could further improve the capture width ratio at the longest wave period tested.

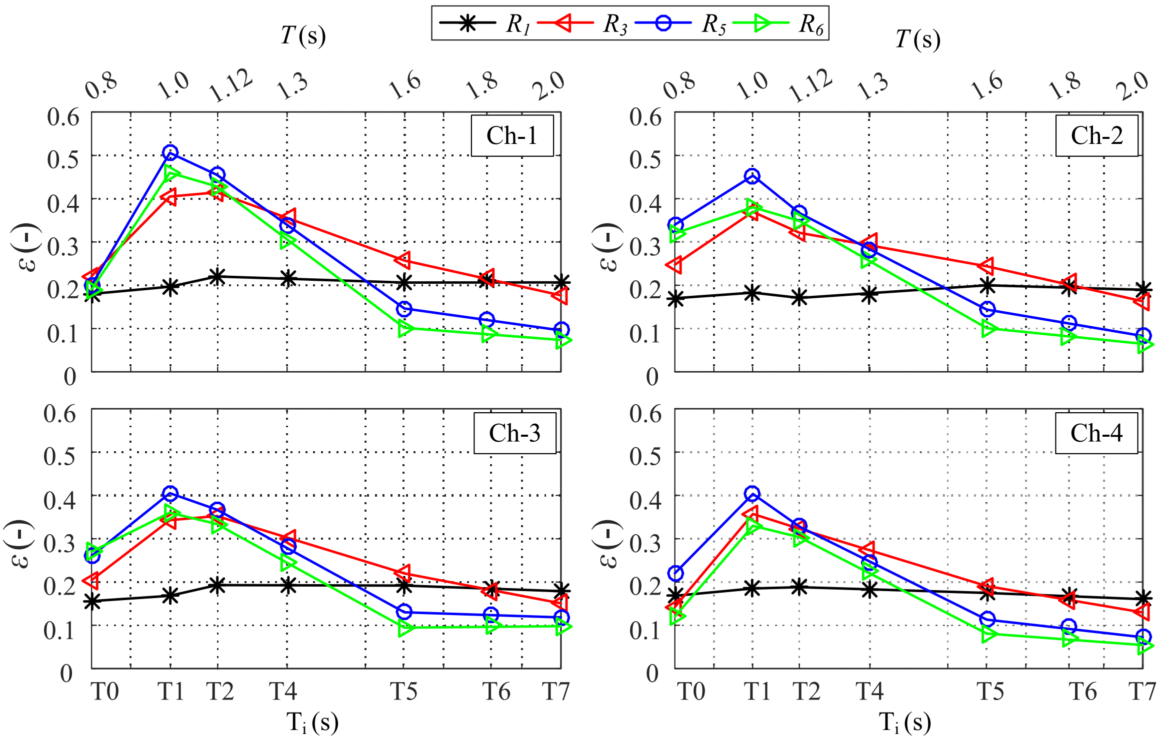

Figure 6.5. Effect of PTO damping on the capture width ratio (ε) of each chamber for different wave periods and a constant wave height (H2 = 87 mm)

6.5.4 Effect of Wave Height on Device Performance

The influence of the incident wave height on device performance is investigated in this section. This was done by decreasing the wave height to 45 mm (H1). Figure 6.6 demonstrates the effect of the wave height has on the chamber water surface elevation

(η), the airflow rate (Q), the differential air pressure (Δp) and the pneumatic power ($\overline{P}_n$) for a range of wave periods with PTO damping of an orifice opening ratio R_5 (2.5 %). Both wave heights have shown almost identical general trends for all the parameters assessed. They decreased as wave height decreased from H2 to H1. The increase in wave height was almost 1.93 times (i.e., from 45 mm to 87 mm) indicating that the incident wave power increased by about 3.74 times. However, the pneumatic power in all chamber increased on average by 3.56 times. This difference could be attributed to the slight increase and decrease in the reflected and transmitted energies respectively by the device resulting in a reduction in energy absorbed by the device [172].

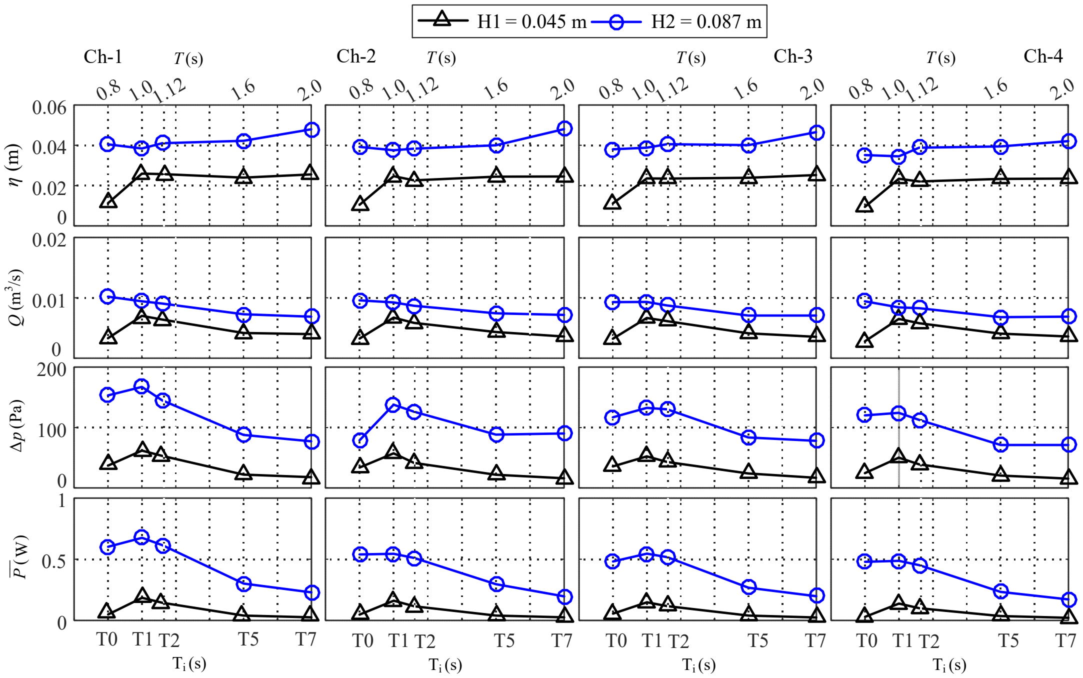

Figure 6.6. Effect of wave height on the water surface elevation η (1st row), airflow rate Q (2nd row), differential air pressure Δp (3rd row) and the pneumatic power $\overline{P}_n$ (4th row) for different wave periods and a constant orifice opening ratio R_5 (2.5%)

Figure 6.7 illustrates the impact the wave height has on ε_c for each chamber at a constant orifice opening ratio (R_5 = 2.5 %). The results demonstrate that all chambers had similar trends for ε_c under the two wave heights tested, such that ε_c initially increased with increasing wave period until a peak value was reached at the resonant period (T1). Then it reduced with a further increase in wave period. Under the wave height H1 at T1, ε_c reached a maximum value of 0.58, 0.50, 0.46 and 0.43 for Ch–1, Ch–2, Ch–3 and Ch–4, respectively. These peak values were reduced to 0.50, 0.45, 0.41 and 0.40 when the wave height was increased to H2. A similar effect of wave height on single–chamber onshore and offshore OWC devices was previously reported [142, 144, 169, 173].

It is expected that with increasing the incident wave height, not only the pneumatic power (see Figure 6.6) increases but also the energy losses [172]. Furthermore, as mentioned earlier, changing the wave height affects the reflected and transmitted wave energies, which, in turn changes the amount of energy absorbed by the device structure. Elhanafi et al. [172] observed that the absorbed energy coefficient (i.e., the ratio between the absorbed energy and the incident wave energy) of an OWC device decreased with increasing the wave height, except for long wave periods where there was a noticeable increase in the absorbed energy coefficient. These observations help understand the increase in ε_c shown in Figure 6.7 only for wave periods longer than the resonant period.

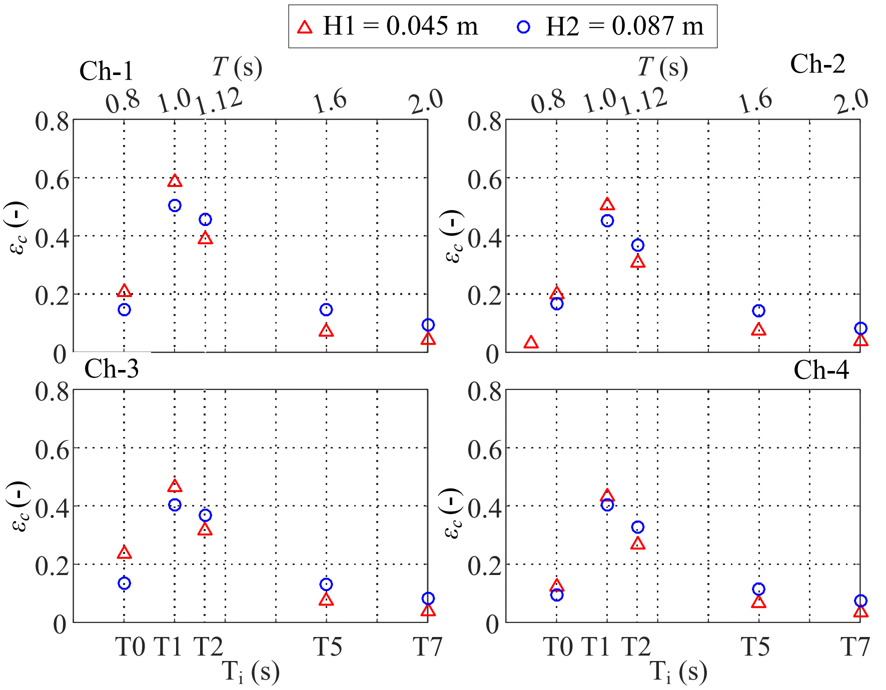

Figure 6.7. Variation of the capture width ratio (ε_c) of each chamber under different wave heights (H1, H2), wave periods (T0, T1, T2, T5, T7) and a constant orifice opening ratio (R_5 = 2.5 %)

Similarly, ε which is the overall capture width ratio for the MC–OWC device ($\sum_{i=1}^{i=4} P_i/(b \times P_{in})$), shown in Figure 6.8 (a) achieved a maximum value of ε = 2.0 at the resonant period T1 (1.0 s) and H = 45 mm (H1). This value was reduced to ε = 1.8 as the wave height increased to 87 mm (H2) at the same resonant period. Overall, increasing the wave height from H1 to H2 improved ε by 1.2 to 2.2 times in the long–period range (Ti > T2), but it negatively impacted device performance in the short–period range (Ti < T2) resulting in a reduction of ε by 0.70 to 0.90 times. The effect of wave height on the PTO damping is shown in Figure 6.8 (b) at the device resonant period T1. It can be seen that for all the tested PTO damping values, an increase in incident wave height reduced the maximum value of ε. The larger wave height H2 required a slightly larger orifice opening ratio (i.e., smaller PTO damping coefficient of τ = 1036 kg$^{1/2}$ m$^{-7/2}$ at R_6 instead of τ = 1326 kg$^{1/2}$ m$^{-7/2}$ at R_5). It is worth noting that these effects are in line with the experimental results reported in [169], which further support the applicability of the developed CFD model in studying the performance of such a complex MC–OWC device.

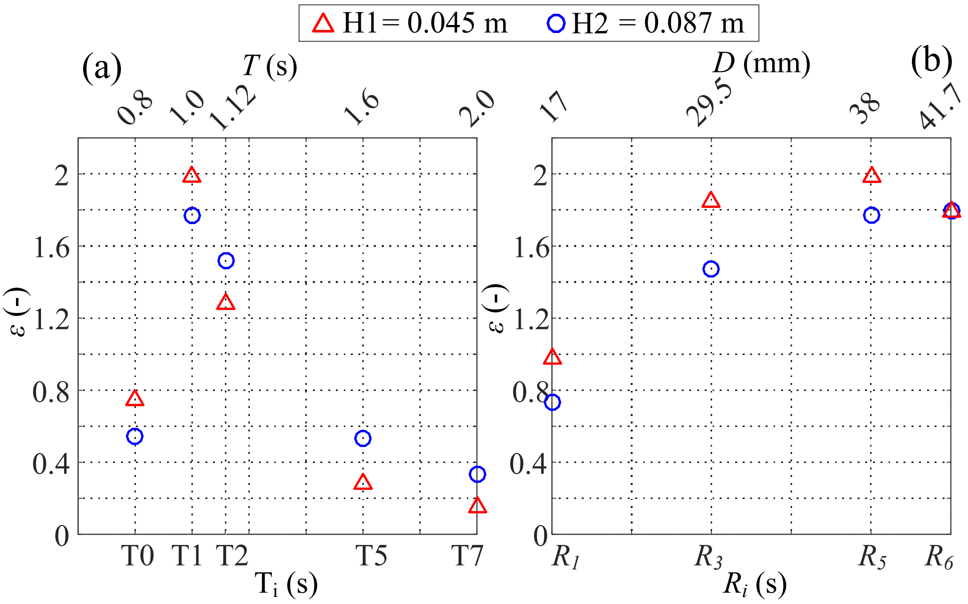

Figure 6.8. Effect of wave height on the total capture width ratio (ε) for (a): different wave periods at constant opening ratio R_5, (b): different orifice opening ratios (R_i) under resonant period T1

6.6 Summary

A 3D CFD model was developed to simulate the behaviour of a MC–OWC device and to investigate the effect of PTO damping and wave height on device performance for a range of wave periods. The CFD results showed good agreement with the experimental measurements in all chambers for the following parameters: differential air pressure, chamber water surface elevation and airflow rate. Also, the resonant period agreed very well with the value estimated from a commonly used formula.

It was found that increasing the PTO damping resulted in increasing the differential air pressure but lowering the water surface elevation and the airflow rate in all device chambers over the entire range of wave periods tested. Among the six PTO damping values tested in this study, the intermediate PTO damping (τ =1326 kg$^{1/2}$m$^{-7/2}$) was found to maximize ε for all chambers over all wave periods, except for long waves where a higher PTO damping was found to be more effective.

Increasing the wave height from 45 mm to 87 mm (i.e., 1.93 times) was found to significantly decrease the MC–OWC device total capture width ratio (ε) for all PTO damping values tested by about 20 % in the short–period wave range, but ε showed an increase of about 76 % over the intermediate– and long–period wave ranges. The impact of changing the incident wave height on the resonant period was found to be negligible, but a larger wave height required slightly lower PTO damping.

Chapter 7 : CONCLUSIONS AND RECOMMENDATIONS FOR FUTURE WORK

This chapter summarises the major outcomes achieved from the research conducted in this thesis along with a number of recommendations for important aspects to be considered for future studies.

7.1 Overall Conclusion

The research work presented in this thesis was devoted to a study of a MC–OWC wave energy converter device that is composed of four fixed rectangular OWC chambers. This device was considered as a direct complement of the development of MC–OWC devices, towards the full scale deployment.

The present work was designed to investigate the impact of the following aspects on the device performance: 1) wave period and wave height for regular and irregular wave conditions, 2) device draught, and 3) Power Take–Off (PTO) damping. The research utilised the two most common and powerful approaches: 1) physical scale model experiments that were conducted in two different wave flumes for two models of different scale (Chapters 4), and 2) numerical modelling using a time–domain model implemented in MATLAB/Simulink environment (Chapter 5) and a fully nonlinear 3D CFD model developed using Star–CCM+ code (Chapter 6).

The following main conclusions were drawn from the studies performed in this thesis:

[1] The proposed device allowed the incident waves to pass not only underneath the OWC chamber but also around the model sidewalls. Therefore, the maximum

capture width ratio obtained was 2.1 under regular wave conditions and 0.95 under irregular wave conditions. These values were the highest among all similar concepts that have been reported in previous research. This improvement in the capture width ratio is deserving of further investigation.

[2] All device chambers showed a similar response to the wave conditions, device draught and PTO damping.

[3] Among the four OWC chambers, the first chamber (Ch–1) always played the primary role in wave energy extraction, and the performance gradually decreased down to the fourth chamber (Ch–4) where the lowest performance was found. However, Ch–2, Ch–3 and Ch–4 contributed about 43 % of the device total maximum capture width ratio (i.e. 2.1).

[4] Increasing the incident wave height resulted in accumulating additional differential air pressure, airflow rate and water surface elevation in all chambers. However, the wave height had an inconsistent effect on the device capture width ratio for a given period regime. For instance, the capture width ratio (ε) improved about 1.1 to 1.3 times as wave height increased in the long–wave period regime, but the larger wave height negatively impacted the device performance in the short–wave period regime resulting in a reduction in ε to 0.70–0.90 times.

[5] Changing the device draught altered the mass of the water column inside the OWC chamber, which in turn changed its resonant period such that the peak capture width ratio (ε) values were shifted to a shorter wave period as the draught decreased.

[6] The chamber draught had a lesser influence on the capture width ratio values in the long wave period regime than in the short wave period regime. Among the

three draught values examined, a draught of 250 mm provided a slightly higher peak capture width ratio of 2.1 compared to 1.8 for the other draught values.

[7] The PTO damping showed a crucial effect on all the performance parameters tested in this work. The experimental and numerical results showed that increasing the PTO damping resulted in a higher chamber differential air pressure, a lower airflow rate and a smaller chamber free surface elevation.

[8] There was a specific value of the PTO damping at which the maximum capture width ratio was achieved for a given period. In this work, an intermediate PTO damping (τ = 463.7 kg$^{1/2}$ m$^{-7/2}$) was found to improve the device capture width ratio for the entire wave period range tested, but a larger PTO damping (τ = 1854.6 kg$^{1/2}$m$^{-7/2}$) was more beneficial for the large–wave period regime, especially for the smaller wave height tested of H = 50 mm.

[9] The experimental and numerical results showed that the resonant period conformed with the value estimated from a commonly used formula.

[10] In the experimental tests performed in the MHL wave flume, an excellent experimental repeatability was achieved, and all measurement uncertainties were in the order of ± 6% giving a level of confidence of approximately 95%.

[11] The time–domain model was successfully applied to get a preliminary understanding of device performance.

[12] The 3D CFD model developed in this study was proven to be capable of replicating the physical experiments and performing a detailed study of the hydrodynamics and aerodynamics of the MC–OWC device.

[13] The good agreement between the numerical and experimental results was quantified using the Normalized Root Mean Square Error (NRMSE) that was

found to be less than 16.5 % for the time domain model and 10 % for a 3D CFD model.

7.2 Recommendations for Future Work

Any proposed WEC technology requires continuous research and development work at both theoretical and application levels to steadily improve the performance and establish the competitiveness in the global energy market. Therefore, this work covered several design difficulties that had not been conducted in previous research work done on the two– or three–chambers OWC devices.

As with all research, specific questions arise which are outside the scope of the current project. Throughout the course of this work, further improvements arose which would be interesting for future studies to progress the development stage of the MC–OWC device. These points are listed below:

[1] Perform further experimental and numerical modelling studies to: 1) carry out an energy balance analysis for a MC–OWC device and; 2) improve the device capture width ratio by optimising the device underwater geometry; 3) investigate the effect of the wave direction relative to device orientation on device performance; 4) investigate the effect of each chamber length and draught on device performance.

[2] The proposed device was designed to use four separate turbines, one for each chamber. This in turn increases the cost of the device. Therefore, further studies where multiple chambers share the same turbine are crucial along with a feasibility study to draw an overall conclusion on the cost–effectiveness of the

MC–OWC system and its applicability for integrating this system into breakwaters.

Appendix A : Experiments Photos

Figure A.1. Front view of MC–OWC device in UTS wave flume

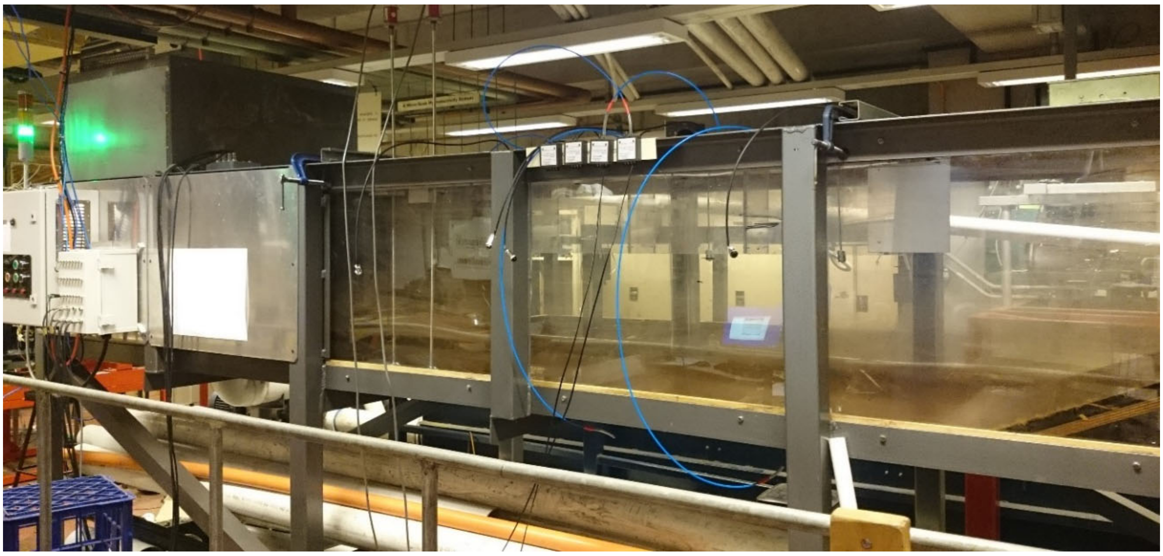

Figure A.2. Front view of the UTS wave flume

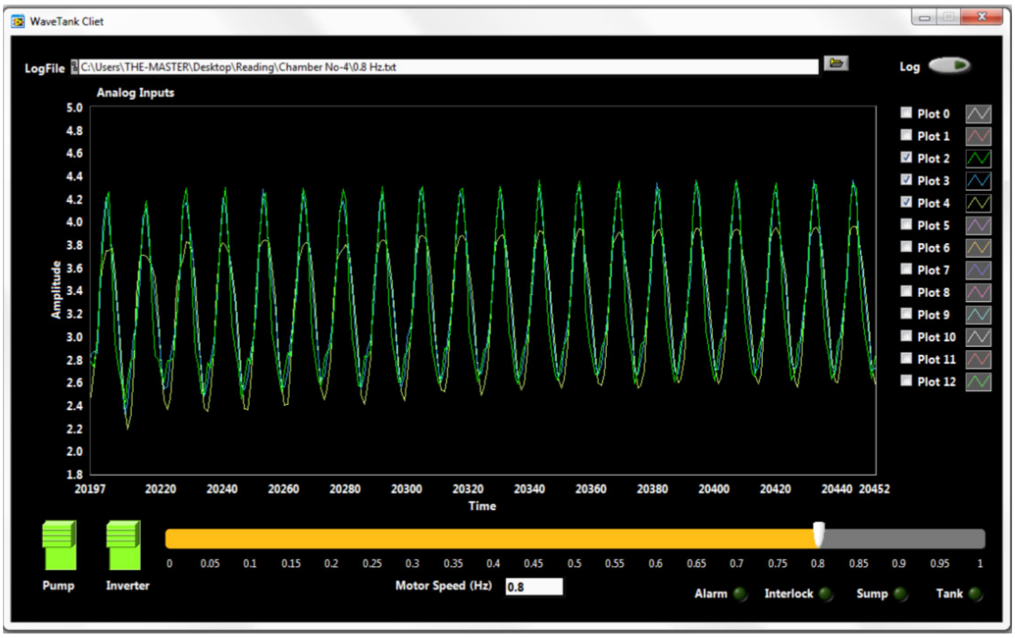

LogFile C:\Users\THE-MASTER\Desktop\Reading\Chamber No-4\0.8 Hz.txt

Motor Speed (Hz) 0.8

☐ Plot 0
☐ Plot 1
☑ Plot 2
☑ Plot 3
☑ Plot 4
☐ Plot 5
☐ Plot 6
☐ Plot 7
☐ Plot 8
☐ Plot 9
☐ Plot 10
☐ Plot 11
☐ Plot 12

Figure A.3. Data acquisition in the UTS wave flume during the experiment

Figure A.4. Wave moving towards the test area in MHL wave flume

Figure A.5. MHL wavemaker system

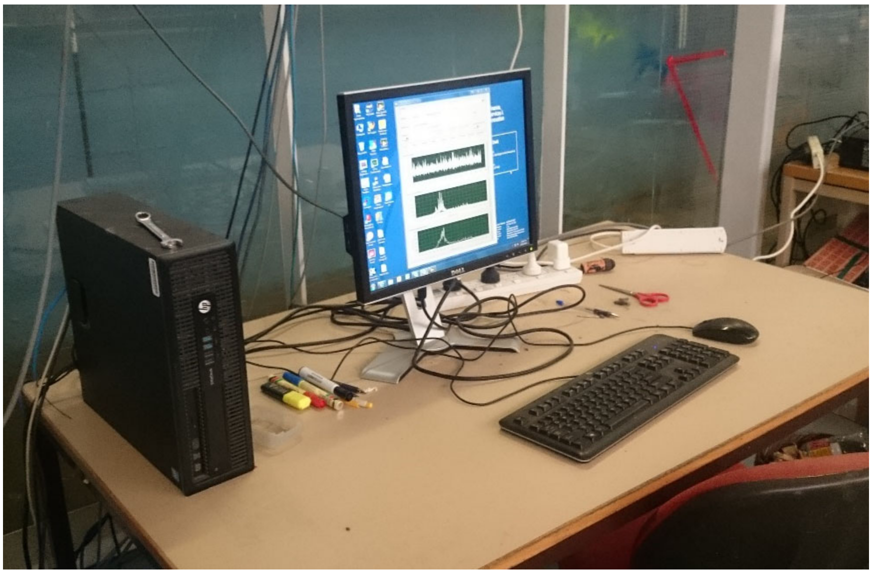

Figure A.6. Wave generation and data acquisition system

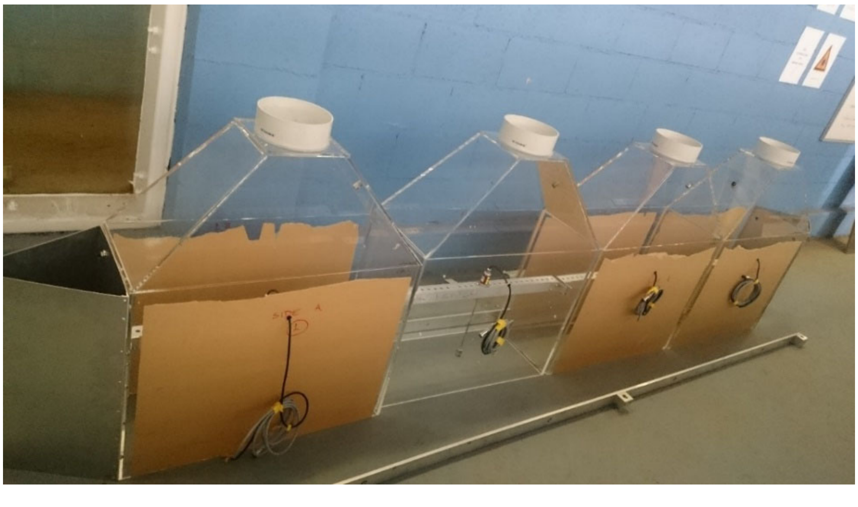

Figure A.7. The MC–OWC model during installation stage.

Appendix B : Irregular Wave Test

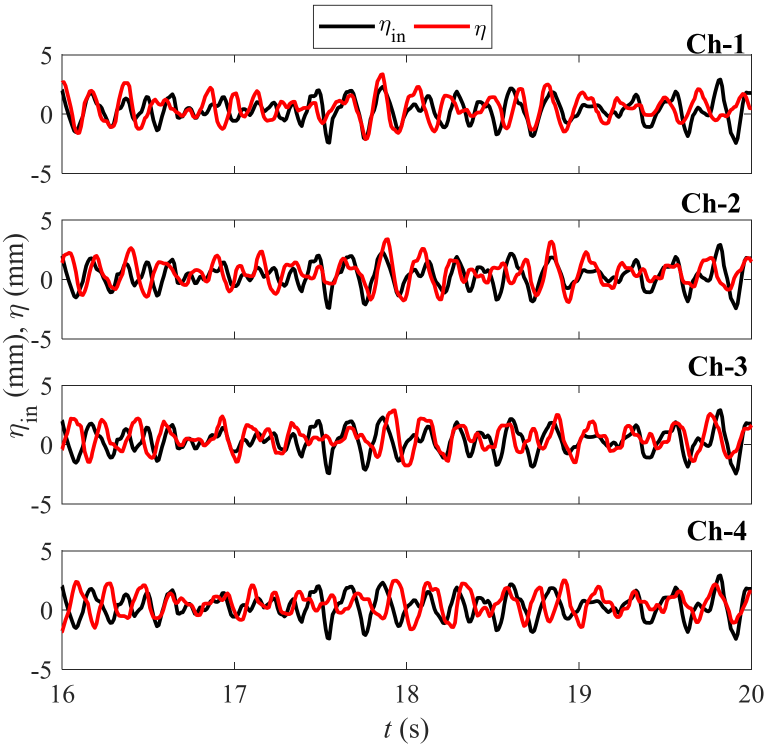

Figure B.8. Sample time–series data of the internal water surface elevation η and incident wave η_{in} in each chamber for a wave condition of Test–1 and constant opening ratio of R_2 =1.35%.

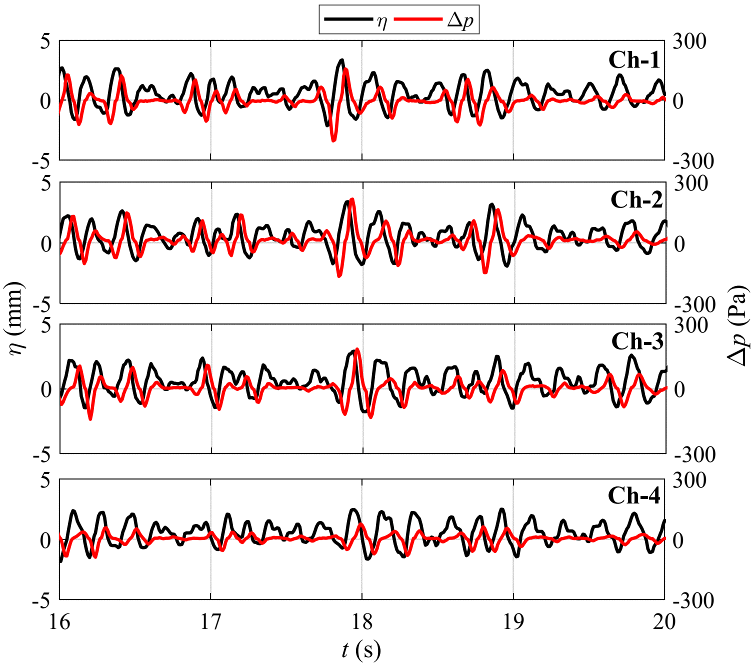

Figure B.9. Sample time–series data of the internal water surface elevation η and differential air pressure Δp in each chamber for a wave condition of Test–1 and constant opening ratio of R_2 =1.35%.

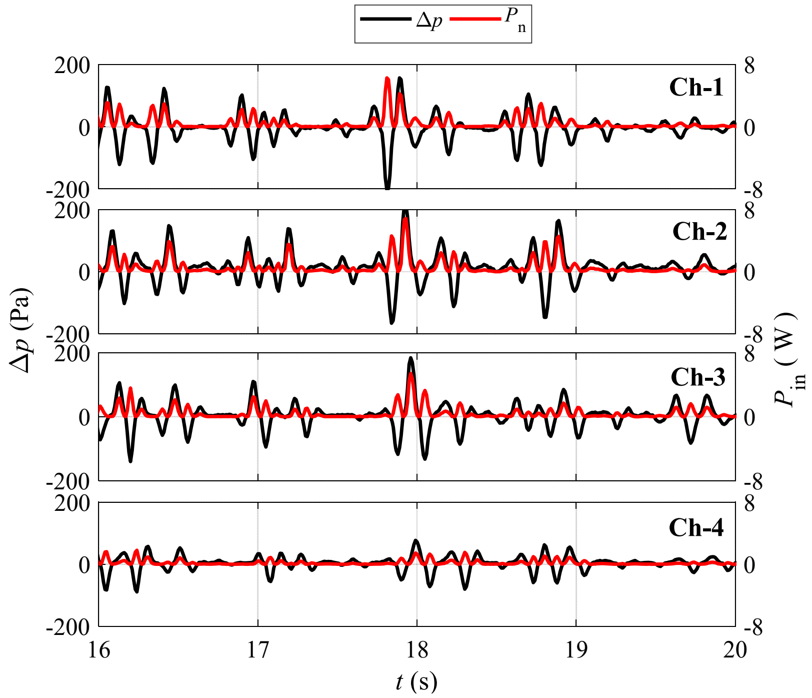

Figure B.10. Sample time–series data of the differential air pressure Δp and pneumatic power P_n in each chamber for a wave condition of Test–1 and constant opening ratio of R_2 =1.35%.

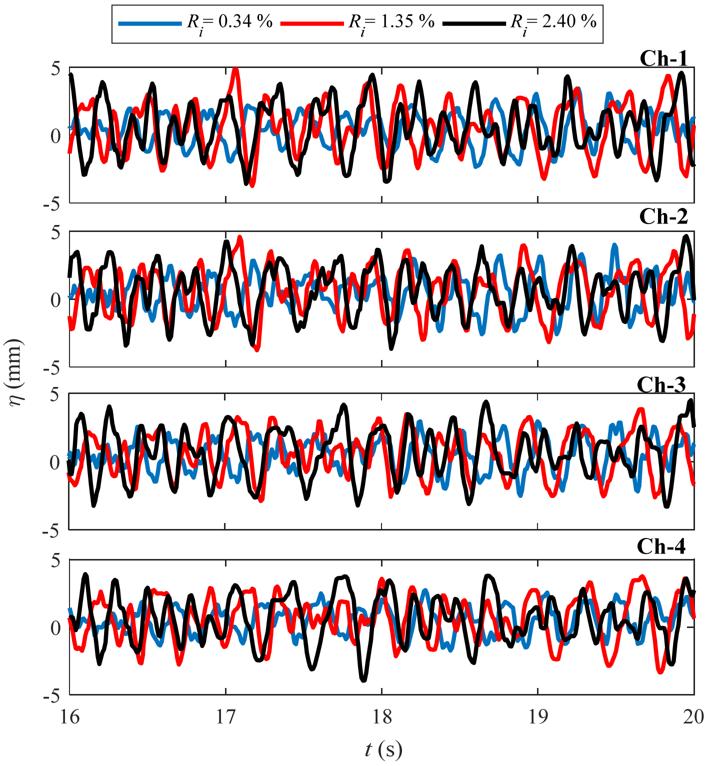

Figure B.11. Sample time–series data of the effect of PTO damping on the internal water surface elevation η in each chamber for a wave condition of Test–1 and three values of opening ratio.

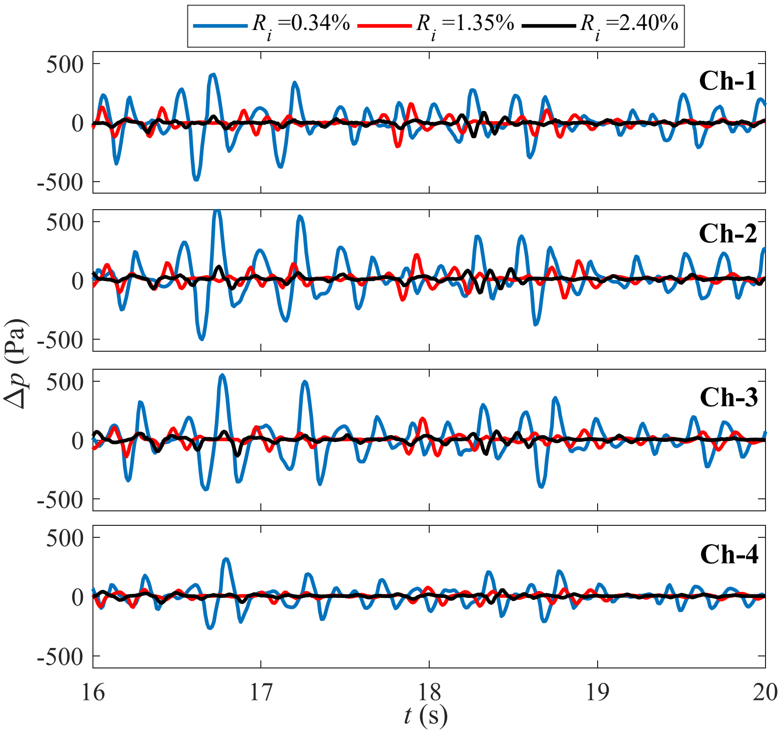

Figure B.12. Sample time–series data of the effect of PTO damping on the differential air pressure Δp in each chamber for a wave condition of Test–1 and three values of opening ratio.

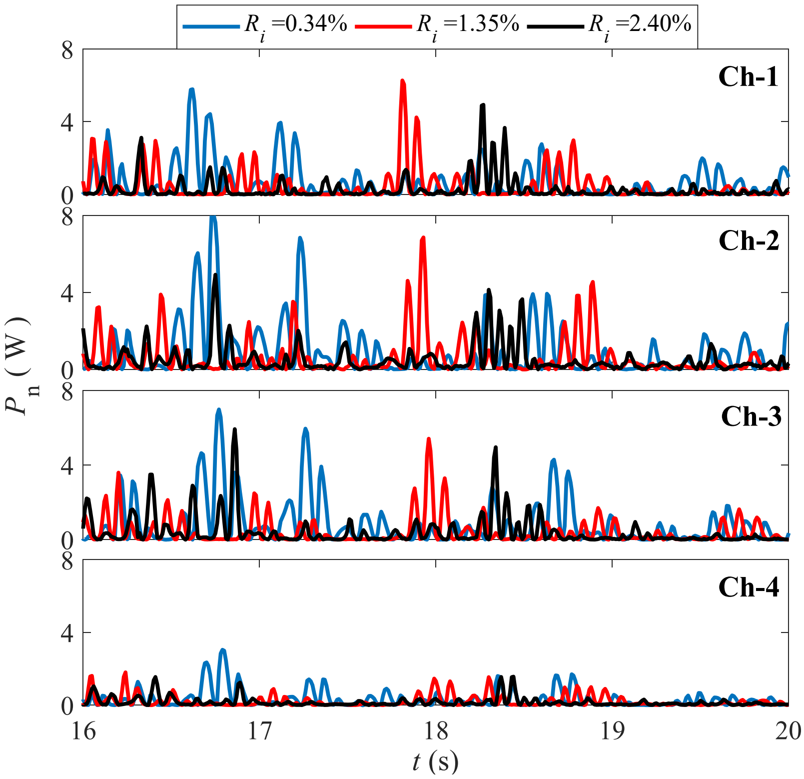

Figure B.13. Sample time–series data of the effect of PTO damping on the pneumatic power P_n in each chamber for a wave condition of Test–1 and three values of opening ratio.

Appendix C : Experimental Uncertainty Analysis

Table C.1. Standard uncertainty Type A calculation.

Wave conditions	Sensors	Test 1	Test 2	Test 3	Standard deviation	Type A $U_{S\text{-}A}$
H=50,T=1.6	G2	22.20	21.32	21.56	0.46	0.27
H=100,T=1.6	G1	47.13	47.57	46.63	0.47	0.27
H=50,T=1.6	Gout	19.10	18.80	19.22	0.21	0.12
H=100,T=1.6	Gout	44.87	44.60	44.45	0.22	0.13
H=50,T=1.6	η1	1.41	1.44	1.44	0.015	0.008
H=100,T=1.6	η1	1.41	1.44	1.44	0.015	0.008
H=50,T=1.6	η2	1.22	1.25	1.27	0.025	0.015
H=100,T=1.6	η2	1.22	1.25	1.27	0.025	0.015
H=50,T=1.6	η3	1.21	1.23	1.19	0.019	0.011
H=100,T=1.6	η3	1.21	1.23	1.19	0.019	0.011
H=50,T=1.6	η4	1.35	1.33	1.34	0.0057	0.003
H=100,T=1.6	η4	1.35	1.33	1.34	0.0057	0.003
H=50,T=1.6	P1	147.23	145.15	144.48	1.44	0.83
H=100,T=1.6	P1	301.46	300.94	298.92	1.34	0.78
H=50,T=1.6	P2	111.05	104.56	105.03	3.61	2.09
H=100,T=1.6	P2	225.51	225.46	221.16	2.50	1.44
H=50,T=1.6	P3	109.96	108.09	108.71	0.95	0.55
H=100,T=1.6	P3	223.28	221.00	222.35	1.15	0.66
H=50,T=1.6	P4	125.98	121.62	123.59	2.18	1.26
H=100,T=1.6	P4	267.81	265.69	265.79	1.12	0.69

Table C.2. Standard uncertainty Type B calculation.

Sensors	Sample No.	Output signal (V)	Converted data (mm or Pa)	Linear fit values	Type B U_{S-B}
Gin	20	6.38	40	40.0	0.0020
Gout	20	6.9	35	34.82	0.0422
G1	16	3.45	8.1	8.60	0.1341
G2	13	4.37	4	3.97	0.0086
G3	17	3.42	9	8.95	0.0126
G4	17	3.20	10	9.94	0.0163
P1	12	12.31	97.05	97.04	0.0012
P2	12	12.5	155.53	155.53	0.0020
P3	19	12.13	41.37	41.37	0.0004
P4	12	13.04	322.90	322.87	0.0041

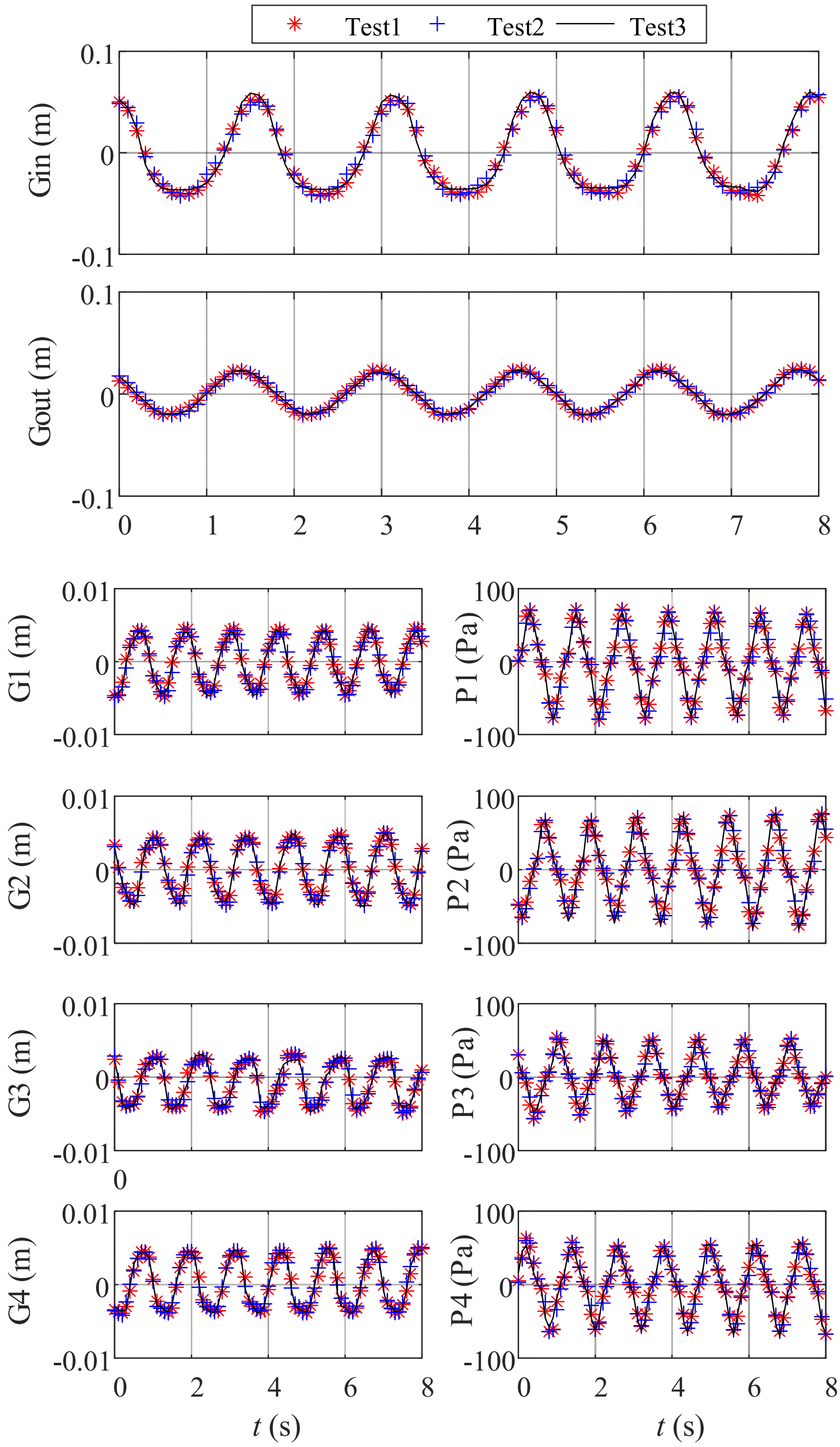

Figure C.14. Experiment repeatability at *H*= 100 mm, *T*= 1.2 s and Ri= 1.34%

Appendix D : MATLAB/Simulink Model Diagrams

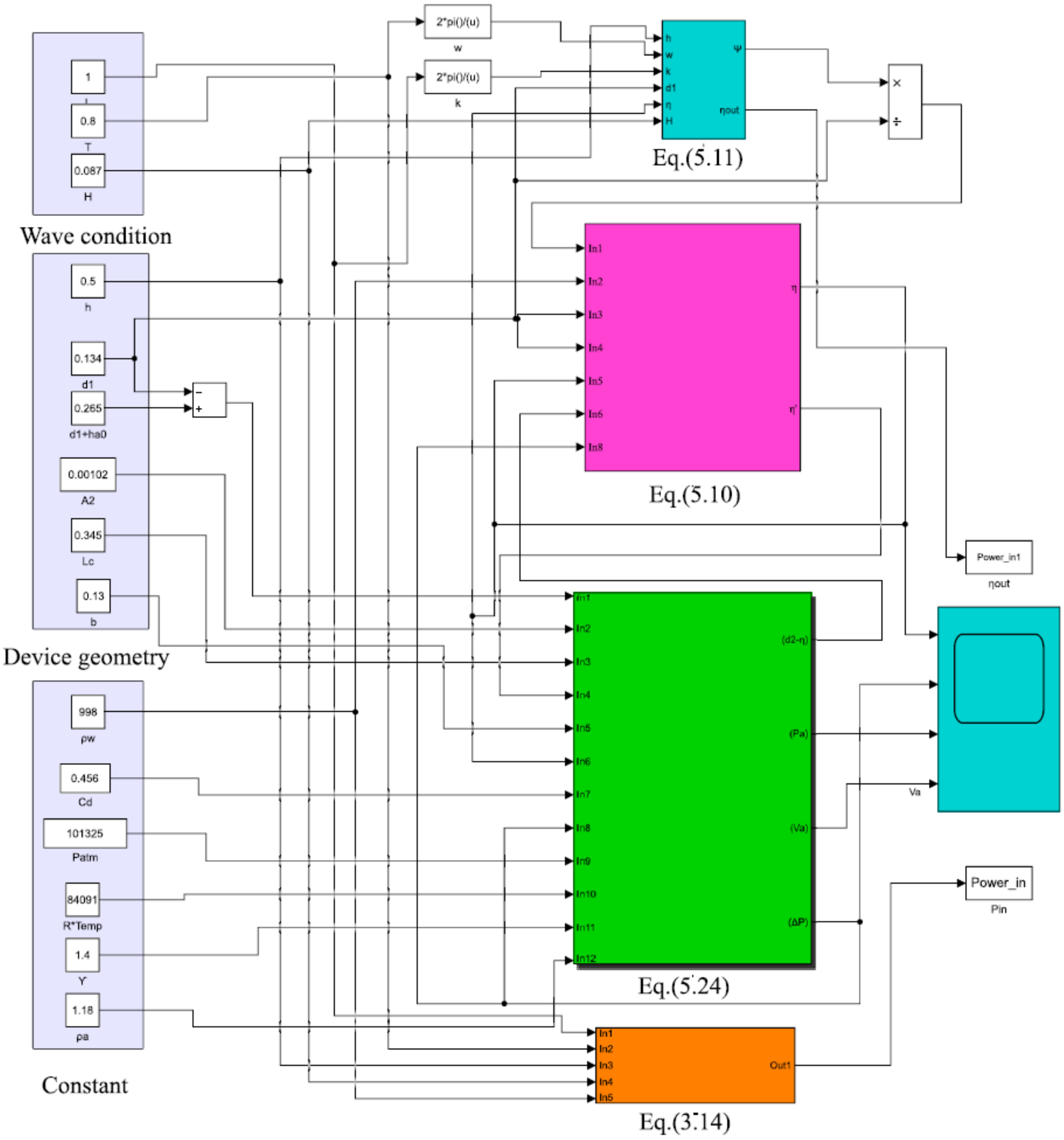

Figure D.15. Single chamber simulation model diagram.

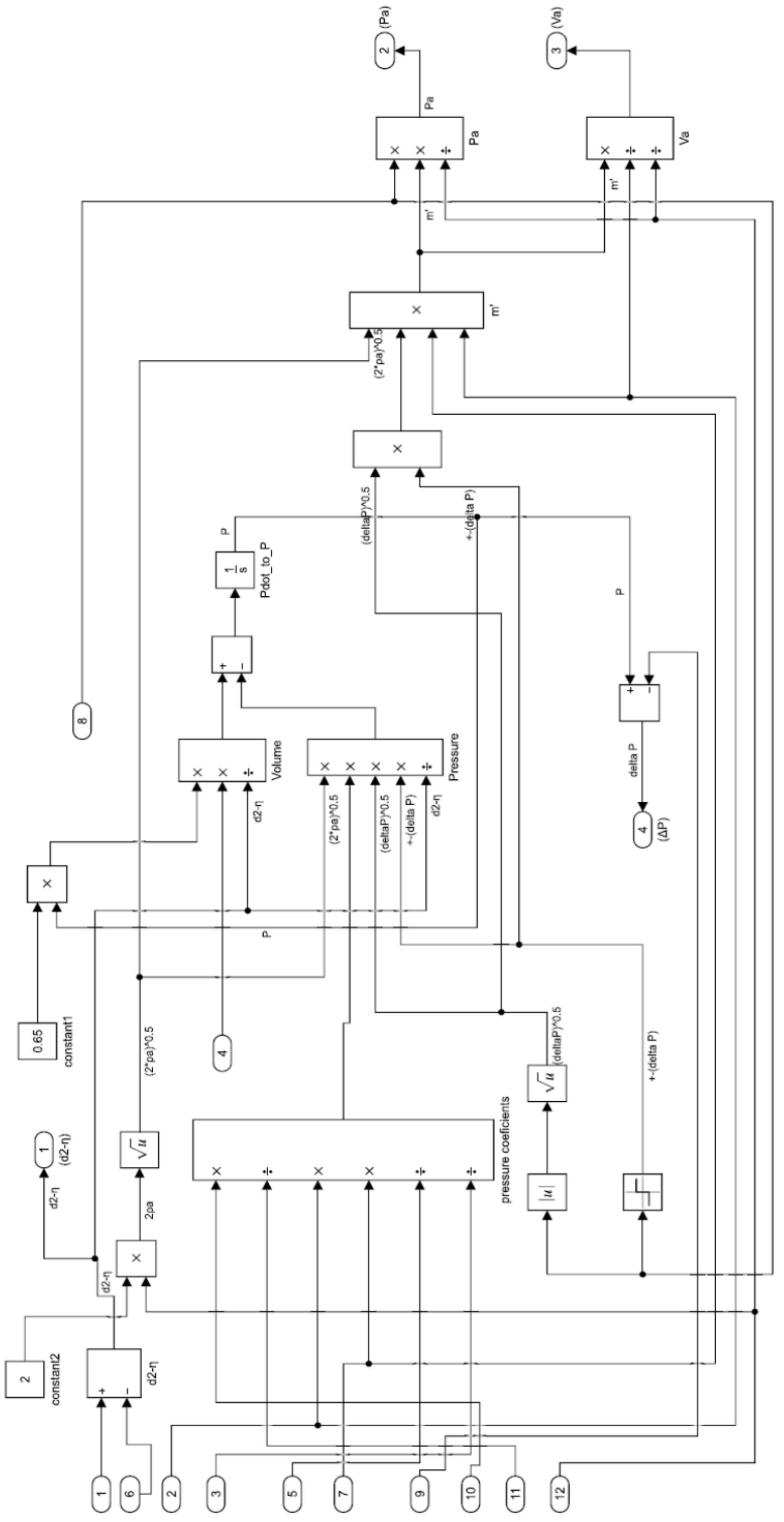

Figure D.16. The pressure drop inside the chamber Δ*p* (Eq.(5.24)) model diagram

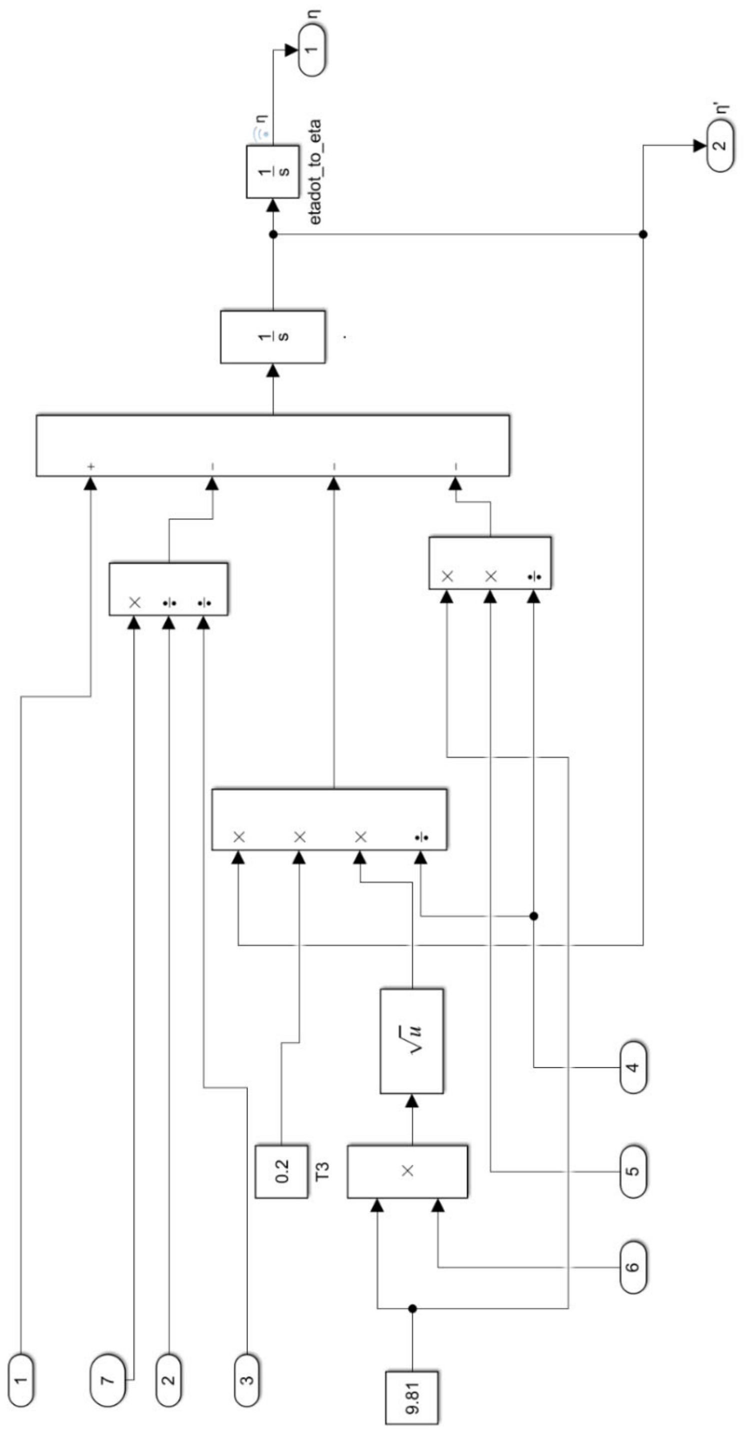

Figure D.17. Newton’s second law model diagram Eq.(5.10)

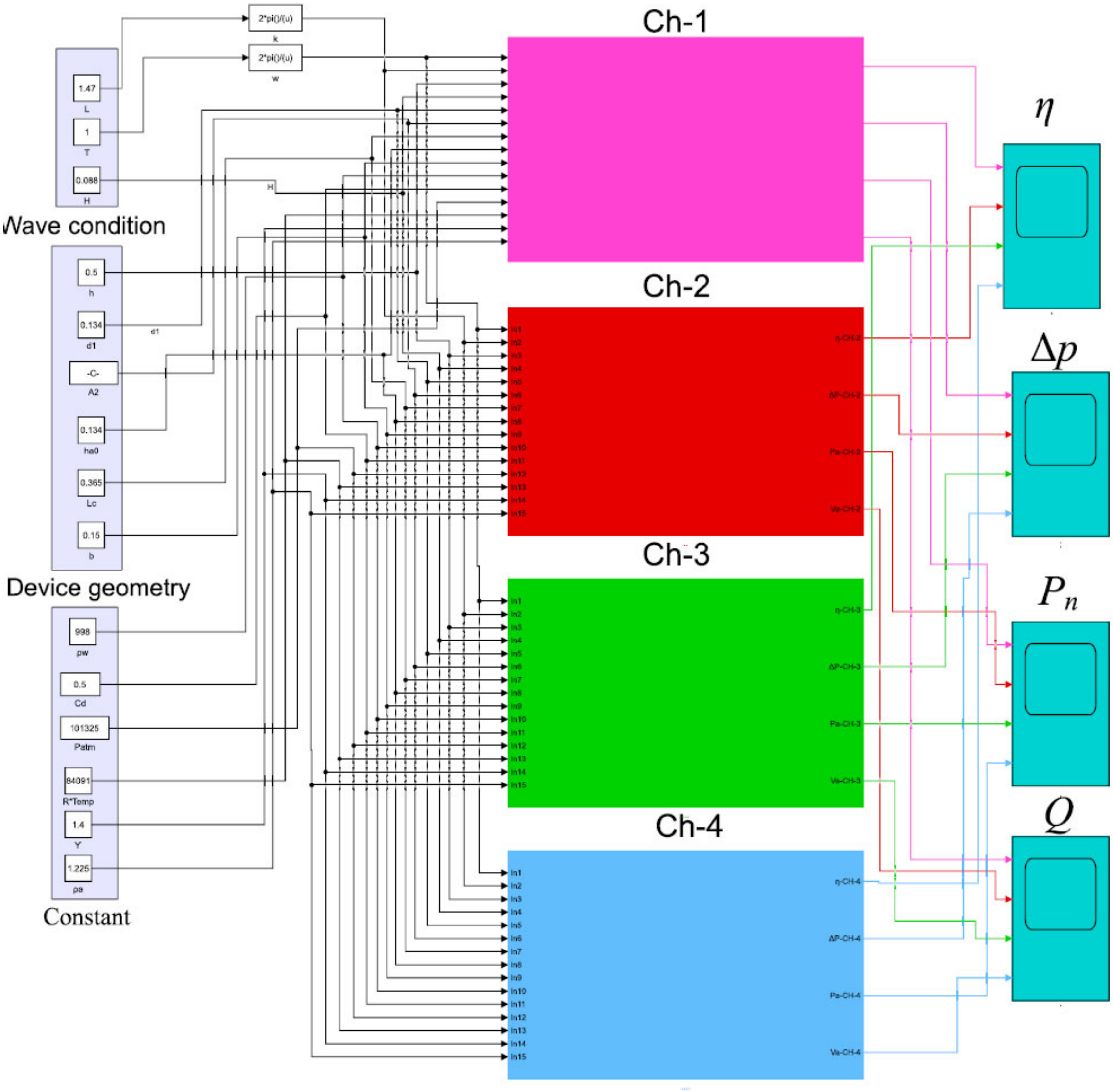

Figure D.18. four chambers MATLAB/Simulink model diagram.

References

[1] López I, Andreu J, Ceballos S, de Alegría IM, Kortabarria I, Review of wave energy technologies and the necessary power-equipment, Renewable and Sustainable Energy Reviews; 27 (2013) 413-34.

[2] Murray R, Review and analysis of ocean energy systems development and supporting policies, International Energy Agency (IEA); (2006).

[3] Government A. Australian Energy Update 2017.vol Energy Statistics and Analysis section, Canberra;2017.

[4] Mork G, Barstow S, Kabuth A, Pontes MT. *Assessing the global wave energy potential*. In: Proceedings of the ASME 2010 29th International conference on ocean, offshore and arctic engineering, American Society of Mechanical Engineers, 2010.

[5] Reguero BG, Losada IJ, Méndez FJ, A global wave power resource and its seasonal, interannual and long-term variability, Applied Energy; 148 (2015) 366-80.

[6] Enerdata. Global Energy Statistical Yearbook, https://yearbook.enerdata.net/electricity/world-electricity-production-statistics.html; 2017 [Accessed April 19. 2017].

[7] Korde UA, Ringwood J. Hydrodynamic Control of Wave Energy Devices: Cambridge University Press; 2016

[8] Czech B, Bauer P, Wave energy converter concepts: Design challenges and classification, IEEE Industrial Electronics Magazine; 6 (2012) 4-16.

[9] Commission E. Study on Lessons for Ocean Energy Development.vol;2017.

[10] Falnes J, A review of wave-energy extraction, Marine Structures; 20 (2007) 185-201.

[11] ArifSyed JM, Thorpe S, Penney K, Australian energy projections to 2029-30, ABARE research report; 10 (2010).

[12] Systems OE. Ocean energies, moving towards competitiveness: a market overview.vol;2016.

[13] Hayward J, Osman P. The potential of wave energy.vol CSIRO;2011.

[14] Esteban M, Leary D, Current developments and future prospects of offshore wind and ocean energy, Appl Energy; 90 (2012) 128-36.

[15] Clément A, McCullen P, Falcão A, Fiorentino A, Gardner F, Hammarlund K, et al., Wave energy in Europe: current status and perspectives, Renewable and Sustainable Energy Reviews; 6 (2002) 405-31.

[16] REN21. Renewables Global Status Report (GSR) 2018.

[17] Magagna D, Uihlein A. JRC ocean energy status report.vol, Publications Office of the European Union: JRC93521;2015.

[18] Delmonte N, Barater D, Giuliani F, Cova P, Buticchi G, Review of oscillating water column converters, IEEE Trans on Industry Applications; 52 (2016) 1698-710.

[19] Heller V, Development of wave devices from initial conception to commercial demonstration, Comprehensive Renewable Energy; 8 (2012) 79-110.

[20] Chowdhury S, Nader J-R, Madrigal Sanchez A, Fleming A, Winship B, Illesinghe S, et al., A review of hydrodynamic investigations into arrays of ocean wave energy converters, retrieved February 2, 2016 from http://arxivorg/ftp/arxiv/papers/1508/150800866pdf; (2015).

[21] Weber J. *WEC Technology Readiness and Performance Matrix–finding the best research technology development trajectory*. In: Proceedings of the International Conference on Ocean Energy, 17-19 October Dublin, Ireland 2012.

[22] Folley M. Numerical Modelling of Wave Energy Converters: State-of-the-Art Techniques for Single Devices and Arrays London, UK: Academic Press; 2016

[23] Khan N, Kalair A, Abas N, Haider A, Review of ocean tidal, wave and thermal energy technologies, Renewable and Sustainable Energy Reviews; 72 (2017) 590-604.

[24] Falcão AF, Henriques JC, Oscillating-water-column wave energy converters and air turbines: A review, Renew Energy; (2015).

[25] Falcão AdO. *The shoreline OWC wave power plant at the Azores*. In: Proceedings of the 4th European Wave Energy Conference, December 4-6 Aalborg, Denmark 2000.

[26] Boake CB, Whittaker TJ, Folley M, Ellen H. *Overview and initial operational experience of the LIMPET wave energy plant*. In: Proceedings of the The Twelfth International Offshore and Polar Engineering Conference, International Society of Offshore and Polar Engineers, 2002.

[27] Takahashi S, Nakada H, Ohneda H, Shikamori M. *Wave power conversion by a prototype wave power extracting caisson in Sakata port*. In: Proceedings of the 23rd International Conference on Coastal Engineering, October 4-9 Venice, Italy 1993.

[28] Alcorn R, Hunter S, Signorelli C, Obeyesekera R, Finnigan T, Denniss T. Results of the testing of the Energetech wave energy plant at Port Kembla.vol Energeth Report;2005.

[29] Washio Y, Osawa H, Nagata Y, Fujii F, Furuyama H, Fujita T. *The offshore floating type wave power device "Mighty Whale": open sea tests*. In: Proceedings of the Tenth International Offshore and Polar Engineering Conference, ISOPE, May 28 -June 2 Seattle, Washington, USA; 2000.

[30] Uihlein A, Magagna D, Wave and tidal current energy–A review of the current state of research beyond technology, Renewable and Sustainable Energy Reviews; 58 (2016).

[31] Fallon D, Hartnett M, Olbert A, Nash S, The effects of array configuration on the hydro-environmental impacts of tidal turbines, Renew Energy; 64 (2014) 10-25.

[32] Martinelli L, Pezzutto P, Ruol P, Experimentally Based Model to Size the Geometry of a New OWC Device, with Reference to the Mediterranean Sea Wave Environment, Energies; 6 (2013) 4696-720.

[33] SEABREATH Ltd, Seabreath wave energy, http://www.seabreath.it; 2018 [Accessed 25 June 2018].

[34] Rasmussen KD. The LEANCON Wave Energy Device, http://www.leancon.com; 2018 [Accessed 5 July 2018].

[35] Kofoed JP, Frigaard P. Hydraulic evaluation of the LEANCON wave energy converter.vol Department of Civil Engineering, Aalborg University;2008.

[36] Kelly T, Dooley T, Campbell J, Ringwood JV, Comparison of the Experimental and Numerical Results of Modelling a 32-Oscillating Water Column (OWC), V-Shaped Floating Wave Energy Converter, Energies; 6 (2013) 4045-77.

[37] Behrens S, Griffin D, Hayward J, Hemer M, Knight C, McGarry S, et al. Ocean renewable energy: 2015–2050. An analysis of ocean energy in Australia. Commonwealth Scientific and Industrial Research Organisation Report2012. p. 212.

[38] Dorrell DG, Kazi S, Papadopoulos M. *Wave Generator Modelling using an Oscillating Water column and a Wells Turbine*. In: Proceedings of the Third IASTED International Conference on Power and Energy Systems, February 24-26 Palm Springs, USA 2003.

[39] Dorrell DG, Halliday R, MacLean S, Miller P, Mosquera FS. *Development of Small-Scale Facilities for Initiating Studies into Sea Wave Energy generation*. In: Proceedings of the International Conference on Renewable Energy and power Quality, March 16-18 Zaragoza, Spain; 2005.

[40] Dorrell DG, Halliday J, Miller P, Findlater M. *Review of wave energy resource and oscillating water column modelling*. In: Proceedings of the 39th International Universities Power Engineering Conference (UPEC) IEEE, September 6-8 Bristol, UK; 2004.

[41] Hsieh M-F, Dorrell DG, Hsieh M-J, Lin C-C, Development of a wave energy converter using a two chamber oscillating water column, IEEE Trans on Sustainable Energy; 3 (2012) 482-97.

[42] Shalby M, Walker P, Dorrell DG. *The Characteristics of the Small Segment Multi-Chamber Oscillating Water Column*. In: Proceedings of the 3rd Asian Wave and Tidal Energy Conferance, October 24-28 Singapore; 2016.

[43] Cruz J. Ocean wave energy: current status and future prespectives: Springer Science & Business Media; 2007

[44] Babarit A, A database of capture width ratio of wave energy converters, Renewable Energy; 80 (2015) 610-28.

[45] Heath T, A review of oscillating water columns, Philosophical Transactions of the Royal Society of London A: Mathematical, Physical and Engineering Sciences; 370 (2012) 235-45.

[46] Brooke J. Wave energy conversion: Elsevier; 2003

[47] Zou S, Abdelkhalik O, Robinett R, Bacelli G, Wilson D, Optimal control of wave energy converters, Rene energy; 103 (2017) 217-25.

[48] Lekube J, Garrido AJ, Garrido I, Rotational speed optimization in oscillating water column wave power plants based on maximum power point tracking, IEEE Trans on Automation Science and Engineering; 14 (2017) 681-91.

[49] O'Sullivan DL, Lewis AW, Generator selection and comparative performance in offshore oscillating water column ocean wave energy converters, IEEE transactions on energy conversion; 26 (2011) 603-14.

[50] Ceballos S, Rea J, Lopez I, Pou J, Robles E, O'Sullivan DL, Efficiency optimization in low inertia wells turbine-oscillating water column devices, IEEE Trans on Energy Conversion; 28 (2013) 553-64.

[51] Alberdi M, Amundarain M, Garrido A, Garrido I, Casquero O, De la Sen M, Complementary control of oscillating water column-based wave energy conversion plants to improve the instantaneous power output, IEEE Trans on Energy Conversion; 26 (2011) 1021-32.

[52] Ramirez D, Bartolome JP, Martinez S, Herrero LC, Blanco M, Emulation of an OWC ocean energy plant with PMSG and irregular wave model, IEEE Transactions on Sustainable Energy; 6 (2015) 1515-23.

[53] Paparella F, Monk K, Winands V, Lopes M, Conley D, Ringwood JV, Up-wave and autoregressive methods for short-term wave forecasting for an oscillating water column, IEEE Transactions on Sustainable Energy; 6 (2015) 171-8.

[54] Kelly JF, Wright WM, Sheng W, O'Sullivan K, Implementation and verification of a wave-to-wire model of an oscillating water column with impulse turbine, IEEE Trans on Sustainable Energy; 7 (2016) 546-53.

[55] Mofor L, Goldsmith J, Jones F, Ocean energy: Technology readiness, patents, deployment status and outlook, Abu Dhabi; (2014).

[56] Guanche R, De Andrés A, Losada I, Vidal C, A global analysis of the operation and maintenance role on the placing of wave energy farms, Energy Conversion and Management; 106 (2015) 440-56.

[57] Veigas M, Iglesias G, Potentials of a hybrid offshore farm for the island of Fuerteventura, Energy Conversion and Management; 86 (2014) 300-8.

[58] Al-Habaibeh A, Su D, McCague J, Knight A, An innovative approach for energy generation from waves, Energy Conversion and Management; 51 (2010) 1664-8.

[59] Chang G, Ruehl K, Jones CA, Roberts J, Chartrand C, Numerical modeling of the effects of wave energy converter characteristics on nearshore wave conditions, Rene Energy; 89 (2016) 636-48.

[60] Dorrell DG, Hsieh M-F, Lin C-C, A multichamber oscillating water column using cascaded savonius turbines, IEEE Trans on Industry Applications; 46 (2010) 2372-80.

[61] Dorrell DG, Hsieh M-F, Lin C-C, A small segmented oscillating water column using a Savonius rotor turbine, IEEE Trans on Industry Applications; 46 (2010) 2080-8.

[62] Drew B, Plummer AR, Sahinkaya MN, A review of wave energy converter technology; (2009).

[63] Naty S, Viviano A, Foti E, Wave Energy Exploitation System Integrated in the Coastal Structure of a Mediterranean Port, Sustainability; 8 (2016) 1342.

[64] Naty S, Viviano A, Foti E, Feaseability study of a wec integrated in the port of giardini naxos, italy, Coastal Eng Proc; 1 (2017) 22.

[65] Vicinanza D, Contestabile P, Nørgaard JQH, Andersen TL, Innovative rubble mound breakwaters for overtopping wave energy conversion, Coastal Eng 88 (2014) 154-70.

[66] Titah-Benbouzid H, Benbouzid M, An Up-to-Date Technologies Review and Evaluation of Wave Energy Converters, INTERNATIONAL REVIEW OF ELECTRICAL ENGINEERING-IREE; 10 (2015) 52–61.

[67] Evans D, Porter R, Hydrodynamic characteristics of an oscillating water column device, Applied Ocean Research; 17 (1995) 155-64.

[68] Falcão AF, Gato LM, Henriques JC, Borges JE, Pereiras B, Castro F, A novel twin-rotor radial-inflow air turbine for oscillating-water-column wave energy converters, Energy; 93 (2015) 2116-25.

[69] Babarit A, A database of capture width ratio of wave energy converters, Rene Energy; 80 (2015) 610-28.

[70] Dorrell D, Findlater M. Computational fluid dynamic modelling of a wells turbine. IASTED EuroPES conference2004.

[71] Dorrell D, Halliday J, Miller P, Findlater M. *Review of wave energy resource and oscillating water column modelling*. In: Proceedings of the Universities Power Engineering Conference, 2004 UPEC 2004 39th International, IEEE, 2004.

[72] Dorrell DG, Kazi S, Papadopoulos M. *Experiences in Wave Generator Modelling using an Oscillating Water column and a Wells Turbine*. In: Proceedings of the Third IASTED International Conference on Power and Energy Systems, 24-26 February, Palm Springs, USA; 2003.

[73] Shalby M, Walker P, Dorrell DG. *The investigation of a segment multi-chamber oscillating water column in physical scale model*. In: Proceedings of the 5th International Conference on Renewable Energy Research and Applications, November 20-23 Birmingham, UK; 2016.

[74] Holmes B, Nielsen K. Report T02-2.1 Guidelines for the Development and Testing of Wave Energy Systems.vol Tech. Rep. OES-IA Annex II Task 2.1;2010.

[75] Hotta H, Washio Y, Yokozawa H, Miyazaki T, R&D on wave power device “Mighty Whale”, Renewable Energy; 9 (1996) 1223-6.

[76] Percival M, Leung P, Datta P. *The development of a vertical turbine for domestic electricity generation*. In: Proceedings of the European Wind Energy Conference&Exhibition, 2004.

[77] Heath T, Whittaker T, Boake C. *The design, construction and operation of the LIMPET wave energy converter (Islay, Scotland)*. In: Proceedings of the 4th European wave energy conference, 2000.

[78] Dorrell D, Fillet W. *Investigation of a small-scale segmented oscillating water column utilizing a Savonius rotor turbine*. In: Proceedings of the International Conference on Energy and Environment, 2006.

[79] Dorrell DG, Hsieh M-F. *Performance of Wells turbines for use in small-scale oscillating water columns*. In: Proceedings of the The Eighteenth International Offshore and Polar Engineering Conference, ISOP, 6-11 July, Vancouver, Canada; 2008.

[80] Dorrell DG, Hsieh M-F, Fillet W. *Segmented small oscillating water columns using in-line Savonius rotors*. In: Proceedings of the The Seventeenth International Offshore and Polar Engineering Conference, ISOPE, 1-6 July, Lisbon, Portugal; 2007.

[81] Evans D, Wave-power absorption by systems of oscillating surface pressure distributions, Journal of Fluid Mechanics; 114 (1982) 481-99.

[82] Pecher A, Kofoed JP. Handbook of Ocean Wave Energy, Ocean Engineering & Oceanography: Springer International Publishing; 2017 10.1007/978-3-319-39889-1.

[83] Govardhan M, Dhanasekaran T, Effect of guide vanes on the performance of a self-rectifying air turbine with constant and variable chord rotors, Rene Energy; 26 (2002) 201-19.

[84] Raghunathan S, A methodology for Wells turbine design for wave energy conversion, Proceedings of the Institution of Mechanical Engineers, Part A: Journal of Power and Energy; 209 (1995) 221-32.

[85] Sjolte J, Tjensvoll G, Molinas M, Power collection from wave energy farms, Applied Sciences; 3 (2013) 420-36.

[86] Wu F, Zhang X-P, Ju P, Sterling MJ, Modeling and control of AWS-based wave energy conversion system integrated into power grid, IEEE Transactions on Power Systems; 23 (2008) 1196-204.

[87] Hansen RH, Kramer MM, Vidal E, Discrete displacement hydraulic power take-off system for the wavestar wave energy converter, Energies; 6 (2013) 4001-44.

[88] Raghunathan S, Beattie W, Aerodynamic performance of contra-rotating Wells turbine for wave energy conversion, Institution of Mechanical Engineers, Part A: Journal of Power and Energy; 210 (1996) 431-47.

[89] Kim TW, Kaneko K, Setoguchi T, Inoue M. *Aerodynamic performance of an impulse turbine with self-pitch-controlled guide vanes for wave power generator*. In: Proceedings of the KSME/JSME THERMAL and FLUID Engineering Conference 1998.

[90] Setoguchi T, Takao M, Kinoue Y, Kaneko K, Santhakumar S, Inoue M. *Study on an impulse turbine for wave energy conversion*. In: Proceedings of the The Ninth International Offshore and Polar Engineering Conference, ISOPE, 30 May -4 June, Brest, France 1999.

[91] Inoue M, Kaneko K, Setoguchi T, Raghunathan S. *Simulation of starting characteristics of the Wells turbine*. In: Proceedings of the 4th Joint Fluid Mechanics, Plasma Dynamics and Lasers Conference, 12-14 May, Atlanta, Georgia; 1986.

[92] INOUE M, KANEKO K, SETOGUCHI T, SARUWATARI T, Studies on the Wells turbine for wave power generator (turbine characteristics and design parameter for irregular wave), JSME international journal Ser 2, Fluids engineering, heat transfer, power, combustion, thermophysical properties; 31 (1988) 676-82.

[93] Gato L, Warfield V, Thakker A, Performance of a high-solidity Wells turbine for an OWC wave power plant, Journal of energy resources technology; 118 (1996) 263-8.

[94] Falcão AFO, Henriques JCC, Gato LMC, Self-rectifying air turbines for wave energy conversion: A comparative analysis, Renewable and Sustainable Energy Reviews; 91 (2018) 1231-41.

[95] Raghunathan S, The Wells air turbine for wave energy conversion, Progress in Aerospace Sciences; 31 (1995) 335-86.

[96] Network MRI, Multi-chamber oscillating water column device for harvesting Ocean Renewable Energy; (2014).

[97] He F, Huang Z, Hydrodynamic performance of pile-supported OWC-type structures as breakwaters: An experimental study, Ocean Eng 88 (2014) 618-26.

[98] López I, Pereiras B, Castro F, Iglesias G, Performance of OWC wave energy converters: influence of turbine damping and tidal variability, International Journal of Energy Research; 39 (2015) 472-83.

[99] Elhanafi A, Fleming A, Macfarlane G, Leong Z, Numerical energy balance analysis for an onshore oscillating water column–wave energy converter, Energy; 116 (2016) 539-57.

[100] Huckerby J, Jeffrey H, Jay B, Executive O, An international vision for ocean energy, The Ocean Energy Systems Implementing Agreement (OES); (2011).

[101] Uihlein A, Magagna D, Wave and tidal current energy–A review of the current state of research beyond technology, Renewable and Sustainable Energy Reviews; 58 (2016) 1070-81.

[102] Hughes SA. Physical models and laboratory techniques in coastal engineering: World Scientific; 1993

[103] Boccotti P. Wave Mechanics for Ocean Engineering: Elsevier; 2000

[104] Sorensen RM. Basic Coastal Engineering: Springer; 2006

[105] Dean RG, Dalrymple RA. Water wave mechanics for engineers and scientists: world scientific publishing Co Inc; 1991

[106] Tucker M, Pitt E. Waves in ocean engineering: Elsevier, Amsterdam, New York; 2001

[107] Le Méhauté B, An Introduction to Hydrodynamics and Water Waves Volume II: Water Wave Theories; (1969).

[108] Ltd TEME. TANK TESTING OF WAVE ENERGY CONVERSION SYSTEMS.vol The European Marine Energy Centre Ltd, UK;2009.

[109] Pierson Jr WJ, Moskowitz L, A proposed spectral form for fully developed wind seas based on the similarity theory of SA Kitaigorodskii, Journal of geophysical research; 69 (1964) 5181-90.

[110] Hasselmann K, Barnett T, Bouws E, Carlson H, Cartwright D, Enke K, et al., Measurements of wind-wave growth and swell decay during the Joint North Sea Wave Project (JONSWAP), Ergänzungsheft 8-12; (1973).

[111] Bretschneider CL. Wave variability and wave spectra for wind-generated gravity waves.vol CORPS OF ENGINEERS WASHINGTON DC BEACH EROSION BOARD;1959.

[112] Ochi MK, Hubble EN. Six-parameter wave spectra. Coastal Engineering 19761977. p. 301-28.

[113] López I, Pereiras B, Castro F, Iglesias G, Optimisation of turbine-induced damping for an OWC wave energy converter using a RANS–VOF numerical model, Appl Energy; 127 (2014) 105-14.

[114] Folley M, Babarit A, Child B, Forehand D, O'Boyle L, Silverthorne K, et al. *A review of numerical modelling of wave energy converter arrays*. In: Proceedings of the 31st International Conference on Ocean, Offshore and Arctic Engineering, The American Society of Mechanical Engineers (ASME), July 1-6 Rio de Janeiro, Brazil; 2012.

[115] Evans D, The oscillating water column wave-energy device, IMA Journal of Applied Mathematics; 22 (1978) 423-33.

[116] Mei CC, Power extraction from water waves, Journal of Ship Research; 20 (1976) 63-6.

[117] Budal K, Theory for absorption of wave power by a system of interacting bodies, Journal of Ship Research; 21 (1977).

[118] Brendmo A, Falnes J, Lillebekken P, Linear modelling of oscillating water columns including viscous loss, Appl ocean research; 18 (1996) 65-75.

[119] Falcão AdO, Sarmento A. *Wave generation by a periodic surface pressure and its application in wave-energy extraction*. In: Proceedings of the 15th international congress of theoritical and applied mechanics, August 17-23 Toronto, Canada; 1980.

[120] Baudry V, Babarit A, Clément A. *An overview of analytical, numerical and experimental methods for modelling oscillating water columns*. In: Proceedings of the 10th European Wave and Tidal Energy Conference, September 6-10 Aalborg, Denmark; ; 2013.

[121] Brito-Melo A, Hofmann T, Sarmento A, Clément A, Delhommeau G, Numerical modelling of OWC-shoreline devices including the effect of surrounding coastline and non-flat bottom, International Journal of Offshore and Polar Engineering; 11 (2001).

[122] Le Crom I, Brito-Melo A, Neumann F, Sarmento A. *Numerical estimation of incident wave parameters based on the air pressure measurements in pico OWC plant*. In: Proceedings of the 8th European Wave and Tidal Energy Conference, September 7-10 Uppsala, Sweden; 2009.

[123] Elhanafi A, Fleming A, Macfarlane G, Leong Z, Numerical hydrodynamic analysis of an offshore stationary–floating oscillating water column–wave energy converter using CFD, International Journal of Naval Architecture and Ocean Engineering; 9 (2017) 77-99.

[124] Revill S, A simple analytical model for a fixed oscillating water column device (tech. rep. No. PR8), National Engineering Laboratory Glasgow; (1978).

[125] Robinson RW. The effects of geometric-wavefield interactions on the performance of oscillating water column wave energy convertors: Queen's University of Belfast; 1982.

[126] Maeda H, Kinoshita T, Masuda K, Kato W, Fundamental research on oscillating water column wave power absorbers, Journal of energy resources technology; 107 (1985) 81-6.

[127] Ma Q. *Nonlinear analysis on hydrodynamic performance of oscillating water column wave energy device with a lateral opening*. In: Proceedings of the 14th Intl Conf on Offshore Mechanics & Arctic Engng, ASME et al, Copenhagen, Denmark; 1995.

[128] Gouaud F, Rey V, Piazzola J, Van Hooff R, Experimental study of the hydrodynamic performance of an onshore wave power device in the presence of an underwater mound, Coastal Engineering; 57 (2010) 996-1005.

[129] Falcão AF, Henriques JC, Cândido JJ, Dynamics and optimization of the OWC spar buoy wave energy converter, Renewable energy; 48 (2012) 369-81.

[130] Sykes R, Lewis A, Thomas G. *Predicting hydrodynamic pressure in fixed and floating OWC using a piston model*. In: Proceedings of the In proceedings of 9th European wave and tidal energy conference, Southampton, 2011.

[131] Gervelas R, Trarieux F, Patel M, A time-domain simulator for an oscillating water column in irregular waves at model scale, Ocean Engineering; 38 (2011) 1007-13.

[132] Harrison J, Patel M, Brown D, Hydrodynamic analysis of marine vehicles with pneumatic compliance, Royal Institution of Naval Architects Transactions; 129 (1987).

[133] Sheng W, Alcorn R, Lewis A, On thermodynamics in the primary power conversion of oscillating water column wave energy converters, Journal of Renewable and Sustainable Energy; 5 (2013) 023105.

[134] Sarmento AJNA, Gato LMC, de O. Falcão AF, Turbine-controlled wave energy absorption by oscillating water column devices, Ocean Engineering; 17 (1990) 481-97.

[135] Josset C, Clément A, A time-domain numerical simulator for oscillating water column wave power plants, Rene energy; 32 (2007) 1379-402.

[136] Falcao AdO, Justino P, OWC wave energy devices with air flow control, Ocean Engineering; 26 (1999) 1275-95.

[137] Elhanafi A, Macfarlane G, Ning D, Hydrodynamic performance of single–chamber and dual–chamber offshore–stationary Oscillating Water Column devices using CFD, Appl Energy; 228 (2018) 82-96.

[138] Zhang Y, Zou Q-P, Greaves D, Air–water two-phase flow modelling of hydrodynamic performance of an oscillating water column device, Renewable Energy; 41 (2012) 159-70.

[139] He F, Huang Z, Characteristics of orifices for modeling nonlinear power take-off in wave-flume tests of oscillating water column devices, Journal of Zhejiang University-SCIENCE A; 18 (2017) 329-45.

[140] Simonetti I, Cappietti L, Elsafti H, Oumeraci H, Optimization of the geometry and the turbine induced damping for fixed detached and asymmetric OWC devices: a numerical study, Energy; (2017).

[141] Windt C, Davidson J, Ringwood JV, High-fidelity numerical modelling of ocean wave energy systems: A review of computational fluid dynamics-based numerical wave tanks, Renewable and Sustainable Energy Reviews; 93 (2018) 610-30.

[142] Luo Y, Nader J-R, Cooper P, Zhu S-P, Nonlinear 2D analysis of the efficiency of fixed Oscillating Water Column wave energy converters, Renew Energy; 64 (2014) 255-65.

[143] López I, Pereiras B, Castro F, Iglesias G, Holistic performance analysis and turbine-induced damping for an OWC wave energy converter, Rene Energy; 85 (2016) 1155-63.

[144] Kamath A, Bihs H, Arntsen ØA, Numerical modeling of power take-off damping in an oscillating water column device, International Journal of Marine Energy; 10 (2015) 1-16.

[145] Vyzikas T, Deshoulières S, Giroux O, Barton M, Greaves D, Numerical study of fixed Oscillating Water Column with RANS-type two-phase CFD model, Renewable Energy; 102 (2017) 294-305.

[146] Elhanafi A, Macfarlane G, Fleming A, Leong Z, Investigations on 3D effects and correlation between wave height and lip submergence of an offshore stationary OWC wave energy converter, Appl Ocean Res 64 (2017) 203-16.

[147] Holmes B. Tank testing of wave energy conversion systems: marine renewable energy guides: European Marine Energy Centre; 2009

[148] Payne G, Guidance for the experimental tank testing of wave energy converters, The University of Edinburgh: Newington, Edinburgh, UK; (2008).

[149] Falcão AFO, Henriques JCC, Model-prototype similarity of oscillating-water-column wave energy converters, International Journal of Marine Energy; 6 (2014) 18-34.

[150] Fleming A, Macfarlane G, In-situ orifice calibration for reversing oscillating flow and improved performance prediction for oscillating water column model test experiments, International Journal of Marine Energy; 17 (2017) 147-55.

[151] Ning D, Wang R, Zhang C, Numerical Simulation of a Dual-Chamber Oscillating Water Column Wave Energy Converter, Sustainability; 9 (2017) 1599.

[152] Crema I, Simonetti I, Cappietti L, Oumeraci H. *Laboratory experiments on oscillating water column wave energy converters integrated in a very large floating structure*. In: Proceedings of the 11th European Wave and Tidal Energy Conference (EWTEC), September 5-9 Southampton, UK; 2015.

[153] Mendes A, Monteiro W. *Performance analysis of a model of OWC energy converter in non-linear waves*. In: Proceedings of the 7th European wave and tidal energy conference, September 11-13 Porto, Portugal; 2007.

[154] Sarmento AJNA, Wave flume experiments on two-dimensional oscillating water column wave energy devices, Experiments in Fluids; 12 (1992) 286-92.

[155] Ning D-Z, Wang R-Q, Zou Q-P, Teng B, An experimental investigation of hydrodynamics of a fixed OWC Wave Energy Converter, Applied Energy; 168 (2016) 636-48.

[156] Simonetti I, Cappietti L, El Safti H, Oumeraci H. *Numerical modelling of fixed oscillating water column wave energy conversion devices: toward geometry hydraulic optimization*. In: Proceedings of the ASME 34th International Conference on Ocean, Offshore and Arctic Engineering, May 31-June 5 Newfoundland, Canada; 2015.

[157] Price A, Dent C, Wallace A, On the capture width of wave energy converters, Applied Ocean Research; 31 (2009) 251-9.

[158] Rezanejad K, Bhattacharjee J, Guedes Soares C, Stepped sea bottom effects on the efficiency of nearshore oscillating water column device, Ocean Engineering; 70 (2013) 25-38.

[159] van't Veer R, Tholen HJ. *Added resistance of moonpools in calm water*. In: Proceedings of the ASME 2008 27th International Conference on Offshore Mechanics and Arctic Engineering, 15-20 June, The American Society of Mechanical Engineers (ASME), Estoril, Portugal; 2008.

[160] Rezanejad K, Guedes Soares C, López I, Carballo R, Experimental and numerical investigation of the hydrodynamic performance of an oscillating water column wave energy converter, Renewable Energy; 106 (2017) 1-16.

[161] Payne GS, Taylor JR, Ingram D, Best practice guidelines for tank testing of wave energy converters, The Journal of Ocean Technology; 4 (2009) 38-70.

[162] Chakrabarti SK. Offshore structure modeling: World Scientific; 1994

[163] Vyzikas T, Deshoulières S, Barton M, Giroux O, Greaves D, Simmonds D, Experimental investigation of different geometries of fixed oscillating water column devices, Rene Energy; 104 (2017) 248-58.

[164] Chisholm D. Two-phase flow in pipelines and heat exchangers: G. Godwin in association with Institution of Chemical Engineers; 1983

[165] Fossa M, Guglielmini G, Pressure drop and void fraction profiles during horizontal flow through thin and thick orifices, Experimental Thermal and Fluid Science; 26 (2002) 513-23.

[166] Standard I, 5167-1. Measurement of fluid flow by means of pressure differential devices, ISO, Geneva, Switzerland; (1991).

[167] He F, Leng J, Zhao X, An experimental investigation into the wave power extraction of a floating box-type breakwater with dual pneumatic chambers, Applied Ocean Research; 67 (2017) 21-30.

[168] He F, Li M, Huang Z, An experimental study of pile-supported OWC-type breakwaters: energy extraction and vortex-induced energy loss, Energies; 9 (2016) 540.

[169] Elhanafi A, Kim CJ, Experimental and numerical investigation on wave height and power take–off damping effects on the hydrodynamic performance of an offshore–stationary OWC wave energy converter, Renew Energy; 125 (2018) 518-28.

[170] Martinelli L, Ruol P, Fassina E, Giuliani F, Delmonte N, A Wave-2-Wire Experimental Investigation of the New “Seabreath” Wave Energy Converter: The Hydraulic Response, Coastal Engineering Proceedings; 1 (2014) 29.

[171] Morris-Thomas MT, Irvin RJ, Thiagarajan KP, An investigation into the hydrodynamic efficiency of an oscillating water column, Journal of Offshore Mechanics and Arctic Engineering; 129 (2007) 273-8.

[172] Elhanafi A, Macfarlane G, Fleming A, Leong Z, Experimental and numerical investigations on the intact and damage survivability of a floating–moored oscillating water column device, Appl Ocean Research; 68 (2017) 276-92.

[173] Elhanafi A, Macfarlane G, Fleming A, Leong Z, Experimental and numerical investigations on the hydrodynamic performance of a floating–moored oscillating water column wave energy converter, Appl Energy; 205 (2017) 369-90.

[174] Kofoed JP, Frigaard P, Development of wave energy devices: The Danish case/the dragon of nissum bredning, Journal of Ocean Technology; (2009).

[175] ISO I, OIML B, Guide to the Expression of Uncertainty in Measurement, Geneva, Switzerland; (1995).

[176] ITTC. Recommended Procedures and Guidelines: Uncertainty Analysis for a Wave Energy Converter.vol 7.5-02-07-03.12, ITTC Report: 7.5-02-07-03.12;2017.

[177] ITTC. Recommended Procedures and Guidelines: Testing and Extrapolation Methods, General Guidelines for Uncertainty Analysis in Resistance Towing Tank Tests.vol 7.5-02-02-02, ITTC Report: 7.5-02-02-02.;2008.

[178] Sarmento AJ, Falcão AdO, Wave generation by an oscillating surface-pressure and its application in wave-energy extraction, Journal of Fluid Mechanics; 150 (1985) 467-85.

[179] Dong R. Effective mass and damping of submerged structures.vol California Univ.;1978.

[180] Patel M, Harrison J, The mechanics of a compliant motion suppression system for semisubmersibles, Journal of sound and vibration; 106 (1986) 491-507.

[181] Alves M, Vicente M, Sarmento A, Guerinel M. *Implementation and verification of a time domain model to simulate the dynamics of OWCs*. In: Proceedings of the 9th European Wave and Tidal Energy Conference, 2011.

[182] Falnes J. Ocean waves and oscillating systems: linear interactions including wave-energy extraction: Cambridge university press; 2002

[183] Hahn B, Valentine DT. Essential MATLAB for engineers and scientists: Academic Press; 2016

[184] Wendt JF. Computational fluid dynamics: an introduction: Springer Science & Business Media; 2008

[185] Tu J, Yeoh GH, Liu C. Computational fluid dynamics: a practical approach: Butterworth-Heinemann; 2018

[186] Alfonsi G. Reynolds-Averaged Navier-Stokes Equations for Turbulence Modeling2009 10.1115/1.3124648.

[187] Hirt CW, Nichols BD, Volume of fluid (VOF) method for the dynamics of free boundaries, Journal of computational physics; 39 (1981) 201-25.

[188] Berberović E, van Hinsberg NP, Jakirlić S, Roisman IV, Tropea C, Drop impact onto a liquid layer of finite thickness: Dynamics of the cavity evolution, Physical Review E; 79 (2009) 036306.

[189] Choi J, Yoon SB, Numerical simulations using momentum source wave-maker applied to RANS equation model, Coastal Engineering; 56 (2009) 1043-60.

[190] Elhanafi A, Macfarlane G, Fleming A, Leong Z, Scaling and air compressibility effects on a three-dimensional offshore stationary OWC wave energy converter, Appl Energy; 189 (2017) 1-20.

[191] ITTC. Recommended Procedures and Guidelines: Practical Guidelines for Ship CFD Applications.vol, ITTC Report: 7.5-03 02-03;2011.

[192] CD-Adapco. User Guid STAR-CCM+ Version 10.02.vol;2015.